


<b>Title</b>	First principles modelling of nucleation and growth during atomic layer deposition onto III-V substrates
<b>Author(s)</b>	Klejna, Sylwia
<b>Publication date</b>	2013
<b>Original citation</b>	Klejna, S. 2013. First principles modelling of nucleation and growth during atomic layer deposition onto III-V substrates. PhD Thesis, University College Cork.
<b>Type of publication</b>	Doctoral thesis
<b>Rights</b>	© 2013, Sylwia Klejna <a href="http://creativecommons.org/licenses/by-nc-nd/3.0/">http://creativecommons.org/licenses/by-nc-nd/3.0/</a> 
<b>Item downloaded from</b>	<a href="http://hdl.handle.net/10468/1369">http://hdl.handle.net/10468/1369</a>

Downloaded on 2017-02-12T08:20:16Z

Ollscoil na hÉireann  
NATIONAL UNIVERSITY OF IRELAND



First principles modelling of nucleation and growth during  
atomic layer deposition onto III-V substrates

*by*

**Sylwia Klejna**

Supervisor: Dr. Simon D. Elliott  
Head of Department: Prof. Michael Morris

*A thesis presented to*

NATIONAL UNIVERSITY OF IRELAND, CORK  
College of Science, Engineering & Food Science  
Department of Chemistry  
Tyndall National Institute

*for the degree of*

***Doctor of Philosophy***

**July 2013**

## Table of Contents

Acknowledgments .....	5
Abstract .....	6
1 Introduction .....	7
1.1 High- <i>k</i> dielectric films and III-V substrates .....	8
1.2 Atomic layer deposition technique .....	9
1.3 Atomic layer deposition processes for high- <i>k</i> dielectric films .....	12
1.4 ‘Self-cleaning’ ALD .....	15
1.5 Outline of the work .....	18
2 Methods of research.....	20
2.1 First principles methods.....	20
2.1.1 Density functional theory.....	21
2.1.2 High-level <i>ab initio</i> computations.....	23
2.2 Approach to materials modeling .....	24
2.2.1 Bulk computations.....	24
2.2.2 Constructing surface model .....	26
2.2.3 <i>Ab initio</i> thermodynamics .....	28
2.3 Population analysis .....	30
2.4 Transition state searches .....	31
3 TMA - clean-up reagent for atomic layer deposition of alumina onto III-V substrates	33
3.1 Introduction .....	34
3.2 Bulk potential energies .....	35
3.3 Homolytic and heterolytic dissociation of TMA .....	39
3.4 TMA adsorption onto As <sub>2</sub> O <sub>3</sub> surface .....	41
3.5 Methyl transfer mechanisms at surface .....	42
3.6 Population analysis of reduced structures .....	48
3.7 Production of various volatile species .....	49
3.8 Discussion.....	58
3.9 Conclusion.....	63
4 Mechanisms for substrate-enhanced growth during the early stages of atomic layer deposition of alumina onto silicon nitride surfaces.....	65
4.1 Introduction .....	66
4.1.1 Summary of experimental results.....	67
4.1.2 Summary of other theoretical results .....	68
4.2 Computational method.....	70
4.2.1 Models of bulk crystals .....	70
4.2.2 Models of substrate surfaces.....	71

4.2.3	Models of gas-phase molecules .....	71
4.3	Non-ALD decomposition reactions .....	72
4.4	Conclusion .....	75
5	Decomposition of metal alkylamides, alkyls and halides for self-cleaning atomic layer deposition of dielectrics onto III-V substrates .....	77
5.1	Introduction .....	78
5.2	Computational method and approach .....	78
5.3	Formation of metal oxides from gas phase precursors .....	82
5.4	Dissociation of ligand by M-L scission .....	84
5.5	Decomposition of dma ligand .....	88
5.5.1	C-H scission and H elimination (B-E) .....	89
5.5.2	N-C scission (F-G) .....	92
5.6	Further decomposition of dma ligand .....	93
5.6.1	Multiple redox steps – dehydrogenation H-I .....	93
5.6.2	Multiple redox steps J-K .....	95
5.7	Effect of substrate on clean-up .....	98
5.8	Conclusion .....	104
6	Mechanisms for decomposition of metal alkylamides at reducible oxide surfaces .....	107
6.1	Introduction .....	108
6.2	Survey of possible products using bulk and gas-phase models .....	109
6.3	Adsorption at bare native oxide surface .....	115
6.4	Migration of the ligand at bare native oxide surface .....	119
6.5	CVD reactions .....	126
6.6	Secondary decomposition surface reactions .....	129
6.7	Conclusion .....	132
7	Summary and Suggestions for Further Work .....	134
	Bibliography .....	137
	Table of Abbreviations .....	150

I, Sylwia Klejna, certify that this thesis is my own work and I have not obtained a degree in this university or elsewhere on the basis of the work submitted in this thesis.

*Sylwia Klejna*

## **Acknowledgments**

I would like to express my extraordinary gratitude for my supervisor, Dr. Simon D. Elliott. His role in shaping me into a ‘scientist’ is invaluable. I would like to thank him especially for support that he showed for me and for my ideas, good teaching and understanding, encouragement and enthusiasm that was always inspiring for me.

I would like to thank Prof. J. Andreas Larsson thanks to whom I could start my adventure with research. Special thanks to Dr. Jakub D. Baran who helped me at the beginning of this road.

I thank Prof. Martyn Pemble, my advisor, and my PhD committee: Lorraine Nagle and Joe O’Brien for encouragement and understanding. I also thank Prof. Jim Greer who always knew what to say.

I thank Prof. Annelies Delabie, Dr. Christoph Adelman and Prof. Kristine Pierloot for kind hospitality during my visit at IMEC. I acknowledge Dr. Ian Povey and Dr. Scott Monaghan for their time and discussion.

I am thankful to many members of Electronic Theory Group and Tyndall National Institute for providing very stimulating and fun environment to study.

I acknowledge the SFI/HEA Irish Centre for High-End Computing (ICHEC) for the provision of computational facilities and support. I acknowledge the financial support derived from the Science Foundation Ireland under grant no. 07/SRC/I1172 (“FORME”, [www.tyndall.ie/forme](http://www.tyndall.ie/forme)).

Finally, I thank my family for being there for me. Special dedication is for my grandmothers: Jadwiga Wronka and Stanisława Klejna.

## Abstract

Atomic layer deposition (ALD) is now used in semiconductor fabrication lines to deposit nanometre-thin oxide films, and has thus enabled the introduction of high-permittivity dielectrics into the CMOS gate stack. With interest increasing in transistors based on high mobility substrates, such as GaAs, we are investigating the surface treatments that may improve the interface characteristics. We focus on incubation periods of ALD processes on III-V substrates. We have applied first principles Density Functional Theory (DFT) to investigate detailed chemistry of these early stages of growth, specifically substrate and ALD precursor interaction. We have modelled the ‘clean-up’ effect by which organometallic precursors: trimethylaluminium (TMA) or hafnium and titanium amides clean arsenic oxides off the GaAs surface before ALD growth of dielectric commences and similar effect on  $\text{Si}_3\text{N}_4$  substrate. Our simulations show that ‘clean-up’ of an oxide film strongly depends on precursor ligand, its affinity to the oxide and the redox character of the oxide. The predominant pathway for a metalloid oxide such as arsenic oxide is reduction, producing volatile molecules or getting oxygen from less reducible oxides. An alternative pathway is non-redox ligand exchange, which allows non-reducible oxides (*e.g.*  $\text{SiO}_2$ ) to be cleaned-up. First principles study shows also that alkylamides are more susceptible to decomposition rather than migration on the oxide surface. This improved understanding of the chemical principles underlying ‘clean-up’ allows us to rationalize and predict which precursors will perform the reaction. The comparison is made between selection of metal chlorides, methyls and alkylamides precursors.

## **1 Introduction**

The microelectronics industry is developing according to Moore's Law, which states that the density of transistors on the chip will double every two years. This enforces their continued scaling to ever smaller dimensions, increasing the complexity and speed of electronic devices. The result has been the dramatic expansion in the technology and communications markets emerging from the global trillion dollar electronics industry [1]. The rapid shrinking of the transistor feature size has led the semiconductor channel length and gate dielectric thickness to also decrease. As a consequence, the Si/SiO<sub>2</sub> based technology is approaching its fundamental physical limits, resulting in the intensive search for alternative materials in order to maintain cost/performance trends of electronic devices. [2] Ideal candidates to replace Si in the transistor channel are III-V semiconductors such as GaAs or InGaAs, due to their higher electron mobility. As a gate dielectric, insulating SiO<sub>2</sub> is being substituted with high-dielectric constant (high-*k*) materials that maintain the same capacitance with much lower leakage current. High-*k* materials are valuable for a wide range of applications, including advanced logic devices, dynamic random access memory (DRAM) capacitors, decoupling filter capacitors for integrated micro-power, and power capacitors for switched-capacitor power conversion.

The introduction of new materials challenges the Si-based microelectronics industry that has been developing for over 30 years. Several fundamental concerns have to be faced in the integration process in order to meet the stringent requirements for reliable devices. A systematic consideration of the required properties has led to the following key properties being identified: electrical properties (permittivity, band gap and band alignment), thermodynamic stability, film morphology, process compatibility, reliability and above all materials compatibility and interface quality [2].

As electronic devices are scaled down into the nanometre regime, their performance comes to depend more and more on material interfaces, and even on individual layers of



atoms. The compatibility of layers at the interface determines mechanical and electrical properties. Additionally, these transition regions can be exploited to obtain desirable properties. For example, in the metal-insulator-semiconductor stack of the field effect transistor (FET) both interfaces to the insulator, with the gate electrode (metal) as well as with the channel (semiconductor), can alter the overall capacitance. If the gate electrode is composed of highly boron doped polycrystalline Si, the interface has to be engineered in order to block dopant diffusion [3]. At the same time, the region in direct contact with the FET channel must exhibit properties maximizing carrier mobility and minimizing leakage. For this purpose an extremely high-quality interface is required. In contrast, interface quality for memory capacitors applications, such as Dynamic Random Access Memory (DRAM), is not as critical. The control of the interface in capacitors is primarily directed at limiting interfacial reactions to keep the total capacitance high for charge storage. Therefore, from a technological point of view, understanding, controlling and designing the properties of materials interfaces is of tremendous importance for these emerging technologies.

## 1.1 High- $k$ dielectric films and III-V substrates

The outstanding electrical properties of the natural high-quality Si/SiO<sub>2</sub> interface present a significant challenge for any alternative. Although III-V/high- $k$  based devices have the potential to replace Si/SiO<sub>2</sub> based transistors, they suffer from having a thermodynamically unstable and electrically low quality interface. This has its origin in the intrinsic complexity of bonding at the III-V interface. Unlike only Si-O bonds, in the example of high- $k$ /GaAs there are possible Ga-O, As-O, high- $k$  metal-Ga, high- $k$  metal-As interfacial bonds. Additionally, bonding constraints at the interface induce defects, dangling bonds, *etc.* Some of these imperfections introduce gap states [4]. The high

density of interface states, in turn, is a cause of the Fermi-level pinning in the GaAs-based interface and is a source of slow traps, decreasing the efficiency of device operation [5-8].

Finding appropriate, stable passivation of the III-V native oxides has been a puzzle for decades. An extensive effort has been put into researching how to increase the control over interfacial oxides between the dielectric and GaAs or InGaAs. It was shown that surface preparations, like cleaning (acids [9, 10],  $\text{NH}_4\text{OH}$  [11, 12]), passivation ( $\text{H}_2\text{S}$ ,  $(\text{NH}_4)_2\text{S}$  [10]), thermal treatment [9] and forming a Si-interfacial passivation layer [12], before high- $k$  growth can reduce the density of interface traps ( $D_{it}$ ).

Crucial for the final interface quality and properties is the method by which the dielectrics are deposited in fabrication lines. The early stages of film growth determine the interface properties and therefore careful optimization of deposition conditions helps with improving device performance. A scalable film deposition technique, which allows controlled growth of ultrathin high- $k$  layers on complex substrates, is atomic layer deposition (ALD) [13].

## 1.2 Atomic layer deposition technique

As mentioned before, more complex electronic components take the form of thin film stacks. This calls for a thin film deposition method that is precise and extremely controllable down to the atomic layer. ALD is such a technique with a unique capability of coating high aspect ratio three-dimensional structures with a conformal material layer of high quality. ALD was originally proposed in 1952 in the Ph.D. thesis of V. B. Aleksovskii and developed in the 1970s and 1980s [14, 15]. ALD is based on sequential self-limiting gas-solid reactions, distinguishing this technique from similar chemical vapor deposition (CVD). ALD is a main technique used to deposit high- $k$  oxides thin films in transistors. Another major application area is for nitrides and metals [16].

Adoption of ALD is not only limited to micro and nano electronics, but also energy, biotechnology, medicine and other advanced technology areas [17].

During CVD, gas phase reactants are injected into the chamber simultaneously and continuously and therefore reactions occur in relatively uncontrolled manner. In ALD, precursor chemicals are strictly separated from each other. In this setting, reactions occur only on the surface substrate in a pulsed manner and between each pulse, an inert gas is used to purge the deposition chamber, removing any volatile by-products. The growth of material layers is thus obtained by repeating the following characteristic steps: 1 – exposure of the substrate to the first gaseous precursor and chemisorption of the first precursor on the substrate; 2 – removal of excess of precursor and gaseous reaction by-products; 3 – exposure of the substrate to the second precursor and reaction of the second precursor with the chemisorbed precursor from previous step; 4 – purge of excess reactants and gaseous by-products. These four steps are defined as one *reaction cycle* and the amount of material obtained in each reaction cycle is referred as *growth-per-cycle* (GPC). Reactions occur on active reactions sites only, which are constant in each cycle. This saturation, limited also by the steric hindrance, results in formation of a monolayer of precursor fragments. After this, no further chemisorption takes place. It is therefore possible to predict and reproduce amount of film grown layer by layer in each cycle.

However, before the deposition process, attention must be paid to the surface preparation and the resultant chemistry. This is particularly relevant when aiming to control the interface. The initial substrate generally has vastly different properties than the deposited film. Thus, if possible, the substrate is stabilized to a known state, for example by thermal treatment or passivation. In general, the initial conditions of the substrate are found to have a strong influence on the growth process. In the so-called initial *transition regime*, ALD growth has been commonly identified as *linear growth*, *inhibited growth* or *substrate-enhanced growth* according to the GPC [18]. It should be noted that the

transition regime is sometimes restricted to just a few cycles, making detection of the interface reactions very difficult unless *in situ* monitoring of adequate sensitivity is employed.

Experimentally, the growth behaviour is generally investigated *via* the GPC rate of deposition per cycle. A linear growth observed already from the early stages of the deposition is the ideal ALD case and it can be observed for metal oxides and metal nitrides grown on SiO<sub>2</sub> [13]; in this case the hydroxyl surface groups easily react with the organometallic molecules. For the deposition of alumina (Al<sub>2</sub>O<sub>3</sub>) using trimethylaluminum (TMA, AlMe<sub>3</sub>, Me = CH<sub>3</sub>) and water (H<sub>2</sub>O) [18], the net growth reaction is:  $2 \text{AlMe}_3 \text{ (g)} + 3 \text{H}_2\text{O (g)} \rightarrow \text{Al}_2\text{O}_3 \text{ (s)} + 6 \text{CH}_4 \text{ (g)}$ .

This is one of the most reliable ALD processes, with an optimum growth rate of 1.1-0.9 Å/cycle at 200-300°C [19, 20]. On the other hand, inhibited initial growth is generally associated with island growth and is therefore characterized by an incubation period that is necessary to activate the surface reactions or to let the islands grow into a complete layer. This incubation (or delay) has been observed for metal oxides grown on H-terminated Si(100) and for most of the ALD processes for metal thin films (*e.g.*, TiN, Ru) [13, 21]. Another type of incubation is substrate-enhanced growth. This is observed on HF-cleaned Ge during hafnia (HfO<sub>2</sub>) deposition [22] but also during deposition of titanium oxide (TiO<sub>2</sub>) thin films on the alumina surface [23]. Transition regime could last a few cycles only, *e.g.* when enhanced, but could also be as long as tens or hundreds of cycles, as in the inhibition case.

Although ALD is a mature technique for high-quality film deposition, successfully adopted for numerous applications, many aspects that control ALD growth are still not sufficiently understood. This is especially true of the chemistry occurring during the transition regime that varies from substrate to substrate and is difficult to monitor but has a tremendous influence on the quality of the film and the interface with the substrate.

What is more, new smart chemistries are constantly needed for the precursor and process development for new ALD technologies. For these reasons, theoretical investigations are an important complement to the experimental research, although also limited in their own way.

### 1.3 Atomic layer deposition processes for high- $k$ dielectric films

Many high- $k$  materials are under consideration as potential candidates to replace SiO<sub>2</sub>, among them transition metal oxides, silicates, rare earth oxides, nanolaminates and mixed oxides. A detailed review of their properties, performance and deposition aspects can be found in reviews by Wilk *et al.*[2], Niinistö *et al.*[24], and recent by Ando[25]. The most frequently studied in ALD high- $k$  research are Al<sub>2</sub>O<sub>3</sub>, HfO<sub>2</sub>, ZrO<sub>2</sub> and TiO<sub>2</sub>.

Most typically water or ozone is employed as a source of oxygen. For instance, water readily reacts with TMA to form alumina [19, 20]. In contrast, strongly oxidizing ozone is needed to remove weakly reactive ligands, such as  $\beta$ -diketonates [24]. A diversity of metal precursors is available for the deposition of high- $k$  films including: halides, alkyls, cyclopentadienyls, alkoxides,  $\beta$ -diketonates, alkylamides, silylamides and amidinates [18]. In this thesis we focus on the representative alkyls, halides and alkylamides briefly described below.

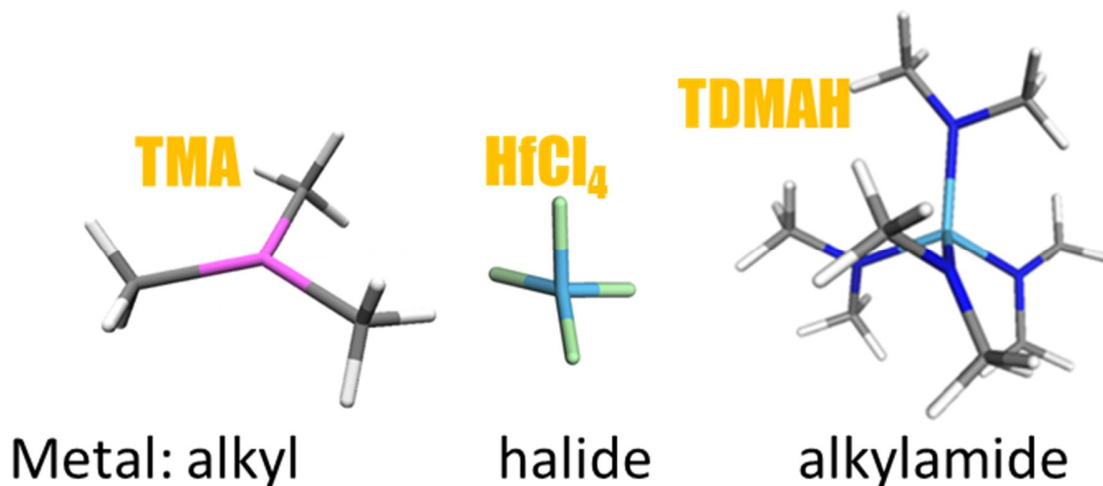


Figure 1-1 Examples of metal alkyl, halide and alkylamide precursor molecules: TMA = Al(CH<sub>3</sub>)<sub>3</sub>, trimethylaluminium; HfCl<sub>4</sub>, hafnium chloride; TDMAH = Hf(N(CH<sub>3</sub>)<sub>2</sub>)<sub>4</sub>, tetrakis(dimethylamido)hafnium. Stick representation: pink Al, light blue Hf, grey C, white H, green Cl, dark blue N.

Alkyls are mostly used for deposition of films containing aluminum and zinc. Those organometallic compounds are highly reactive and those of the electropositive elements are very strong reducing agents featuring polar metal-carbon bonds. Consequently, a variety of materials have been grown from alkyls (oxides, nitrides, sulphides), though they have been used for a rather small selection of elements (mostly groups 12-14). Small alkyl ligands do not cause substantial steric hindrance effects. Hence, in most of the alkyl-based ALD, a rather high GPC is obtained [26], as mentioned before for TMA/H<sub>2</sub>O ALD [27-30]. The by-products formed during the deposition process are typically inert saturated hydrocarbons, which desorb cleanly. A major downside of these precursors is their tendency to decompose at moderately low temperature to metal hydrides and metal alkenes, as in the case of TMA which decomposes above around 350 °C [31-33]. This makes many alkyls unsuitable for ALD processes. The thermal stability of alkyl precursors can be improved by introducing other ligands to form heteroleptic precursors such as ZrCp<sub>2</sub>Me<sub>2</sub> [34] (Cp = C<sub>5</sub>H<sub>5</sub>), HfCp<sub>2</sub>Me<sub>2</sub> [35], Zr(MeCp)<sub>2</sub>Me<sub>2</sub> or Hf(MeCp)<sub>2</sub>Me(OMe) [36]. Contamination of the films obtained from alkyls is usually low; however there is a possibility of carbon and hydrogen residues.

Volatile halide precursors are available for many metals [18] and therefore are exploited for deposition of a variety of materials including not only oxides, but also nitrides and sulphides. Their suitable properties for ALD are: high reactivity, thermal stability, and small ligand size minimizing steric hindrance. Despite many advantages of employing halides in an ALD process, there are a few drawbacks: the GPC is typically small – a fraction of a monolayer of the material to be grown [37, 38]; many halides are solids, which is a challenge in ALD processing; corrosive by-products that can etch the grown film (HCl, HF) [39, 40]; impurities of *e.g.* chlorine or hydrogen that have adverse effects on the film properties [41]. Typical halide-based ALD processes for deposition of *e.g.* HfO<sub>2</sub> or TiO<sub>2</sub> on a semiconductor are HfCl<sub>4</sub>/H<sub>2</sub>O [42, 43] or TiCl<sub>4</sub>/H<sub>2</sub>O [44] at 300°C.

Another group of precursors includes alkylamides, which contain a nitrogen bonded to a metal ( $M(NR_2)_n$ ) [45, 46]. These have been investigated as ALD reactants since the late 1990s [47, 48] and represent a versatile group: they are available for a number of elements and can be used to form a wide range of materials including oxides and nitrides. A big problem of these precursors though is their low decomposition temperature. For instance, Ti(NMe<sub>2</sub>)<sub>4</sub> decomposes already at 150°C [49]. This can influence the GPC, which typically exceeds a monolayer [48, 50], and as a consequence impurities are often found in the films (N, C, H). Nevertheless, due to the relatively weak metal-nitrogen bond, ALD growth reactions with protic compounds occur readily. The facile ALD reactions and high volatility [51, 52] of amides enables efficient deposition at low temperatures, usually around 200°C. Therefore, the final quality of the films they produce depends critically on such process parameters as the length and pressure of the pulses and the deposition temperature used [53, 54]. Hf(NEtMe)<sub>4</sub> and Zr(NEtMe)<sub>4</sub> (Et = C<sub>2</sub>H<sub>5</sub>), known as TEMAH and TEMAZ, are commonly used as ALD as well as CVD precursors [46, 51-53].

## 1.4 ‘Self-cleaning’ ALD

On top of all of the advantages, described in section 1.2, ALD was found to have a salutary effect on high- $k$ /III-V interfaces. An interfacial cleaning mechanism that results in consumption of semiconductor native oxides and in practically sharp dielectric/semiconductor interfaces has been observed during ALD of high- $k$  dielectrics:  $\text{Al}_2\text{O}_3$  [55],  $\text{HfO}_2$  [56, 57],  $\text{TiO}_2$  [58, 59] and  $\text{Ta}_2\text{O}_5$  [60] on GaAs and InGaAs. This has been called ‘clean-up’ or ‘self-cleaning’ [11, 12, 55, 56, 61, 62]. Although removing native oxides is not sufficient to solve the Fermi-level pinning problem in devices [4, 63], it is an important step in the preparation of abrupt interfaces. This indicates that interfacial states can be controlled by optimizing the precursor exposure during the initial cycles of ALD deposition. This phenomenon was confirmed in many experiments, but detailed understanding of the chemistry of the reduction process is still missing.

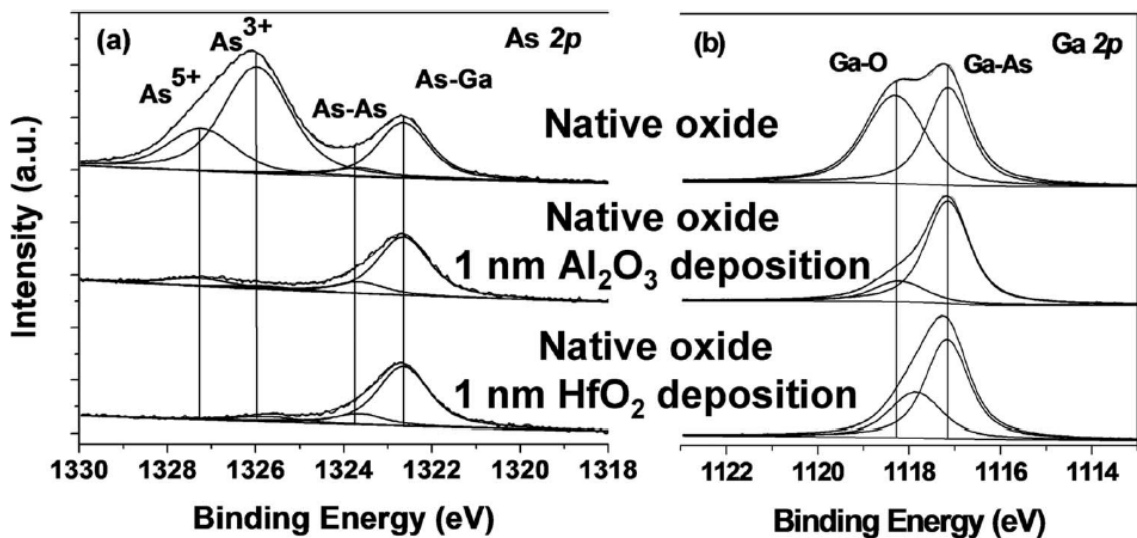


Figure 1-2 (a)As 2p 3/2 and (b) Ga 2p 3/2 XPS spectra showing oxidation state differences for a native oxide and subsequent 1 nm  $\text{Al}_2\text{O}_3$  and  $\text{HfO}_2$  depositions on a GaAs surface. [11]

First reports on the clean-up effect documented an effective passivation of GaAs-based substrates with TMA when depositing  $\text{Al}_2\text{O}_3$  [11]. For  $\text{HfO}_2$  ALD, the clean-up effect was observed mainly when using hafnium alkylamides, with similar behaviour shown by TEMAH or tetrakis(dimethylamido)hafnium (TDMAH,  $\text{Hf}(\text{NMe}_2)_4$ ) [11, 56, 64]. It is



commonly stated that the mechanism responsible for the ‘clean-up’ effect is oxidation state dependent, as well as precursor dependent, suggesting a ligand exchange mechanism [11, 56]. Hinkle *et al.* suggest in their *in situ* analysis of ALD  $\text{Al}_2\text{O}_3$  and  $\text{HfO}_2$  deposition on GaAs surfaces that TMA removes  $\text{As}^{3+}$ , consistent with the  $\text{Al}^{3+}$  oxidation state in  $\text{Al}_2\text{O}_3$ , while TEMAH should be more likely to remove higher oxidation states ( $\text{As}^{5+}$ ,  $\text{Ga}^{5+}$ ,  $\text{Ga}^{4+}$ ), since Hf is in the 4+ oxidation state in  $\text{HfO}_2$  (see [Figure 1-2](#)). On the other hand there are studies showing that the reaction mechanism of ‘clean-up’ appears to be nonselective toward reducing different As oxides [58, 62]. This discrepancy might be due to different surface preparations and thermal treatments, and resultant differences in the chemistry of native oxides. Scanning transmission electron microscopy (STEM) shows a 20-25 Å thick Ga-rich oxide layer on gallium arsenide [9], 10 Å thick after heating at 320°C [62], with increased As concentration near the GaAs surface. There is the possibility of thermal conversion of  $\text{As}_2\text{O}_5$  into  $\text{As}_2\text{O}_3$  in the low pressure of the ALD chamber, with excess  $\text{O}_2$  given off as a by-product [62, 65]. There may also be thermal conversion of mixed Ga/As oxide into predominantly  $\text{Ga}_2\text{O}_3$  [62]. Indeed, if the Ga-O bond is stronger than As-O, then this may explain why  $\text{AsO}_x$  loses oxygen more easily than  $\text{GaO}_x$  in ‘clean-up’ with TMA. The experimental fact is that the initial TMA pulse (without a pulse of oxygen source) results in the formation of  $\text{AlO}_x$ , where the oxygen is presumably scavenged from  $\text{AsO}_x$  or  $\text{GaO}_x$  present on the substrate [58, 63].

A recent study shows that ALD processes utilizing alkylamide precursors featuring Ti (tetrakis(dimethylamido)titanium, TDMAT,  $\text{Ti}(\text{NMe}_2)_4$ ) or Ta (pentakis(dimethylamido)tantalum, PDMAT,  $\text{Ta}(\text{NMe}_2)_5$ ) also result in the same interfacial cleaning effect while depositing  $\text{TiO}_2$  or  $\text{Ta}_2\text{O}_5$  respectively [59, 60]. These observations indicate that the common requirement for self-cleaning is the use of organometallic or metalorganic precursors. However, the examples of the purely inorganic  $\text{HfCl}_4$  and  $\text{TiCl}_4$  ALD processes contradict this assumption. ‘Clean-up’ is also

observed with the use of these precursors by Delabie *et al.* [57] and Granados-Alpizar and Muscat [58] but was not reported by Frank *et al.* [9].

Common experimental observations are found for interfacial cleaning with TMA and alkylamide precursors. Generally arsenic oxides are easier to remove than gallium oxides. Higher oxidation states of both As ( $\text{As}^{5+}$ ) and Ga ( $\text{Ga}^{3+}$ ) are more sensitive to reduction. Accumulation of metallic arsenic – arsenic suboxide at the interface has been observed for TMA based ALD [63] (see [Figure 1-3](#)) and alkylamide based ALD [64, 66] (see [Figure 1-4](#)). It seems that elevating the temperature of the process significantly enhances the clean-up abilities of alkylamides, and this differentiates these processes from TMA-based clean-up [10, 60] (see also [Figure 1-4](#)). Granados-Alpizar and Muscat show differences in surface reactions during GaAs exposure to TMA and  $\text{TiCl}_4$  pulses [58]: TMA deposits an  $\text{Al}_2\text{O}_3$  layer and removes a portion of As from the surface, whereas  $\text{TiCl}_4$  removes O and leaves the surface passivated with Cl atoms. Both precursors remove the native oxide layer, but the mechanisms underlying this process seem to be fundamentally different. The mechanism for removing oxides with  $\text{HfCl}_4$  differs also from the one for  $\text{TiCl}_4$ : the growth of hafnium oxide is enhanced [57] and growth of titanium oxide is inhibited [58].

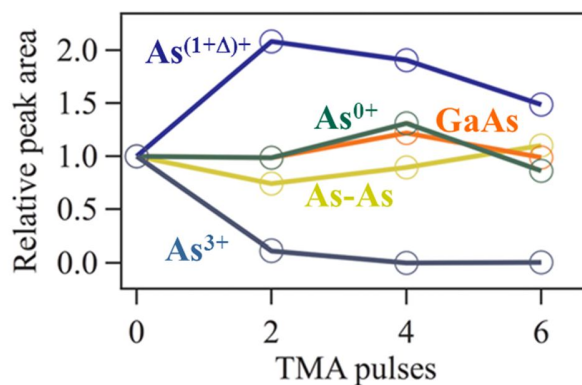


**Figure 1-3** The peak area relative to the initial values of As 3d spectra of the native oxide covered GaAs and after 2, 4, and 6 TMA pulses. [63]

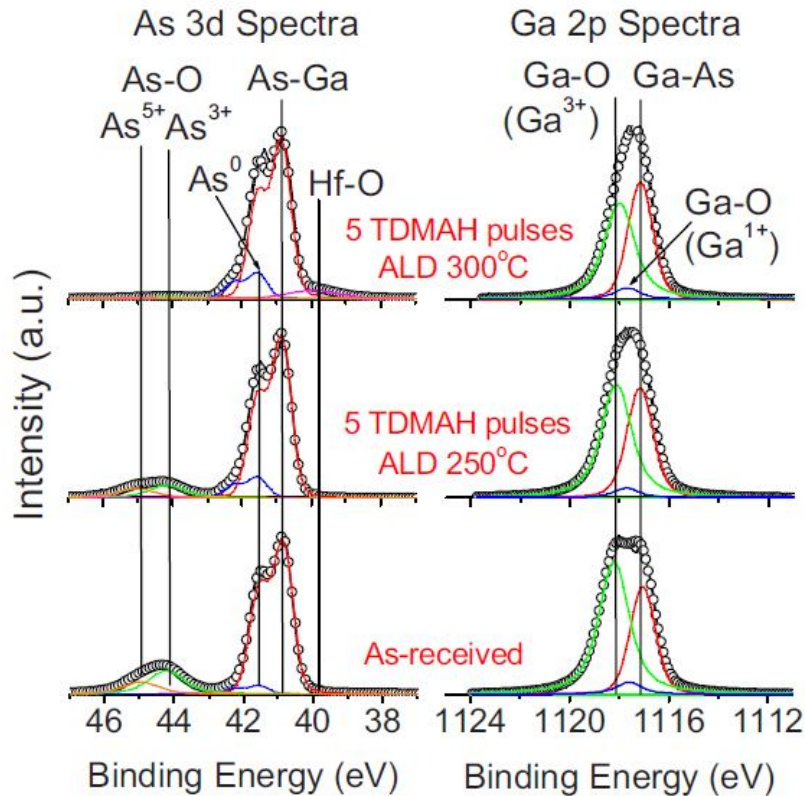


Figure 1-4 XPS As 3d and Ga 2p<sub>3/2</sub> spectra of as-received native GaAs and after exposure of native GaAs to five TDMAH pulses inside ALD chamber at ALD temperatures of 250 and 300 °C. [66]

These extensive and sometimes conflicting studies on interfacial self-cleaning show how little is understood about the chemistry occurring in the initial cycles of deposition of dielectrics.

## 1.5 Outline of the work

Many open questions remain about the reaction of ALD precursors with technologically-important substrates during the early stages of ALD growth when an interface is formed. In this thesis we report theoretical investigation of reactions occurring on III-V substrates, in particular on their native oxides, and on a silicon nitride substrate, during deposition of dielectric materials. Using computational modelling methods we are investigating the surface treatments that may improve the interface characteristics. Particular attention is paid to the TMA reagent itself and its interaction with III-V oxides

(mainly As(III) oxide), SiO<sub>2</sub> and Si<sub>3</sub>N<sub>4</sub>, as this precursor was widely used in experiment and the deposited films showed good electrical properties [67]. These results are in the chapters 3 and 4. Another important precursor family showing self-cleaning ALD, as described above, are metal alkylamides. In chapter 5 we investigate decomposition of the alkylamide ligand in contact with As(III) oxide, looking at redox properties of this ligand. In chapter 6, we extend this to consideration of mechanistic paths describing the interaction of tetrakis(dimethylamido)hafnium also with As(III) oxide. Also in chapter 5, a model for comprehensive study of reaction of different precursors with III-V native oxides, including As (III), Ga(III), In(III) oxides, is developed. The study covers the metals Ta(V), Ti(IV), Zr(IV), Hf(IV), Al(III), Mg(II) combined with methyl, amide and chloride ligands. The results chapters are preceded by the description of the framework in which the calculations were conducted (chapter 2). Numbering for tables and figures includes their chapter number.

## 2 Methods of research

The major aim of the studies presented in this thesis was to assist and to complement experiment and as a result to obtain better understanding of the mechanisms occurring during initial ALD cycles of dielectric films. In this thesis atomic-scale simulation is used to explain various experimental results with the aim of leading to new insights, and in particular of answering the question: how to improve interface properties? Our simulation assists ALD monitoring techniques, such as X-ray photoelectron spectroscopy (XPS), synchrotron radiation photoelectron spectroscopy (SRPS), spectroscopic ellipsometry (SE), quadruple mass spectrometry (QMS), infrared spectroscopy (FTIR), time of flight secondary ion mass spectroscopy (ToF SIMS) and X-ray reflectivity (XRR). Computational modelling offers complementary analysis to these techniques by providing a much greater insight into the reaction mechanisms, specifically by revealing intermediate steps that are not easily observed experimentally.

### 2.1 First principles methods

Modeling ALD mechanisms requires a method that is highly accurate in determining changes in the structure and bonding when gaseous precursors interact with solid materials. First principles methods offer accurate prediction of structures and energies of hypothetical atomic-scale models, without fitting to experiment. This is obtained by approximately solving the quantum mechanical Schrödinger equation for the electronic structure of discrete atoms explicitly located in space.

The original first principles (or *ab initio*) method, Hartree Fock (HF) theory, provides a methodology for the approximate determination of a wavefunction of a quantum many-body system (atoms, molecules, nanostructures). The fundamental assumption of HF theory is that each electron sees all of the other electrons as an average neglecting electron correlation. This can lead to large deviations from experimental results when

properties are derived from the HF wavefunction. So-called “post-HF” methods, or high-level *ab initio* methods, attempt to include electron correlation in the multi-electron wave function. However these are too computationally expensive to be applied to large systems (>100 atoms). Approximate density functional theory (DFT) provides a higher level of accuracy at roughly the same computational cost as HF (by incorporating some effects of both exchange and correlation of electrons). These practical aspects make DFT one of the widely used first principles techniques.

### 2.1.1 Density functional theory

The DFT method is based on the Hohenberg-Kohn theorems that prove that, instead of needing a molecular wavefunction for each electron, the entire electron probability density of the molecule is sufficient to solve the Schrödinger equation. The first theorem demonstrates that the ground state properties of a many-electron system are uniquely determined by an electron density that depends on only 3 spatial coordinates. The second theorem defines an Energy functional for the system and proves that the correct ground state electron density minimizes this energy functional.

Nevertheless, the commonly-used Kohn-Sham formalism of DFT [68] does make use of wavefunctions in a similar way as HF theory. Finding the density of mutually interacting electrons is done by computing non-interacting pseudo-electrons moving in an effective potential that partially accounts for electron correlation and exchange. This non-interacting system of pseudo-electrons is built up from a set of orbitals that together form a single-particle Slater determinant. The Slater determinant is an exact wavefunction of a system of non-interacting particles. The effective potential should include the external potential and the effects of the interactions between the electrons. By careful selection of this effective potential, the density of the created system can match the ground state density of the desired system of interacting electrons. As a consequence, DFT then looks

formally like a single-particle theory, although many-body effects are still included *via* the so-called exchange-correlation functional.

In practice, the utility of the theory rests on the approximation used for the exchange-correlation functional [68], which is the sum of the error made in using a non-interacting kinetic energy and the error made in treating the electron-electron interaction classically. Many different functionals of the density have been proposed for use in the Hamiltonian, falling into the main categories of the local density approximation (LDA) or generalized gradient approximation (GGA) often mixed with HF exchange (hybrid DFT). The exchange-correlation energy functional approximated by LDA depends solely upon the value of the electronic density at each point in space. GGA also takes into account the gradient of the density at the same coordinate. Hybrid functionals are approximations to the exchange-correlation energy functional that incorporate a portion of the exact exchange energy functional from HF theory. Hybrid functionals often perform better than LDA or even GGA approaches in predicting molecular geometries.

The performance of a family of density functional methods was evaluated *inter alia* by Johanson *et al.* [69]. The systematic calculations of equilibrium geometries, dipole moments, harmonic vibrational frequencies, and atomization energies were performed for a set of 32 small neutral molecules by six different local and gradient-corrected DFT methods, and also by the *ab initio* methods HF, 2nd order Møller-Plesset perturbation theory (MP2), and quadratic configuration interaction with single and double substitutions (QCISD). They found that even the simplest LDA reproduces geometries and vibrational frequencies with satisfactory accuracy; however binding energies are too large. Gradient corrections do not yield more accurate structural data and vibrational frequencies, but significantly improve binding energies, even over the MP2 method.

DFT generally gives a good description of classical two-centre bonds, non-classical multi-centre bonds, metallic and polar bonding, and binding energies, reproduces geometries with satisfactory accuracy and calculates correct vibrational frequencies. Systems of up to 1000 atoms can be explicitly calculated with DFT using today's computing power. However, due to 'self-interaction' in the DFT density, there are difficulties to properly describe intermolecular interactions, especially van der Waals forces (dispersion), charge transfer excitations, curve crossing at transition states, some strongly correlated systems and in calculations of the band gap in semiconductors. Hence, DFT within the GGA of Perdew and Wang (PW91) [70] for the exchange-correlation energy is applied in this thesis as a reliable method for computation of the ground state electronic structure and ALD reaction energies, exercising caution regarding its limitations.

### 2.1.2 High-level *ab initio* computations

Considering TMA as a superb precursor for self-cleaning ALD led us to an investigation of the stability of this molecule. Therefore, metal-ligand dissociation energetics have to be evaluated in light of the clean-up mechanisms that are investigated in chapter 3. For the proper description of the dissociation process and benchmarking DFT applicability for considered system we performed high-level *ab initio* computations: MP2 [71], multi-configurational methods [72]: complete active space self-consistent field (CASSCF) and complete active space perturbation theory (CASPT2), coupled cluster theory (CC) [73]: single and double excitation (CCSD), single, double and triple excitations (CCSD(T)).

MP2 treats the correlation as a perturbation to the single-reference HF solution by means of Rayleigh–Schrödinger perturbation theory. This method is an improvement over HF, but there can be difficulties with the convergence of the wavefunction depending on



the specific system and basis set. Multi-configurational methods find their application for molecular ground states which are quasi-degenerate with low lying excited states, including bond breaking processes. This is possible through formalism that, rather than the single determinant wavefunction, of the HF and MP2 methods, uses instead a linear combination of several determinants to build the wavefunction. The difficulty of the CAS method is the selection of the orbitals to include in the active space, which requires considerable *technical* experience. In contrast, in the CC technique, a single determinant wavefunction is constructed using an exponential cluster operator that accounts for electron correlation. This operator can be truncated to the desired level of excitation from a given reference state. Because of the elusiveness of describing electron correlation, these methods are computationally time consuming and tractable for fewer than 100 atoms.

The MP2 and CASSCF/CASPT2 calculations were performed with MOLCAS [74], while the CCSD/CCSD(T) were carried out with MOLPRO [75]. An extended all-electron ano-rcc basis set [76] and aug-cc basis sets [77, 78] was used.

## 2.2 Approach to materials modeling

### 2.2.1 Bulk computations

DFT with 3-D periodic boundary conditions and a plane wave basis set is appropriate for the description of properties of crystalline materials, as implemented within the VASP package [79]. It is suitable for modeling reactions taking place on metal oxide surfaces ( $\text{As}_2\text{O}_3$ ,  $\text{In}_2\text{O}_3$ ,  $\text{Ga}_2\text{O}_3$ ).

The core electrons were described with ultrasoft pseudopotentials (USPP) [80, 81] projected into real space and valence electrons were described with a plane-wave basis with a kinetic energy cutoff of 396 eV unless otherwise noted. A sparse Monkhorst-Pack  $k$ -point grid was used to sample reciprocal space. A conjugate-gradient algorithm was

used for ionic relaxation with all ions relaxed until the forces on the ions were less than 0.02 eV/Å.

High accuracy was used for bulk oxide calculations: convergence of energies to  $10^{-4}$  eV with respect to coordinates of ions and cells, 130% of the standard plane-wave cutoff energy, convergence with respect to  $k$ -point sampling. The total energy versus volume for all models of the bulk oxide structures was optimized resulting in equilibrium lattice parameters that agreed well with experiment (with deviation less than 2%) [82]. Lattice parameters and space groups, along with  $k$ -point sampling for all bulk structures considered in this work are given in [Table 2-1](#).

bulk	Structure/Space group	Lattice parameters [Å, °]	$k$ -point sampling
$\alpha$ -As	Rhombohedral, R-3m No. 166	$a = 4.198; \alpha = 54.125$	15×15×15
$\alpha$ -Al <sub>2</sub> O <sub>3</sub>	Hexagonal, R-3c No. 167	$a = 4.849; c = 13.123$	4×4×2
As <sub>2</sub> O <sub>3</sub>	Cubic, FD-3M No.227	$a = 11.073^*$	2×2×2
$\alpha$ -As <sub>2</sub> O <sub>5</sub>	Orthorhombic, P212121 No. 19	$a = 9.078, b = 8.871, c = 4.857$	2×2×4
<i>zincblende</i> -GaAs	Cubic, F43M No. 216	$a = 5.747$	4×4×4
Ga <sub>2</sub> O <sub>3</sub>	Monoclinic, C2/M No. 12	$a = 12.300, b = 3.100, c = 5.900, \beta = 104^\circ$	4×8×6
HfO <sub>2</sub>	Monoclinic, P21/C No.14	$a = 5.132, b = 5.206, c = 5.305, \beta = 99.67^\circ$	4×4×4
<i>zincblende</i> -InAs	Cubic, F43M No. 216	$a = 6.169$	8×8×8
In <sub>2</sub> O <sub>3</sub>	Cubic, IA-3 No. 206	$a = 10.298$	4×4×4
MgO	Cubic, FM-3M No. 225	$a = 4.237$	6×6×6
Ta <sub>2</sub> O <sub>5</sub>	Orthorhombic, PMMM No. 47	$a = 6.490, b = 3.684, c = 7.763$	4×6×4
<i>rutile</i> -TiO <sub>2</sub>	Tetragonal, P42/MNM No.136	$a = 4.657, c = 2.978$	4×4×6
ZrO <sub>2</sub>	Monoclinic, P21/C No.14	$a = 5.198, b = 5.272, c = 5.367, \beta = 99.45^\circ$	4×4×4

**Table 2-1 Lattice parameters computed with periodic USPP-PW91 DFT for the bulk of As, GaAs and InAs and oxides of Al(III), As(III), As(V), Ga(III), Hf(IV), In(III), Mg(II), Ta(V), Ti(IV) and Zr(IV). The Monkhorst-Pack  $k$ -point sampling scheme for each structure is listed. Geometry optimization was carried out until energies were converged to  $10^{-4}$  eV with respect to coordinates of ions and cells. Plane-wave cutoff energy was 495 eV for all systems.**

A special case was the model for arsenic (III) oxide since its crystalline structure did not allow us to perform cell shape optimization within DFT. This crystalline form, known as arsenolite, is the polymorph of solid arsenic (III) oxide that has been reported to grow as a result of oxidation of the GaAs surface [83, 84], and therefore was chosen here as a model for the oxidized III-V substrate. Arsenolite is a molecular solid built of a cubic tetrahedral array of  $\text{As}_4\text{O}_6$  molecules with rings of four connected pyramidal  $\text{AsO}_3$  units that share O atoms [85, 86]. The intermolecular interaction is of the van der Waals type. Present DFT methods are not able to completely describe this type of weak interaction [87, 88] and therefore experimental lattice constants had to be used for the  $\text{As}_2\text{O}_3$  bulk model [85]. We are confident that this has no adverse effect on the reactions studied here as we draw no conclusions about the actual structure of  $\text{As}_2\text{O}_3$  or dielectric layers layers. Ions were fully relaxed within the fixed  $\text{As}_2\text{O}_3$  cell and the calculated geometry parameters compare well with the experimental values, with the deviation around 2%, in line with other theoretical results [89, 90] (see [Table 2-2](#)).

geometry parameters	bulk	bulk (experiment) [85]	1-layer slab (010)
$R(\text{As-O})$	1.823 Å	1.786(3) Å	1.819 Å
$\angle (\text{As-O-As})$	127.5°	128.7(3)°	126.6°
$\angle (\text{O-As-O})$	99.1°	98.4°	99.8°

**Table 2-2 Computed geometrical parameters for the  $\text{As}_2\text{O}_3$  bulk and its (010) oriented slab within a cell fixed at the experimental lattice parameters. For the slab structure, given values are an average for the entire supercell.**

## 2.2.2 Constructing surface model

Most of the ALD mechanisms were investigated on a model  $\text{As}_2\text{O}_3$  surface as clean-up was shown to be the most effective for this native oxide. A model of the  $\text{As}_2\text{O}_3$  surface was built by cleaving the relaxed bulk structure at the low-index (010) plane between molecular units. The (010) plane is the natural cleavage direction which creates a surface free of dangling bonds. To verify stability of the (010) oriented surface, its formation

energy ( $\sigma$ ) as a function of slab thickness was tested for slabs up to 20 layers thick using [91]:

Equation 2-1

$$\sigma = \lim_{N \rightarrow \infty} \frac{1}{2} (E_{slab}^N - NE_{bulk}),$$

where  $E_{slab}^N$  is the total energy of  $N$ -layer slab and  $E_{bulk}$  is the bulk total energy. As can be seen in **Figure 2-1**, the surface energy is determined to be below  $0.02 \text{ J/m}^2$ . This almost zero-surface-energy correlates well with the weak interaction between molecular units in the crystalline structure, although, as noted above, DFT-PW91 does not describe the interaction correctly. Similar results have been obtained by Ganduglia-Pirovano and Sauer for surface optimization of the molecular solid  $\text{V}_2\text{O}_5$  [92]. The consequence is that even a very thin slab is adequate to simulate the (010) surface and in this study we use a 1-layer slab totalling 2 molecular units of  $\text{As}_4\text{O}_6$  (20 atoms) per  $1 \times 1$  simulation cell.

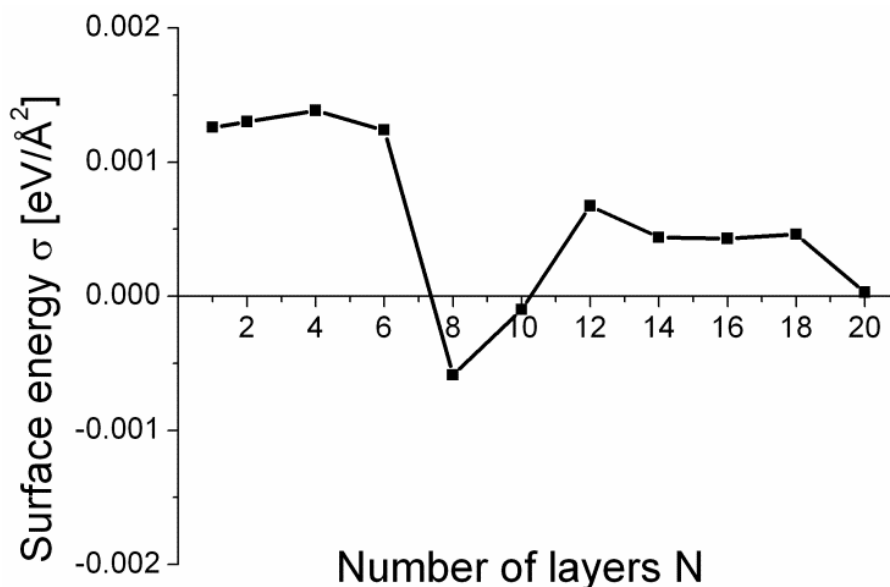


**Figure 2-1.** Surface formation energies ( $\sigma$ ) for  $\text{As}_2\text{O}_3$  (010) as a function of the slab thickness (number of layers  $N$ , where a layer is defined as a two molecular units of  $\text{As}_4\text{O}_6$ ).

### 2.2.3 *Ab initio* thermodynamics

ALD experiments are conducted at constant temperature and pressure and therefore the appropriate thermodynamic potential to consider is the Gibbs free energy,  $G(T,p)$ . Combining 0 K DFT calculations with statistical thermodynamics for the gas-phase chemical potentials,  $\mu(T,p)$ , allows one to bridge to any  $(T,p)$ -conditions of realistic experiments.

We neglect the constant contribution to entropy ( $S$ ) from solids and solid surfaces with adsorbates since  $S_t$  and  $S_r$  for surfaces are approximately zero and  $S_v$  is approximately constant during the reaction,  $\Delta S_v = 0$  ( $t$  – translational,  $r$  – rotational,  $v$  - vibrational modes of motion of the molecule). We have computed only the entropies of gaseous ( $g$ ) species as ideal gases from

Equation 2-2

$$S = R \ln q$$

where  $R$  is the gas constant and

Equation 2-3

$$q = q_t q_r q_v$$

is a molecular partition function factorized into contributions from each mode of motion, which are in turn obtained from vibrational analysis. Taking  $\Delta S = 0$  for reactions exclusively on the surface means that the Gibbs free energy profiles closely resemble the DFT potential energy surfaces. We treat in a more accurate way adsorption and desorption processes. During these reaction steps a gaseous molecule loses/gains translational and rotational modes of motion and therefore

Equation 2-4

$$\Delta S = -R \ln(q_t q_r)$$

for adsorption and

Equation 2-5

$$\Delta S = R \ln(q_t q_r)$$

for desorption.

Gibbs free energies ( $\Delta G(T,p)$ ) are calculated from:

Equation 2-6

$$\Delta G(T,p) = \Delta E^{0\text{K}} + \Delta\mu(T,p),$$

where  $\mu$  is the chemical potential of gaseous species obtained from vibrational analysis given by:  $ZPE - RT \ln q$ .

In general, if we consider a surface interacting with the environment, *e.g.* with oxygen gas, then the free energy of the surface depends on the oxygen pressure and temperature. The stability of native oxides, at a given temperature and a given O<sub>2</sub> partial pressure, is reported in chapter 3.2. The first principles thermodynamics formalism according to Reuter *et al.* [93] was used for these calculations. As an example we quote here the formulation of the Gibbs free energy for reaction **(16)** in chapter 3.2, that is:

Equation 2-7

$$\Delta G(T,p) = \mu_{\text{O}_2}(T,p) + \Delta E^{0\text{K}}_{\text{bulk.}}$$

When the surface is in thermodynamic equilibrium with the gas phase:

**Equation 2-8**

$$\mu_{\text{O}_2}(T,p) = \mu_{\text{O}_2}(T,p^\circ) + RT\ln(p/p^\circ),$$

where empirical values of  $\mu_{\text{O}_2}(T,p^\circ)$  are available from thermodynamics tables [94].

Geometry optimization for gas species was performed with the plane wave periodic code using a big simulation box, cubic or rhombohedral, with  $a = 15 \text{ \AA}$  lattice constant, ensuring enough space for the gas molecule to be effectively surrounded by vacuum and unhindered by its periodic images. Six  $k$ -points were located at the edges of the first Brillouin zone. However, as outlined above,  $\Delta S$  was computed *via* vibrational analysis, and this was carried out using a non-periodic code.

The vibrational analysis was performed with the TURBOMOLE suite of quantum chemical programs [95]. This program is well suited for the calculation of large molecules and clusters and it utilizes atom-centred gaussian basis sets [96]. DFT was employed within the GGA parametrization by Perdew-Burke-Ernzerhof (PBE) [97], the resolution-of-the-identity (RI) approximation [98, 99] and atom-centred triple-zeta valence basis functions, augmented by double polarization functions, TZVPP2 [100].

### 2.3 Population analysis

Partial atomic charges can be estimated from the quantum chemical calculations. These can help to accurately describe the complex interaction between atoms in molecules and in the solid state. In this thesis Bader population analysis was employed [101]. This approach is available as a Transition State Tools (TST) for VASP developed at the University of Texas [102-104].

The Bader partitioning is more robust than other population analysis methods, *e.g.* Mulliken population analysis, because it is based upon the charge density as opposed to wavefunction based methods. This is an advantage because, in a converged electronic structure calculation, the charge density is insensitive to the basis set used, unlike the

wavefunction. The charge density is used to divide space within molecular systems into atomic (Bader) volumes. Each volume contains a single charge density maximum, and is separated from other volumes by surfaces on which the charge density is a minimum normal to the surface. The dividing surfaces separating these volumes lie in the bonding regions between atoms.

For the redox reactions that arise in our mechanistic investigations, differences in Bader atomic charges,  $\Delta q$ , are analyzed to determine the chemical state of intermediates. The sign convention used in this work is that  $\Delta q < 0$  means loss (oxidation of an atom) and  $\Delta q > 0$  means gain (reduction of an atom) of electron population on atoms taking part in the considered reaction.

## 2.4 Transition state searches

Finding saddle points on the potential energy hypersurface is a very difficult task in chemical kinetics and requires much more input than straightforward location of minima. However, as commonly stated, ALD is driven by kinetics rather than thermodynamics; hence this effort is worthwhile. For this work, reactions pathways are computed with DFT for mechanisms of decomposition of Hf alkylamide precursor for hafnia deposition and are presented in chapter 6. These results though, have to be viewed as some general suggestions, not as accurate computations. Computing activation energies with single determinant *ab initio* methods gives uncertain errors when the wavefunction changes strongly at the transition state (TS). Accuracy can be reliably obtained by post-HF methods, however these are costly and not straightforward to implement (gradients are sometimes not available), as mentioned before, and are not applied to the search for transition states in this thesis.

Our strategy for TS searches was to generate a sequence of configurations that interpolate between reactant and product states and to optimise to the minimum-energy



path with the nudged elastic band method (NEB) [105] also available as TST for VASP. Convergence is poor for these calculations, making them computationally time-consuming. There are some advantages of using NEB for large and complex systems: (i) the Hessian matrix is not necessary; (ii) the saddle point does not need to be close to the initial pathway chosen; (iii) the full minimum-energy pathway is obtained showing intermediate minima and the connectivity between the stationary points. NEB calculations reported in this thesis were performed with up to 8 images for each reaction pathway. The damped molecular dynamics algorithm for ionic relaxation was found to be appropriate for the regarded system. Around 1000 steps were needed to converge forces on atoms below  $0.05 \text{ eV/\AA}$ .

### 3 TMA - clean-up reagent for atomic layer deposition of alumina onto III-V substrates

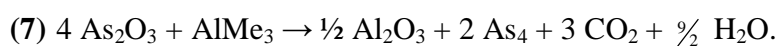
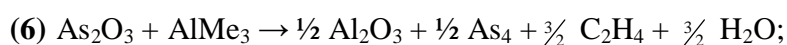
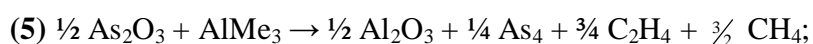
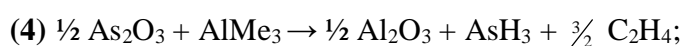
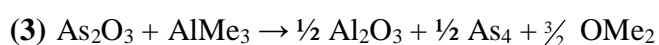
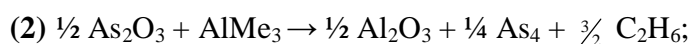
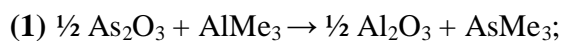


Trimethylaluminium has been found to achieve in situ ‘clean-up’ of the oxides of GaAs and InGaAs before atomic layer deposition (ALD) of alumina. Here we propose seven reaction mechanisms for ‘clean-up’, featuring exchange of ligands between surface atoms, reduction of arsenic oxide by methyl groups and desorption of various products. We use first principles Density Functional Theory (DFT) to determine which mechanistic path is thermodynamically favored. We also discuss the statistical likelihood of the interdependent pathways. ‘Clean-up’ of an oxide film is shown to strongly depend on electropositivity of the precursor metal, affinity of the precursor ligand to the oxide and the redox character of the oxide. The predominant pathway for a metalloid oxide such as arsenic oxide is reduction, producing volatile molecules or getting oxygen from less reducible oxides. We therefore predict that ‘clean-up’ of III-V native oxides mostly produces As<sub>4</sub> gas, but also GaAs solid or InAs solid. Most C is predicted to form C<sub>2</sub>H<sub>6</sub> but with some C<sub>2</sub>H<sub>4</sub>, CH<sub>4</sub> and H<sub>2</sub>O. An alternative pathway is non-redox ligand exchange, which is a pathway that allows non-reducible oxides to be cleaned-up.

Published as: Klejna, S.; Elliott, S. D., *First-Principles Modeling of the “Clean-Up” of Native Oxides during Atomic Layer Deposition onto III–V Substrates*. The Journal of Physical Chemistry C 2012, 116 (1), 643-654.

### 3.1 Introduction

The aim of this chapter is to find the mechanism responsible for ‘clean-up’, *i.e.* for reduction or removal of As-O bonds on an oxidized GaAs substrate in the very first pulse of TMA during ALD of Al<sub>2</sub>O<sub>3</sub>. In particular we focus on the role of TMA as an agent to clean off the arsenic (III) oxide. We seek quantitative information on the energetics ( $\Delta E$ ), thermodynamics of the process ( $\Delta G$ ) and structures of intermediates and by-products, so that these can then be searched for experimentally. Specifically, we use plane wave Density Functional Theory (DFT) to compute energetics of the reaction pathways leading to products that match experiment. We investigate several different reactions (1)-(7) with different sets of volatile products of As, C and H, as no remnant products containing these elements were detected at the GaAs/AlO<sub>x</sub> interface [11, 61]. Reaction energetics are computed per one TMA molecule which allows comparison between competitive products.



We take two approaches to modelling the candidate ‘clean-up’ reactions (1)-(7). In the first approach we model crystalline oxides and isolated gas-phase molecules and thus determine the ‘bulk’ thermodynamics of the reactions (section 3.2). In the second approach, we consider the explicit steps that occur as the TMA molecule reacts with a surface covered with arsenic oxide. The reaction is divided into three parts: TMA

adsorption (section 3.3), methyl transfer (section 3.5) and desorption of volatile products (section 3.7). Our notation is to use arabic numerals for overall reactions, including the candidates for ‘clean-up’. Lower case letters and arabic numerals correspond to the intermediate ‘clean-up’ reactions, *e.g.* **2a**, **2b** *etc.* are intermediates for reaction (2). Surface models for adsorption, methyl transfer and models for surfaces after desorption of gaseous molecules are labelled with upper case letters **A-Z**.

### 3.2 Bulk potential energies

To have a first overview on the energetics of ‘clean-up’ reactions (1)-(7) we have used DFT to compute the potential energy at zero temperature  $\Delta E_{(b)}$  and the thermodynamic Gibbs free energy at various temperatures  $\Delta G_{(b)}$  for bulk structures in each reaction.

**Table 3-1** and **Figure 3-1** show the computed change in energy at 573 K ( $\Delta G_{(b)}^{573K}$ ) and at 0 K ( $\Delta E_{(b)}^{0K}$ ) for proposed ‘clean-up’ reactions (1)-(7). **Figure 3-1** shows also the temperature dependence over the range 0 – 1200 K of the free energy for reactions (1)-(7).

reaction	$\Delta G_{(b)}^{573K}$	$\Delta E_{(b)}^{0K}$
(1) $\frac{1}{2} \text{As}_2\text{O}_3 + \text{AlMe}_3 \rightarrow \frac{1}{2} \text{Al}_2\text{O}_3 + \text{AsMe}_3$	-4.0	-4.4
(2) $\frac{1}{2} \text{As}_2\text{O}_3 + \text{AlMe}_3 \rightarrow \frac{1}{2} \text{Al}_2\text{O}_3 + \frac{1}{4} \text{As}_4 + \frac{3}{2} \text{C}_2\text{H}_6$	-5.6	-5.2
(3) $\text{As}_2\text{O}_3 + \text{AlMe}_3 \rightarrow \frac{1}{2} \text{Al}_2\text{O}_3 + \frac{1}{2} \text{As}_4 + \frac{3}{2} \text{OMe}_2$	-4.6	-3.2
(4) $\frac{1}{2} \text{As}_2\text{O}_3 + \text{AlMe}_3 \rightarrow \frac{1}{2} \text{Al}_2\text{O}_3 + \text{AsH}_3 + \frac{3}{2} \text{C}_2\text{H}_4$	-3.6	-2.3
(5) $\frac{1}{2} \text{As}_2\text{O}_3 + \text{AlMe}_3 \rightarrow \frac{1}{2} \text{Al}_2\text{O}_3 + \frac{1}{4} \text{As}_4 + \frac{3}{4} \text{C}_2\text{H}_4 + \frac{3}{2} \text{CH}_4$	-5.8	-4.5
(6) $\text{As}_2\text{O}_3 + \text{AlMe}_3 \rightarrow \frac{1}{2} \text{Al}_2\text{O}_3 + \frac{1}{2} \text{As}_4 + \frac{3}{2} \text{C}_2\text{H}_4 + \frac{3}{2} \text{H}_2\text{O}$	-6.3	-3.1
(7) $4 \text{As}_2\text{O}_3 + \text{AlMe}_3 \rightarrow \frac{1}{2} \text{Al}_2\text{O}_3 + 2 \text{As}_4 + 3 \text{CO}_2 + \frac{9}{2} \text{H}_2\text{O}$	-15.7	-2.5

**Table 3-1. Gibbs free energies at 573 K and energies at 0 K for possible products of ‘clean-up’ reaction of  $\text{As}_2\text{O}_3$ . Given energies are bulk potential energies. All energies are shown in eV per  $\text{AlMe}_3$  molecule reacting with arsenic (III) oxide.**

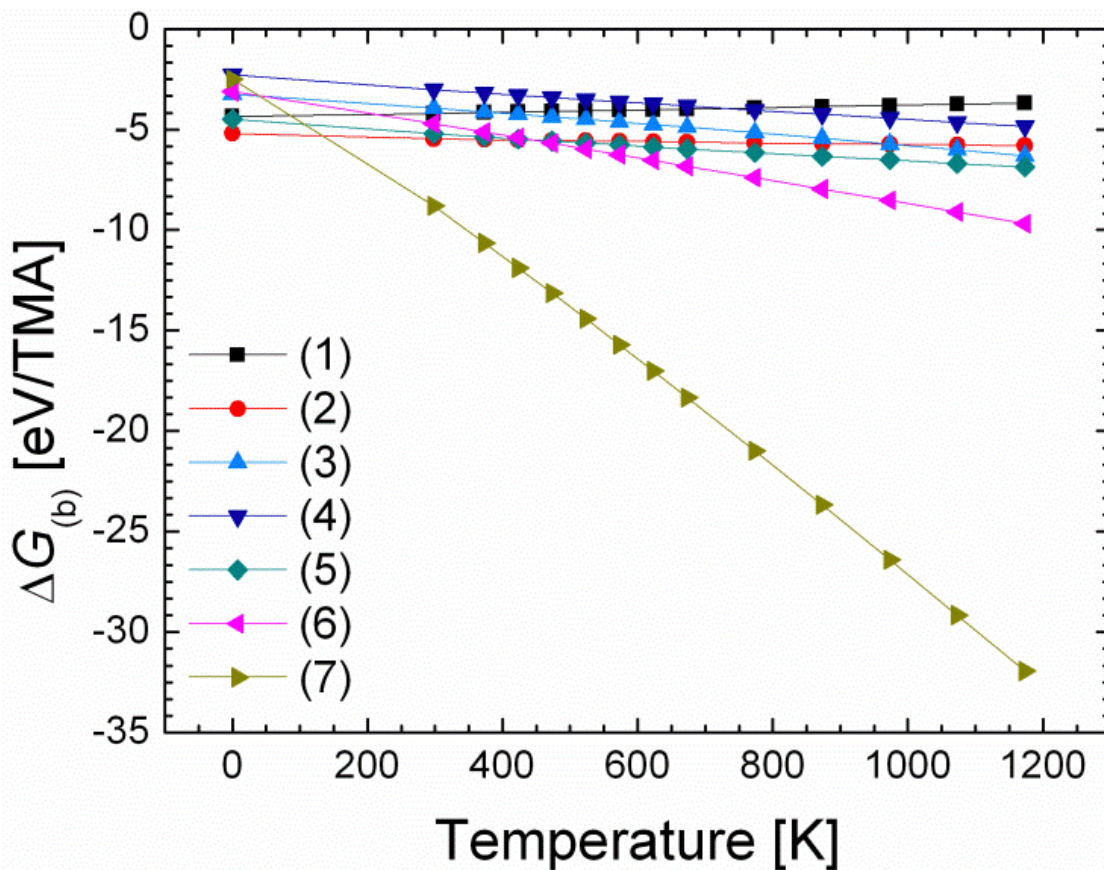


Figure 3-1. Temperature dependence of free energy for ‘clean-up’ reactions applied to bulk solids and gas-phase molecules (1)-(7).

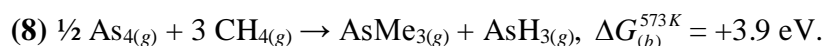
The most favorable reaction at all temperatures of interest is reaction (7). The complete oxidation process of methyl groups to carbon dioxide is strongly exothermic and requires the transfer of twenty-four electrons per TMA reacting. Four formula units of arsenic oxide are reduced to gaseous elemental arsenic in this reaction. Water is also produced giving -15.7 eV/TMA at a typical ALD process temperature.

Reactions (1)-(6) are thermodynamically competitive with one another at ALD deposition temperatures. Reactions (2), (3), (5) and (6) are thermodynamically approximately equal, releasing -5.6, -4.6, -5.8, -6.3 eV/TMA respectively at 573 K. These reactions involve reduction of arsenic (III) to elemental As in the form of gaseous  $\text{As}_4$  and oxidation of methyl groups to ethane ( $\text{C}_2\text{H}_6$ ) in reaction (2), dimethyl ether ( $\text{OMe}_2$ ) in reaction (3) or ethene ( $\text{C}_2\text{H}_4$ ), the latter with the formation of methane ( $\text{CH}_4$ ) in reaction

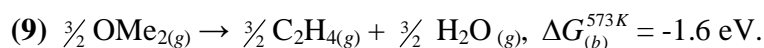
(5) or water in reaction (6). An alternative possible reaction at low temperature is non-redox ligand transfer (1), where each reacting TMA molecule produces volatile trimethylarsenic ( $\text{AsMe}_3$ ), still arsenic(III), and energy -4.0 eV and -4.4 eV at 573 K and 0 K respectively. The least possible mechanism with the change in energy -3.6 or -2.3 eV/TMA at 573 or 0 K respectively is reduction of  $\text{As}^{3+}$  to molecular arsine ( $\text{AsH}_3$ ) and oxidation of methyl groups to molecular ethene ( $\text{C}_2\text{H}_4$ ) (4).

All of these except reaction (1) involve reduction of As and oxidation of C. The number of electrons transferred is zero: reaction (1), three: (2) and (5), six: (3), (4) and (6), twenty-four: (7) per TMA reacting. In all cases,  $\text{O}^{2-}$  is transferred from arsenic to aluminium(III), presumably driven by the strength of Al – O bonding. However, note that the oxidation states of O and Al do not change.

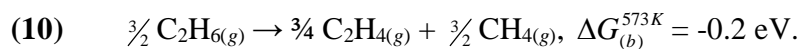
The bulk energetics can be used to investigate some side-reactions of the products. We find that disproportionation of  $\text{As}_4$  under the action of  $\text{CH}_4$  is not favored at any temperatures (Figure 3-2):



Decomposition of dimethyl ether to ethane and water is favored at all temperatures:



$\text{C}_2\text{H}_4$  and  $\text{CH}_4$  are computed to be slightly more favourable products at the ALD process temperature than  $\text{C}_2\text{H}_6$ :



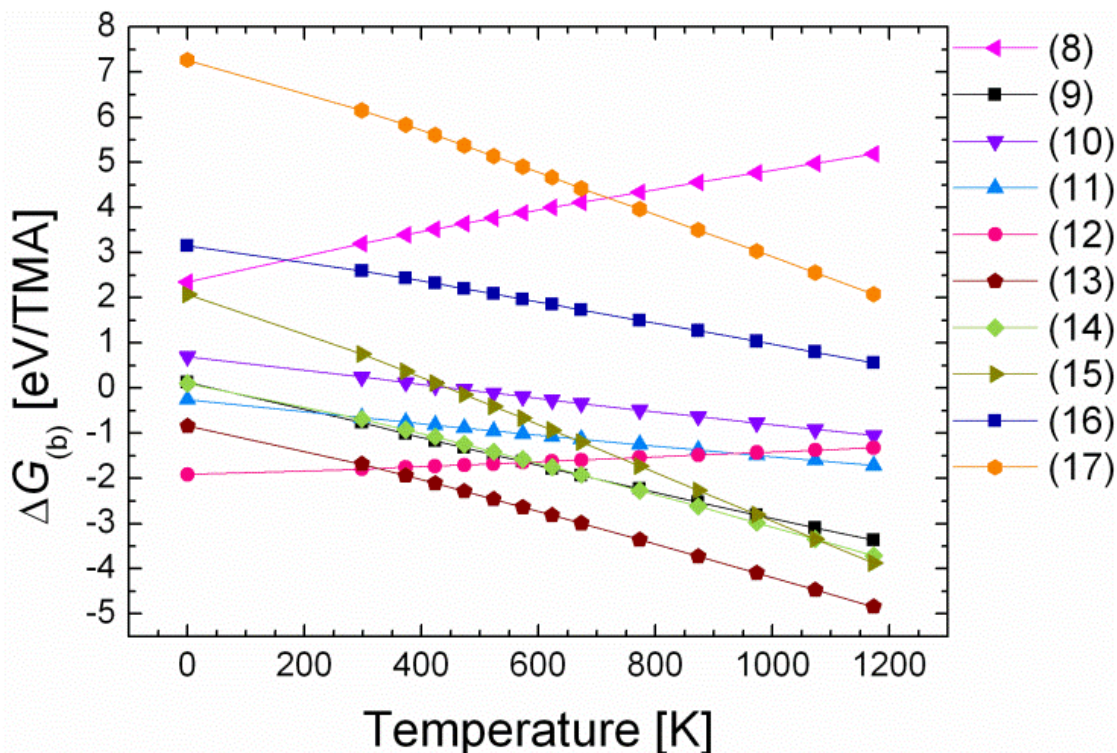


Figure 3-2. Temperature dependence of free energy for side-reactions of the gas products (8)-(12) and alternative ‘clean-up’ reactions (13)-(17).

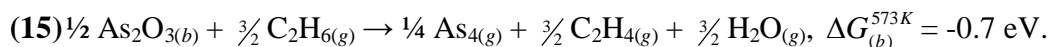
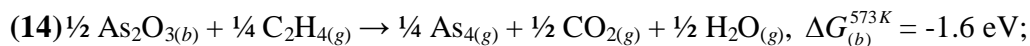
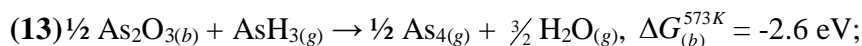
This explains why reactions (2) and (5) are thermodynamically the same, with  $C_2H_4$  and  $CH_4$  formation slightly more favourable at higher temperatures (above 500 K).

Disproportionation of  $C_2H_6$  and  $C_2H_4$  under the action of  $H_2O$  is favored:

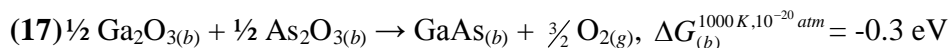
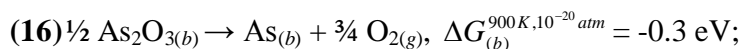


Carbon oxidation to its highest oxidation state in  $CO_2$  is a potentially exothermic reaction, depending on the source of the oxygen. Water is here a relatively weak oxidizing agent. By comparing to reaction (7), which is strongly exothermic at any temperature higher than 0 K, we see that arsenic oxide is a strong oxidizing agent.

By combining with the original ‘clean-up’ reactions, we can propose alternative surface treatments, not involving TMA, that will result in the same ‘clean-up’ effect but without the formation of  $Al_2O_3$ :



The most promising of these is probably the proposal to use AsH<sub>3</sub>. In fact, reports by Reinhardt *et al.* [106] showed that an oxidized GaAs (001) surface was deoxidized at around 350°C (625 K), certainly at 400°C under H<sub>2</sub> and AsH<sub>3</sub> constant flow. The annealing in AsH<sub>3</sub> prevents the decomposition of the GaAs and keeps it smooth during oxide desorption [107-110]. Our calculations add some extra information: this "deoxidation" may be reduction by AsH<sub>3</sub> according to (13), rather than just decomposition of As<sub>2</sub>O<sub>3</sub> into arsenic and oxygen (16). Thermal decomposition of As and Ga oxides occurs above 850 K and at very low vacuum as shown in [107-110] and computed here for reactions:



This means that thermal removal of oxides can imitate the known clean-up effect under harsh conditions, but the same can be achieved under moderate conditions *via* reduction by arsine. However, none of these is more energetically favored than the original 'clean-up' reactions at any temperature of interest (Figure 3-2).

### 3.3 Homolytic and heterolytic dissociation of TMA

We investigated the homolytic and heterolytic dissociation of TMA with high-level *ab initio* methods in order to assess the applicability of DFT methods for the considered systems. We performed computations with MP2, CASPT2, CCSD and CCSD(T). We considered three possible reactions of dissociation of a methyl group from the AlMe<sub>3</sub> monomer, namely when it dissociates as a radical (Me<sup>\*</sup>), as a methanide anion (Me<sup>-</sup>) and



as a methyl cation ( $\text{Me}^+$ ). Geometries of reactants and products were optimized with DFT PBE TZVPP using the Turbomole program. Energies were not corrected with ZPE as performing vibrational analysis with high-level *ab initio* methods is computationally too heavy. Calculated basis set superposition error (BSSE) was reduced to  $\sim 1$  kcal/mol for such large basis sets as ano-rcc and aug-cc and to a few kcal/mol for TZVPP. Obtained results are shown in [Table 3-2](#). No experimental values are available to our knowledge for these types of reactions.

Method / Basis set	Reaction energies [kcal/mol]		
	$\text{AlMe}_3 \rightarrow \text{AlMe}_2^* + \text{Me}^*$	$\text{AlMe}_3 \rightarrow \text{AlMe}_2^+ + \text{Me}^-$	$\text{AlMe}_3 \rightarrow \text{AlMe}_2^- + \text{Me}^+$
PBE / TZVPP	81.8	229.6	299.3
B3LYP / TZVPP	79.8	229.0	293.6
MP2 / ano-rcc-VTZP	87.7	235.5	299.8
MP2 / aug-cc-pVTZ	87.0	226.9	294.8
CASPT2 / ano-rcc-VTZP	87.5	235.0	296.2
CCSD / aug-cc-pVTZ	83.2	228.0	287.7
CCSD(T) / aug-cc-pVTZ	85.0	227.4	288.8

**Table 3-2 Reaction energies for the homolytic and heterolytic dissociation of Me group from  $\text{AlMe}_3$  monomer.**

$\text{Me}^*$  is a doublet in the ground state.  $\text{AlMe}_2^*$  is also a doublet, calculated to be lower in energy than the quartet by  $-81.3$  kcal/mol (PBE). The optimised geometry of  $\text{AlMe}_2^+$  in a singlet state is linear, whereas the triplet is bent. The singlet state is lower in energy by  $-61.5$  kcal/mol with respect to the triplet (PBE). For the  $\text{AlMe}_2^-$  fragment, the difference in DFT energy between singlet and triplet states is only  $19.1$  kcal/mol. Therefore, CCSD(T) single point calculations were performed on both singlet and triplet states, giving reaction energies within CCSD(T) for this heterolytic dissociation of  $288.8$  kcal/mol and  $310.0$  kcal/mol for singlet and triplet respectively.

To test the quality of the DFT calculations, we performed high-level *ab initio* computations with extensive basis sets. In the case of the homolytic dissociation, the difference between absolute energies was found to be around few kcal/mol. DFT results are very close to the one obtained with CCSD methods and MP2 performs very well. For the heterolytic dissociation we note that the choice of the basis set is crucial, which is obvious when we deal with ions. The calculations indicate that DFT methods are suitable for a good description of the regarded system. When higher accuracy is required, the use of MP2 with an appropriate basis set is sufficient.

The calculated dissociation energies suggest that the TMA molecule is moderately stable, since the binding energies are not that high. For comparison, heterolytic dissociation energies for Ru complexes, *e.g.* RuCp<sub>2</sub> (Cp = C<sub>5</sub>H<sub>5</sub><sup>-</sup>), which are very stable molecules, are found to be around 700 kcal/mol [111].

### 3.4 TMA adsorption onto As<sub>2</sub>O<sub>3</sub> surface

The oxide substrate surface is modeled by periodic slabs separated by 10 Å of vacuum. We use a 1×2 supercell that contains 1 layer totalling 4 molecular units of As<sub>4</sub>O<sub>6</sub> (40 atoms). For all slab calculations medium accuracy was used in VASP with plane wave cutoff of 396 eV and 2×1×1 *k*-point mesh.

TMA adsorbs onto oxide surfaces in an associative way, forming a Lewis adduct between Al and surface oxygen. The mechanism for this reaction is well known and has been described in previous studies on other oxides [18, 112]. For the (010) oriented arsenic oxide surface (**A**, [Figure 3-3](#)), overlap of the empty *p* orbital of Al atom in horizontal TMA with the lone pair of electrons on surface oxygen is easy and not hindered by geometry (**B**). The Al – O bond length is computed to be 2.0 Å and the calculated adsorption energy is  $\Delta E_{(surf)}^{0K} = -0.7$  eV ([Table 3-3](#)). This agrees very well with the same reaction on Al<sub>2</sub>O<sub>3</sub> [112]. The calculated Gibbs free energy,  $\Delta G_{(surf)}^{573K} = +2.5$  eV

(**B**, [Figure 3-7](#)), is positive for adsorption, as expected. The adsorbate molecule loses translational motion, which is the main contribution to the entropy (see section 2.2.3). This means that it is not thermodynamically favored for TMA to adsorb molecularly, but that subsequent TMA dissociation on the surface may lead to  $\Delta G < 0$ .

### 3.5 Methyl transfer mechanisms at surface

We have identified ligand transfer as the primary reaction of decomposition of chemisorbed  $\text{AlMe}_3$  (**B**, [Figure 3-3](#)) on arsenic (III) oxide (**A**, [Figure 3-3](#)). Successive dissociation of Me from  $\text{AlMe}_3$  leads to surface species of the type:  $(\text{||O} - )_{1+n}\text{AlMe}_{3-n} + n \text{||X} - \text{Me}$ , where  $n = 1, 2, 3$  is the number of Me groups transferred and  $\text{||X}$  is a binding site of the surface. Specifically, this dissociation can occur on surface As atoms and/or surface O atoms:  $X = \text{As}$  and/or O. On an oxidized III-V surface, one would also consider  $X = \text{In}, \text{Ga}$  *etc.*, but this is beyond the scope of the current work. Computed energetics for the formation of these products are shown in [Table 3-3](#) with the corresponding structures in [Figure 3-3](#). Entropy changes are assumed to be negligible during methyl transfer on the surface with no adsorption or desorption, *i.e.*  $\Delta G_{(surf)} = \Delta E_{(surf)}^{0K}$  at all temperatures.

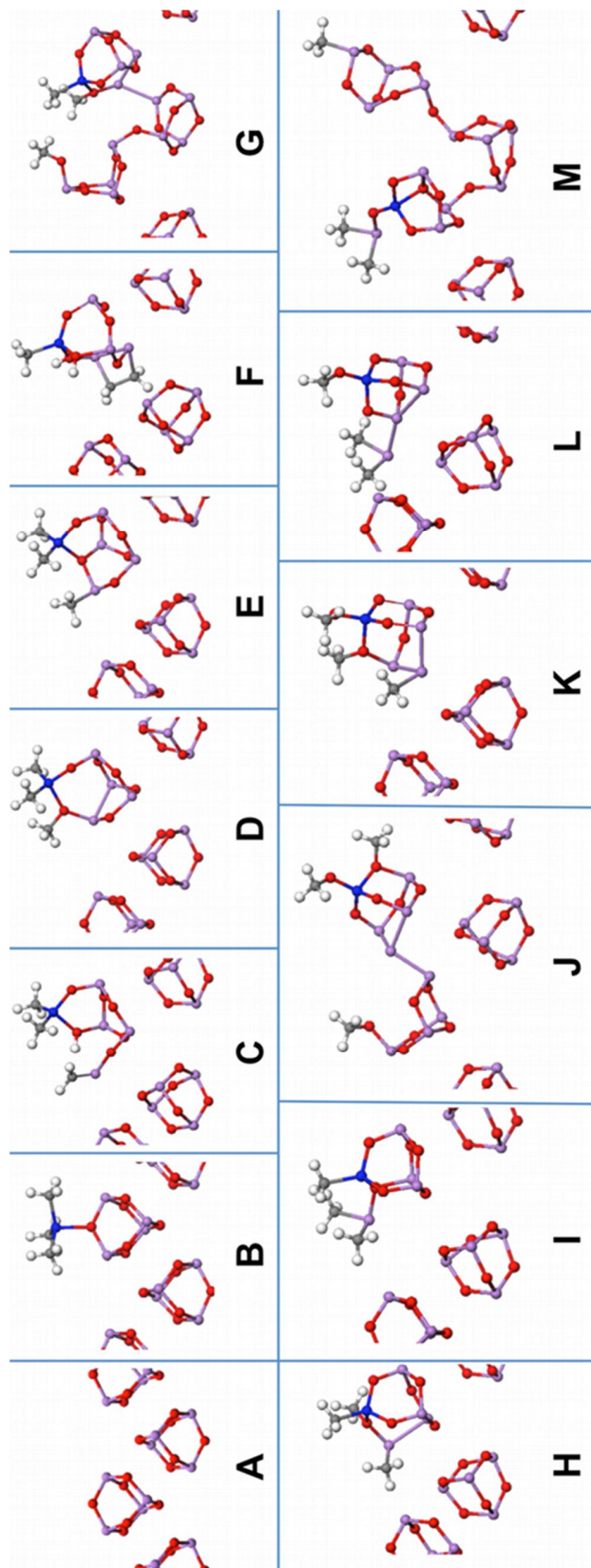


Figure 3-3. Surface models for adsorption of AlMe<sub>3</sub> onto As<sub>2</sub>O<sub>3</sub> surface (A, B) and Me group transfer (C–M) onto different atoms (surface O or surface As). Ball and stick representation: purple As, red O, blue Al, grey C and white H.

products at surface		$\Delta E_{(surf)}^{0K}$
<b>A</b>	$4 \text{As}_4\text{O}_{6(surf)} + \text{AlMe}_3(g)$	0.0
<b>B</b>	$\parallel\text{O} - \text{AlMe}_3$	-0.7
<b>C</b>	$(\parallel\text{O} - )_2\text{AlMe}_2 + \parallel\text{As} = \text{CH}_2 + \parallel\text{O} - \text{H} + 2 e^-$	+0.3
<b>D</b>	$(\parallel\text{O} - )_2\text{AlMe}_2 + \parallel\text{O} - \text{Me} + 2e^-$	-0.4
<b>E</b>	$(\parallel\text{O} - )_2\text{AlMe}_2 + \parallel\text{As} - \text{Me}$	-1.0
<b>F</b>	$(\parallel\text{O} - )_3\text{AlMe} + 2 \parallel\text{As} = \text{CH}_2 + 2 \parallel\text{O} - \text{H} + 4 e^-$	-0.3
<b>G</b>	$(\parallel\text{O} - )_3\text{AlMe} + 2 \parallel\text{O} - \text{Me} + 4e^-$	-0.4
<b>H</b>	$(\parallel\text{O} - )_3\text{AlMe} + \parallel\text{As} - \text{Me} + \parallel\text{O} - \text{Me} + 2e^-$	-1.3
<b>I</b>	$(\parallel\text{O} - )_3\text{AlMe} + 2 \parallel\text{As} - \text{Me}$	-2.5
<b>J</b>	$(\parallel\text{O} - )_4\text{Al} + 3 \parallel\text{O} - \text{Me} + 6e^-$	-1.4
<b>K</b>	$(\parallel\text{O} - )_4\text{Al} + \parallel\text{As} - \text{Me} + 2 \parallel\text{O} - \text{Me} + 4e^-$	-1.7
<b>L</b>	$(\parallel\text{O} - )_4\text{Al} + 2 \parallel\text{As} - \text{Me} + \parallel\text{O} - \text{Me} + 2e^-$	-2.4
<b>M</b>	$(\parallel\text{O} - )_4\text{Al} + 3 \parallel\text{As} - \text{Me}$	-2.9

**Table 3-3** Reaction energies ( $\Delta G_{(surf)} = \Delta E_{(surf)}$  at 0 K) for adsorption of  $\text{AlMe}_3$  onto  $\text{As}_2\text{O}_3$  surface (**A**, **B**) and Me group transfer (**C–M**) onto different surface atoms (surface O or surface As), as illustrated in Figure 3-3. Energies are in eV per  $\text{AlMe}_3$  molecule reacting with  $\text{As}_2\text{O}_3$  and relative to **A**.

According to our simulations the initial step of decomposition of  $\text{AlMe}_3$  ( $n = 1$ ) is splitting of Al – Me and binding of the methyl group to a surface arsenic atom:  $\parallel\text{As} - \text{Me}$ . Structure **E** is the lowest energy product that we found, where near-tetrahedral geometry for Al is preserved: Al is bound to two surface oxygen atoms and two remaining methyl groups:  $(\parallel\text{O} - )_2\text{AlMe}_2$ . The energy change for this reaction is computed to be -1.0 eV relative to **A** and -0.3 eV relative to **B** (Table 3-3). Therefore, we can propose a mechanism as follows:



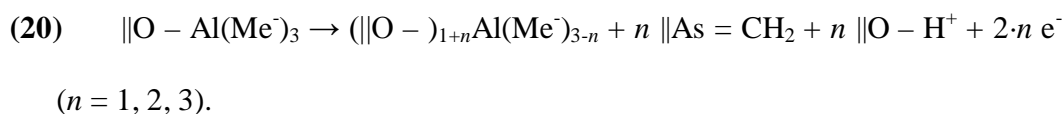
The other possibility of dissociation of  $\text{AlMe}_3$  in this step is the one where the Me group binds to O ( $\parallel\text{O} - \text{Me}$ , **D**), which is computed to be slightly unfavourable ( $\Delta E_{(surf)}^{0K} = 0.3$  eV relative to **B**). Transferring Me to O is expected to be accompanied by the transfer of electrons. The  $\text{Me}^-$  group on Al becomes oxidized to  $\text{Me}^+$  on O, releasing two electrons. The general reaction for this mechanism can be written as:



The optimized structure (**D**) shows an As – As bond, suggesting that the electrons are transferred from carbon to arsenic (see section 3.6).

Proton diffusion according to the reaction:  $\text{||As} - \text{Me} \rightarrow \text{||As} = \text{CH}_2 + \text{H}^+ + 2\text{e}^-$  is a further decomposition reaction that can contribute to the mechanism for reactions (**4**)-(6).

The computed energy ( $\Delta E_{(surf)}^{0K} = 0.3 \text{ eV}$ ) suggests that there may be a high barrier for this reaction. The optimized structure is shown in [Figure 3-3](#) labelled as **C**. On the other hand, further proton diffusion seems to be favorable, as in reaction **F**:  $2 \text{||As} - \text{Me} \rightarrow 2 \text{||As} = \text{CH}_2 + 2 \text{H}^+ + 4\text{e}^-$  with  $\Delta E_{(surf)}^{0K} = -0.3 \text{ eV}$  relative to **A**. The relaxed structure **F** shows that once two methylene groups ( $=\text{CH}_2$ ) are formed, a C – C bond appears, but As – C is strong enough to keep it from desorption as  $\text{C}_2\text{H}_4$  ([Figure 3-3](#)). In general we can write the reaction:



The second methyl group transfer ( $n = 2$ ) gives a product of the type  $(\text{||O}^-)_3\text{AlMe}$ , with the transferred group on O again ( $2 \text{||O} - \text{Me}$ , **G**), on both ( $\text{||As} - \text{Me} + \text{||O} - \text{Me}$ , **H**), or on As again ( $\text{||As} - \text{Me}_2$ , **I**). We found that the formation of  $\text{||As} - \text{Me}_2$  (**I**) is the most energetically favourable, with a change in energy of -2.5 eV relative to **A**. Transferring a second Me to As is of the same type as described above for **E**, since Al and As are in the same formal oxidation state (+3). Formation of  $\text{||As} - \text{Me} + \text{||O} - \text{Me}$  (**H**) gives only -1.3 eV (see [Table 3-3](#)) and requires oxidation of one Me group, similar to **D**. The least plausible is oxidation of two Me groups in **G** with a change in energy of only -0.4 eV relative to **A**, isoenergetic with **D**. It is therefore likely that the **D** → **G** redox reaction is reversible. For all structures (**F**, **G**, **H**, **I**) Al is roughly tetrahedral, coordinated to three O sites and the last remaining Me group.

We find that dissociation of the final Me ( $n = 3$ ) from Al leads to products of the type  $(\text{||O} - )_4\text{Al} + 3 \text{||X} - \text{Me}$  with four O atoms bound to *surf*-Al. There are four possibilities for this reaction: all three Me on O atoms ( $3 \text{||O} - \text{Me}$ ), one Me on As and two Me on O atoms ( $\text{||As} - \text{Me} + 2 \text{||O} - \text{Me}$ ), two Me on As atoms and one on O ( $2 \text{||As} - \text{Me} + \text{||As} - \text{O}$ ), or all three Me on As atoms ( $3 \text{||As} - \text{Me}$ ). Structures **J**, **K**, **L** and **M** respectively are the lowest energy structures that we have found for this dissociation (**Figure 3-3**). Again the energetically most probable scenario is dissociation of TMA onto arsenic atoms. This liberates  $\Delta E_{(surf)}^{0K} = -2.9$  eV (**M**, **Table 3-3**). Relative to this, transfer of successive Me to O costs energy: **L** has  $\Delta E_{(surf)}^{0K} = -2.4$  eV, **K** has  $\Delta E_{(surf)}^{0K} = -1.7$  eV and **J** has  $\Delta E_{(surf)}^{0K} = -1.4$  eV. The redox reaction **I**  $\rightarrow$  **L** is thus energetically nearly neutral and probably reversible. Oxidation of three methyl groups partially reduces four As atoms and three covalent As – As bonds appear in the relaxed structure **J**.

In **Figure 3-4** we show possible connections between computed minima.

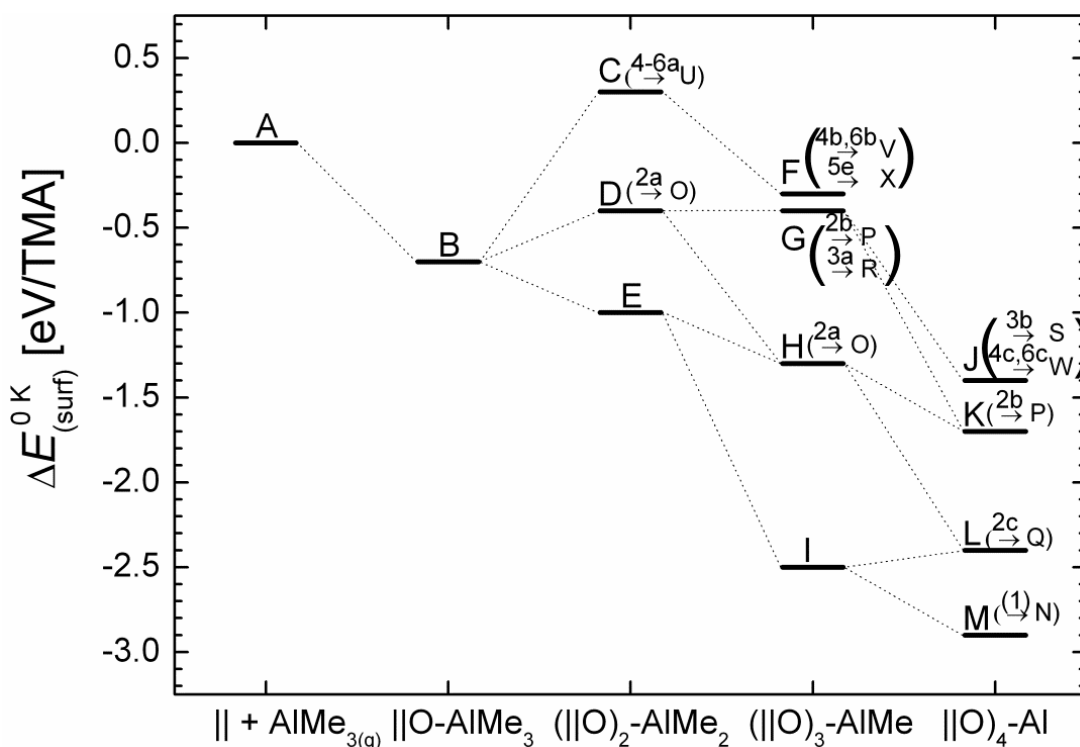


Figure 3-4. Potential energy surface ( $\Delta G_{(surf)} = \Delta E_{(surf)}$  at 0 K) showing the minima for structures A–M in the methyl transfer steps that form part of surface reactions (1)–(6) (Table 3-5) and give surface products N–Z Figure 3-6 as typed in brackets. The corresponding numerical values (in eV per  $\text{AlMe}_3$  molecule reacting with  $\text{As}_2\text{O}_3$  at 0 K) are shown in Table 3-3 with surface models shown in Figure 3-3.

Our computations thus reveal the overall trends in energetics of TMA decomposition onto arsenic or oxygen atoms. The energy liberated by breaking an Al – Me bond and forming As – Me ranges from -0.3 to -1.5 eV. On the other hand, forming an O – Me bond is less energetically favored, ranging from -0.2 to +0.3 eV, even if an As – Me bond is already present. What is more, oxidising a Me group is strongly uphill when Me transfer occurs from As to O (ranges from 0 to +1.2 eV). This suggests that the As – C bond is strong. Bader population of the As – Me bond has shown no significant change in charges on atoms relative to Al – Me, suggesting that the formal oxidation state  $\text{Me}^-$  is preserved (see Table 3-4).



### 3.6 Population analysis of reduced structures

**Table 3-4** shows the resulting differences in valence charges associated with selected atoms from structures **B**, **D** and **E**. It is shown that during Me transfer onto As there is negligible reorganization in the electronic populations (see  $\Delta q$  (**B**  $\rightarrow$  **E**) **Table 3-4**), which means that no charge transfer occurred. As mentioned before, transferring Me to O is expected to cause the transfer of electrons since, formally, oxidising the  $\text{Me}^-$  group to  $\text{Me}^+$  releases two electrons. This is confirmed in the difference between valence atomic charges of the carbon atom denoted  $\text{C}^1$  (see **Figure 3-5** for labels) that is bound with O or As in structures **D** or **E** respectively. This  $\Delta q(\mathbf{E} \rightarrow \mathbf{D})$  for  $\text{C}^1$  is determined to be  $-1.7e$ . Released electrons are accepted by As atoms, which is manifested in formation of the  $\text{As}^1 - \text{As}^2$  bond in structure **D** ( $R(\text{As}^1 - \text{As}^2) = 2.619 \text{ \AA}$ ).  $\Delta q$  increases from  $0.0e$  for ‘surface’ arsenic As (formal oxidation state +3) to  $1.1e$  and  $1.0e$  for  $\text{As}^1$  and  $\text{As}^2$  respectively, so that the electron pair is shared in the newly-formed  $\text{As}_2$  dimer and formal oxidation state of these arsenic atoms would be +2.

atom	$\Delta q$ ( <b>B</b> $\rightarrow$ <b>E</b> )	$\Delta q$ ( <b>E</b> $\rightarrow$ <b>D</b> )
As	0.0	0.0
$\text{As}^1$	0.1	1.1
$\text{As}^2$	0.0	1.0
C	0.1	0.1
$\text{C}^1$	0.2	-1.7

**Table 3-4.** Differences in Bader atomic charges ( $\Delta q$ ) between selected atoms from structures **B**, **D** and **E** (**Figure 3-3**). Selected atoms are labeled on structures **D** and **E** (**Figure 3-5**).

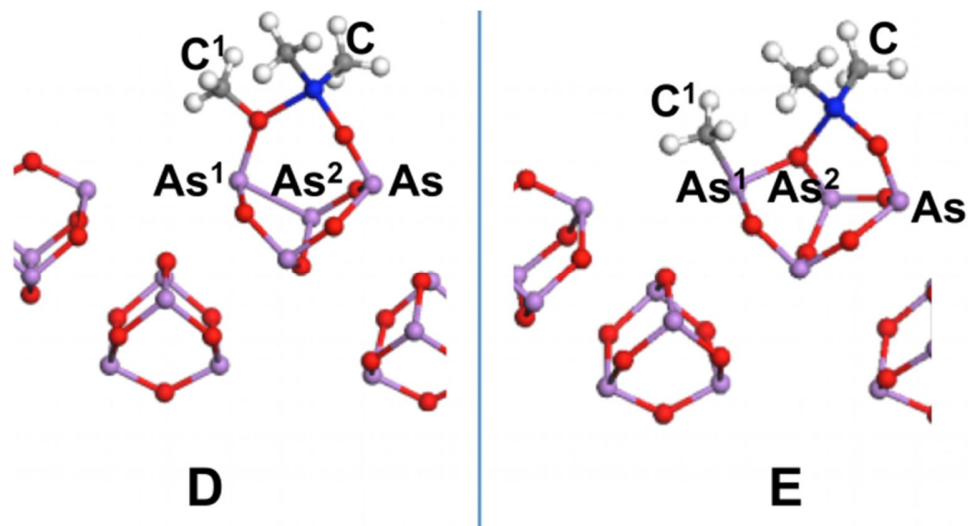


Figure 3-5. Structures D and E with atoms labeled for the Bader charge analysis in Table 3-4.

### 3.7 Production of various volatile species

As stated in section 3.5, decomposition of trimethylaluminum on arsenic oxide may lead to formation of multiple products on the surface. This may result in desorption of nine volatile species:  $\text{As}_4$ ,  $\text{AsMe}_3$ ,  $\text{AsH}_3$ ,  $\text{CH}_4$ ,  $\text{C}_2\text{H}_4$ ,  $\text{C}_2\text{H}_6$ ,  $\text{CO}_2$ ,  $\text{H}_2\text{O}$  and  $\text{OMe}_2$  according to reactions (1)-(7). We have computed the temperature dependence of Gibbs free energies for these reactions at the surface ( $\Delta G_{(surf)}$ ) which is shown in Figure 3-8. A schematic of the potential free energy surface at a typical ALD temperature is shown in Figure 3-7 with values in Table 3-5 and structures of products in Figure 3-6.

surface reaction				$\Delta G_{(surf)}^{573K}$
		surface product	gaseous product	
<b>(1)</b>	<b>N</b>	$(\text{  O}-)_4\text{Al}$	+ AsMe <sub>3</sub>	-2.4
<b>2a</b>	<b>O</b>	$(\text{  O}-)_3\text{AlMe} + 2 e^-$	+ C <sub>2</sub> H <sub>6</sub>	-0.7
<b>2b</b>	<b>P</b>	$(\text{  O}-)_4\text{Al} + \text{  O}-\text{Me} + 4 e^-$	+ C <sub>2</sub> H <sub>6</sub>	-0.9
<b>2c</b>	<b>Q</b>	$(\text{  O}-)_4\text{Al} + \text{  As}-\text{Me} + 2 e^-$	+ C <sub>2</sub> H <sub>6</sub>	-1.6
<b>(2)</b>	<b>N</b>	$(\text{  O}-)_4\text{Al}$	+ $\frac{1}{4}$ As <sub>4</sub> + $\frac{3}{2}$ C <sub>2</sub> H <sub>6</sub>	-4.0
<b>3a</b>	<b>R</b>	$(\text{  O}-)_3\text{AlMe} + 4 e^-$	+ OMe <sub>2</sub>	+0.5
<b>3b</b>	<b>S</b>	$(\text{  O}-)_4\text{Al} + \text{  O}-\text{Me} + 6 e^-$	+ OMe <sub>2</sub>	-0.5
<b>3c</b>	<b>T</b>	$(\text{  O}-)_4\text{Al} + \text{  O}-\text{Me}$	+ $\frac{1}{2}$ As <sub>4</sub> + OMe <sub>2</sub>	-1.3
<b>4-6a</b>	<b>U</b>	$(\text{  O}-)_2\text{AlMe}_2 + \text{  O}-\text{H} + 2 e^-$	+ $\frac{1}{2}$ C <sub>2</sub> H <sub>4</sub>	+1.8
<b>4b, 6b</b>	<b>V</b>	$(\text{  O}-)_3\text{AlMe} + 2 \text{  O}-\text{H} + 4 e^-$	+ C <sub>2</sub> H <sub>4</sub>	+1.0
<b>4c, 6c</b>	<b>W</b>	$(\text{  O}-)_4\text{Al} + 3 \text{  O}-\text{H} + 6 e^-$	+ $\frac{3}{2}$ C <sub>2</sub> H <sub>4</sub>	-1.1
<b>(4)</b>	<b>N</b>	$(\text{  O}-)_4\text{Al}$	+ AsH <sub>3</sub> + $\frac{3}{2}$ C <sub>2</sub> H <sub>4</sub>	-2.0
<b>5b</b>	<b>O</b>	$(\text{  O}-)_3\text{AlMe} + 2 e^-$	+ $\frac{1}{2}$ C <sub>2</sub> H <sub>4</sub> + CH <sub>4</sub>	-0.8
<b>5c</b>	<b>P</b>	$(\text{  O}-)_4\text{Al} + \text{  O}-\text{Me} + 4 e^-$	+ $\frac{1}{2}$ C <sub>2</sub> H <sub>4</sub> + CH <sub>4</sub>	-1.0
<b>5d</b>	<b>Q</b>	$(\text{  O}-)_4\text{Al} + \text{  As}-\text{Me} + 2 e^-$	+ $\frac{1}{2}$ C <sub>2</sub> H <sub>4</sub> + CH <sub>4</sub>	-1.8
<b>5e</b>	<b>X</b>	$(\text{  O}-)_4\text{Al} + \text{  O}-\text{H} + 4 e^-$	+ C <sub>2</sub> H <sub>4</sub> + CH <sub>4</sub>	-2.2
<b>(5)</b>	<b>N</b>	$(\text{  O}-)_4\text{Al}$	+ $\frac{1}{4}$ As <sub>4</sub> + $\frac{3}{4}$ C <sub>2</sub> H <sub>4</sub> + $\frac{3}{2}$ CH <sub>4</sub>	-4.2
<b>6d</b>	<b>R</b>	$(\text{  O}-)_3\text{AlMe} + 4 e^-$	+ C <sub>2</sub> H <sub>4</sub> + H <sub>2</sub> O	-0.6
<b>6e</b>	<b>Y</b>	$(\text{  O}-)_4\text{Al} + \text{  O}-\text{H} + 6 e^-$	+ $\frac{3}{2}$ C <sub>2</sub> H <sub>4</sub> + H <sub>2</sub> O	-2.3
<b>6f</b>	<b>Z</b>	$(\text{  O}-)_4\text{Al}$	+ $\frac{1}{2}$ As <sub>4</sub> + $\frac{3}{2}$ C <sub>2</sub> H <sub>4</sub> + H <sub>2</sub> O	-3.1

Table 3-5. Reaction Gibbs free energies at 573 K for production of volatile species according to reactions (1)-(6) and their intermediates reactions 2a-6f. Models of surfaces after desorption N-Z are illustrated in Figure 3-6. Given values are in eV per AlMe<sub>3</sub> molecule reacting with As<sub>2</sub>O<sub>3</sub> and relative to A.

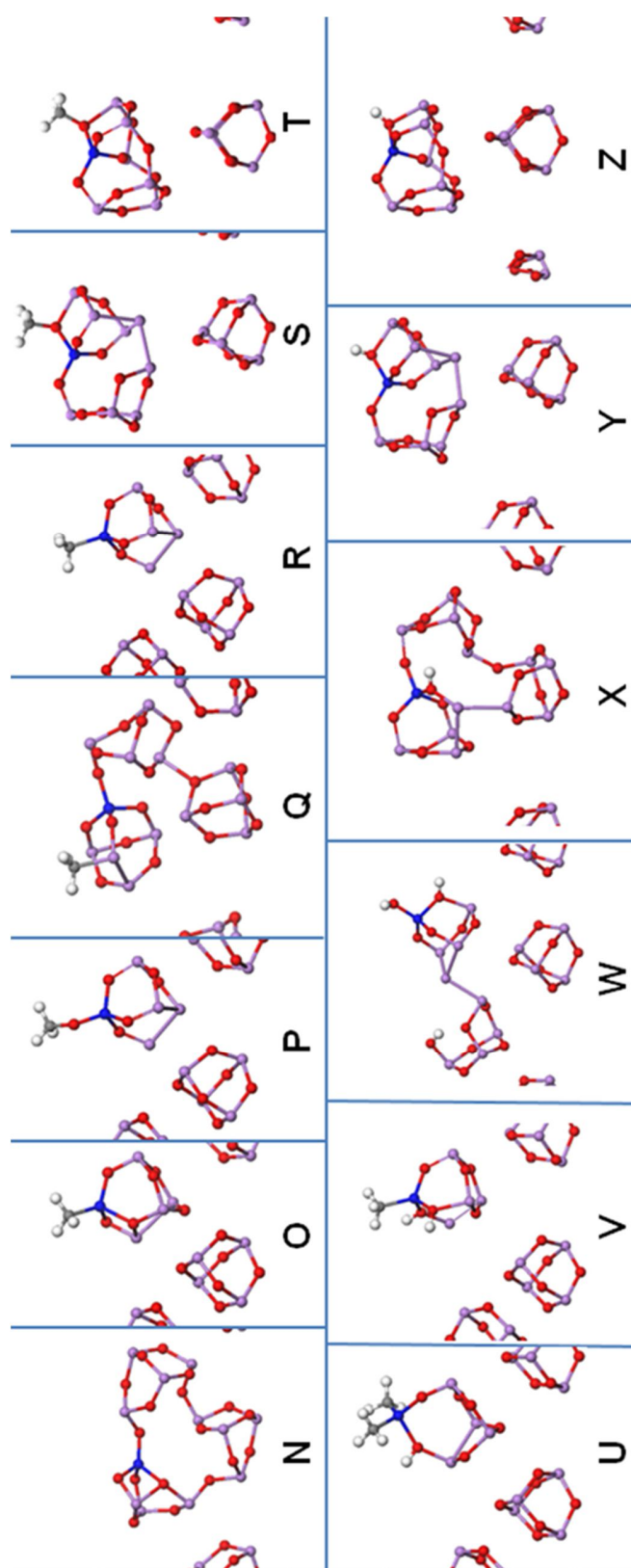
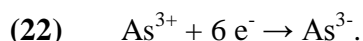
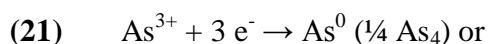


Figure 3-6. Surface models of products of desorption of volatile species:  $\text{As}_4$ ,  $\text{AsMe}_3$ ,  $\text{AsH}_3$ ,  $\text{CH}_4$ ,  $\text{C}_2\text{H}_4$ ,  $\text{C}_2\text{H}_6$ ,  $\text{H}_2\text{O}$  and  $\text{OMe}_2$  according to reactions (1)-(6) and their intermediates 2a-6f. Ball and stick representation: purple As, red O, blue Al, grey C and white H.

If there is sufficient concentration of  $\parallel\text{As} - \text{Me}$  groups on the surface (**M**, [Figure 3-3](#)), trimethylarsine may be formed from  $\text{As}^{3+}$  without any redox *via* reaction **(1)** to give product **N**, [Figure 3-6](#). This process is exothermic:  $\Delta G_{(surf)}^{573K} = -2.4$  eV per TMA (see [Table 3-5](#) for energetics of surface reactions), but desorption of  $\text{AsMe}_3$  is less favored than formation of surface products  $\parallel\text{As} - \text{Me}_n$ . The computed energies for reaction **(1)** are also much smaller compared to redox surface reactions **(2)**, **(5)** and **(6)**. As noted above, the energetics of ligand transfer on the surface favour Me transfer from Al to As. However, transfer to O, concomitant with partial reduction of surface As, will close off the possibility of desorption as  $\text{As}^{3+}$  in reaction **(1)**. In this way, we see that each surface reaction affects the surface concentration of reactants for the other reactions.

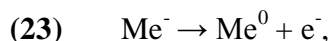
As shown in previous sections, each decomposition of TMA on surface oxygen atoms causes a transfer of electrons and reduction of surface arsenic. Arsenic (III) oxide can be reduced to elemental arsenic or even to molecular arsine (formal 3- oxidation state) as shown in redox reactions **(2)**-**(7)**. This requires transferring three or six electrons per arsenic atom accordingly:



This shows that decomposition of multiple TMAs may lead gradually to the accumulation of charge on surface As and eventual desorption as  $\text{AsH}_3$  or  $\text{As}_4$ , which is a possible volatile form of elemental As. Alternatively, reduced As may undergo other reactions (see section 3.8). The mechanism identified here of transferring electrons by Me transfer to surface O can produce up to six electrons per one TMA molecule (see reaction **(19)** – transfer of three methyl groups to O gives six electrons). This approach allows us to evaluate surface energetics for production of an  $\text{AsH}_3$  molecule or up to half of an  $\text{As}_4$  molecule in reactions **(2)**-**(6)**, which will be described below, but it does not allow us to

evaluate the surface energy of reaction (7), where twenty-four electrons are transferred to produce two As<sub>4</sub> molecules. Modelling reaction (7) requires further consideration of proton diffusion, which was shown to be endothermic (C), and is beyond the scope of this work. Nevertheless bulk energetics (section 3.2) showed this reaction to be the most exothermic ‘clean-up’ reaction, where eight arsenics are reduced by one TMA and carbon is completely oxidized (from formally -4 in Me up to +4 in CO<sub>2</sub>). One can only speculate that this kind of charge transfer is subject to kinetics, as will be discussed in the next section.

Our simulations show that formation of C<sub>2</sub>H<sub>6</sub> in reaction (2) is spontaneous when Me groups in the right oxidation state,  $\parallel M - Me^-$  ( $M = Al, As$ ) and  $\parallel O - Me^+$ , are close together. It can occur for most of the surface dissociation products studied in section 3.5 (when at least one Me group is oxidized: **D, G, H, K, L, Figure 3-3**) and so this is a statistically likely reaction. Desorption of the C<sub>2</sub>H<sub>6</sub> molecule can lead to three types of products *via* reaction **2a, 2b, 2c**: when the remaining Me group binds to Al, to O or to As respectively, and the lowest energy structures that we have found are **O, P, Q** respectively (see **Figure 3-6**). Again the most energetically favorable is a structure of the type  $\parallel As - Me$  with calculated energy for reaction **2c**:  $\Delta G_{(surf)}^{573K} = -1.6$  eV relative to **A** (see **Table 3-5**). In reaction (2) one surface arsenic atom is reduced to elemental arsenic. This requires transferring three electrons (reaction (21)). Therefore, from the product of reaction **2c** we remove the remaining methyl group as Me<sup>0</sup> ( $\frac{1}{2}$  C<sub>2</sub>H<sub>6</sub>):



thereby transferring one more electron to already-reduced As *via* (19) in structure **Q**, transferring three electrons overall. Eliminating As<sup>0</sup> *via* (21) from the surface (*i.e.*  $\frac{1}{4}$  As<sub>4(g)</sub>) and relaxing gives the final product **N** (**Figure 3-6**) along with an estimate of the

energetics of surface reaction (2) (Table 3-5). The change in free energy computed according to the stoichiometry of reaction (2) is -4.0 eV per TMA.

OMe<sub>2</sub> may be formed from surface dissociation products: **G**, **J**, **K**, where at least two methyl groups are oxidized. Desorption of OMe<sub>2</sub> according to reaction 3a gives product **R** (Figure 3-6) and is endothermic  $\Delta G_{(surf)}^{573K} = +0.5$  eV relative to **A** (see Table 3-5). To estimate the energy for reaction (3), in accord with stoichiometry, it is necessary to oxidize three methyl groups *via* (19) so two arsenics ( $\frac{1}{2}$  As<sub>4</sub>) are reduced *via* (21). This procedure results in product **S**, with three As – As dimers, and a change in energy  $\Delta G_{(surf)}^{573K} = -0.5$  eV relative to **A**. Desorption of OMe<sub>2</sub> and  $\frac{1}{2}$  As<sub>4</sub> leaves the surface product **T** and we can estimate the energy for reaction 3c:  $\Delta G_{(surf)}^{573K} = -1.3$  eV. Surface energetics for the entire reaction (3) could not be calculated, since it produces fractional numbers of O atoms per TMA ( $\frac{3}{2}$  OMe<sub>2</sub>).

Production of ethene in reactions (4) is shown to be strongly uphill. As mentioned before, there is probably a high barrier for the proton diffusion mechanism. The free energy computed for desorption of  $\frac{1}{2}$  C<sub>2</sub>H<sub>4</sub> from structure **C** (Figure 3-3) *via* reaction 4a to form product **U** is  $\Delta G_{(surf)}^{573K} = +1.8$  eV (see Table 3-5, Figure 3-6). For surface reactions 4b the energy cost is a little less,  $\Delta G_{(surf)}^{573K} = +1.0$  eV, where C<sub>2</sub>H<sub>4</sub> is formed from surface product shown in **F** (Figure 3-3) and leaves surface product **V** (Figure 3-6). Finally desorption of  $\frac{3}{2}$  C<sub>2</sub>H<sub>4</sub> from structure **J** is exothermic in 4c surface reaction (Table 3-5). As a result of desorption of  $\frac{3}{2}$  ethene, a hydroxylated arsenic oxide surface is produced: ||O – H, six electrons are transferred to surface arsenic (20) and as a consequence three As – As dimers are formed (**W**, Figure 3-6). (On an oxidized GaAs surface, ||Ga – OH may also form, but this is beyond our current scope.) In the next reaction, desorption of three protons (H<sup>+</sup>) from the hydroxyl groups and one reduced arsenic *via* (22) gives the final

gaseous product  $\text{AsH}_3$  and surface product denoted as **W** (Figure 3-6). The Gibbs free energy for the entire reaction (4) modeled on the surface is  $\Delta G_{(surf)}^{573K} = -2.0$  eV (Table 3-5), making it the least favorable of the ‘clean-up’ reactions that we have computed (Figure 3-7).

Reaction (5) is subdivided according to products: **5a** – formation of  $\frac{1}{2}$   $\text{C}_2\text{H}_4$  (which is the same as **4a** described above), **5b-d** – formation of  $\text{CH}_4$  and arsenic reduction according to (5). Structure **C** is the substrate for reactions **5b**, **5c** and **5d**, resulting in surfaces **N**, **O** and **P** respectively (Figure 3-6). In addition, elimination of  $\text{C}_2\text{H}_4$  and  $\text{CH}_4$  according to reaction **5e** (Table 3-5) from structure **F** (Figure 3-3) leaves a partially hydroxylated surface for which the lowest energy structure that we have found is **T** (Figure 3-6). The fractional numbers of product molecules per TMA in reaction (5) seem to present a problem in calculating product desorption explicitly. However, eliminating fragments with the correct oxidation state results in proper stoichiometry. Thus, atoms are removed from the surface **Q** ( $\text{||As} - \text{Me} + 2\text{e}^-$ ) as  $\text{As}^0 + \text{CH}_3^0$  ( $\text{||As} + \text{Me}^0 + 3\text{e}^-$ ), where  $\text{CH}_3^0$  has C in the same overall oxidation state as the products  $\frac{1}{4}$   $\text{C}_2\text{H}_4 + \frac{1}{2}$   $\text{CH}_4$ . This procedure yields a surface free energy for the entire reaction (5):  $\Delta G_{(surf)}^{573K} = -4.2$  eV (Table 3-5). These surface energetics (Figure 3-7) confirm the bulk energetics already estimated in section 3.2 for the formation of  $\text{C}_2\text{H}_6$  or  $\text{C}_2\text{H}_4$  and  $\text{CH}_4$  as a result of the ‘clean-up’ effect.



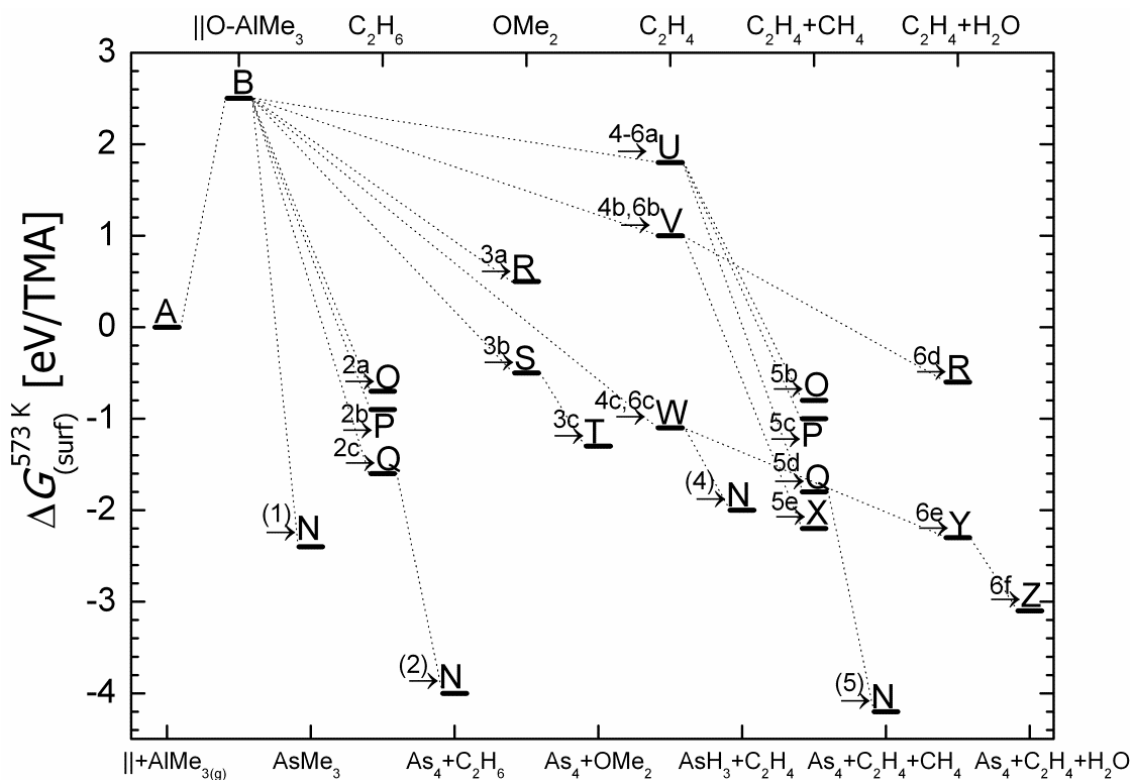


Figure 3-7. Potential free energy surface showing minima for adsorption (B) and when volatile species are produced for surface reactions (1)-(6) and 2a-6f. The corresponding numerical values (in eV per AlMe<sub>3</sub> molecule reacting with As<sub>2</sub>O<sub>3</sub> at 573 K) are shown in Table 3-5 with surface models shown in Figure 3-3 (A, B) and Figure 3-6 (N-Z). Bottom and top x axes emphasize surface or gaseous products.

Formation of C<sub>2</sub>H<sub>4</sub> in reactions **6a-c** (which are the same as **4a-c** described above) are intermediates for reaction (6). Dehydration of the surface model V according to: 2 ||O – H → || – O – || + H<sub>2</sub>O<sub>(g)</sub>, reaction **6d**, will give the surface product R, Figure 3-6, and  $\Delta G_{(surf)}^{573K} = -0.6$  eV (Table 3-5). Dehydration of the surface model W according to reaction **6e** is predicted to be thermodynamically more favored with  $\Delta G_{(surf)}^{573K} = -2.3$  eV (V, Figure 3-6 and Figure 3-7). The surface energy for the entire reaction (6) also could not be calculated for the same reason as for reaction (3) – the fractional number of O atoms in the final product ( $\frac{3}{2}$  H<sub>2</sub>O). Nevertheless, the partial data (reaction **6f**, Table 3-5, surface product Z, Figure 3-6) place this process in the same energetic range as other redox mechanisms within this simple model and confirm our bulk estimate of the competition between reactions (2), (5) and (6) (Figure 3-7).

We have also computed adsorption of a second TMA molecule onto the hydroxylated surface **W**. The computed energies are the same as for the first TMA molecule adsorption ( $\Delta G_{(surf)}^{573K} / \Delta E_{(surf)}^{0K} = +2.5/-0.7$  eV, relative to **W**). This process can be also accompanied by CH<sub>4</sub> formation. In this reaction a proton may be transferred from one of the ||O – H groups to the C of the newly adsorbed AlMe<sub>3</sub> molecule, producing CH<sub>4</sub>, which desorbs: ||O – H + ||O – AlMe<sub>3</sub> → (||O)<sub>2</sub> – AlMe<sub>2</sub> + CH<sub>4(g)</sub>. This releases  $\Delta E_{(surf)}^{0K} = -1.4$  eV relative to **W** but thermodynamically it is neutral:  $\Delta G_{(surf)}^{573K} = 0.1$  eV. This is close to the value computed by Elliott and Greer for the same reaction on an aluminum oxide substrate ( $\Delta E_{(surf)}^{0K} = -1.2$  eV) [112]. In addition, we find that dehydration of the surface model **V**, according to reaction **6d**, is less favored than methane production in reaction **5e**. More importantly, dehydration of the surface model **W** according to reaction **6e** is predicted to be thermodynamically more favored than AsH<sub>3</sub> desorption. In all of these cases, surface protons are consumed *via* ||OH, ||Me and/or incoming TMA to form CH<sub>4</sub> or H<sub>2</sub>O. This suggests that reaction **(4)** is not only limited by electron transfer and accumulation, but also by proton concentration on the oxide surface and this is governed by kinetics.

**Figure 3-8** illustrates the effect of temperature on the candidate ‘clean-up’ reactions in terms of the energy gained when products desorb. (The statistical likelihood and inter-competition between reactions is not shown, but is discussed in section 3.8). Intermediates **4a-c** leading to AsH<sub>3</sub> *via* reaction **(4)** are high in energy (also visible in **Figure 3-7**) and become progressively less favored with increasing temperature. Production of As<sub>4</sub> is consistently lower in energy (products **N** of reactions **(2)** and **(5)**, and **Z** of reaction **6f** also in **Figure 3-7**). Formation of OMe<sub>2</sub> along with As<sub>4</sub> is less favored than formation of other co-products of As<sub>4</sub>. At temperatures up to about 150°C (423 K), the most energetically favored co-product with As<sub>4</sub> is C<sub>2</sub>H<sub>6</sub> **(2)**, followed by C<sub>2</sub>H<sub>4</sub> and CH<sub>4</sub>

(5).  $\text{As}_4 + \text{C}_2\text{H}_4$  and  $\text{As}_4 + \text{CH}_4$  dominate in the range  $250^\circ\text{C} - 700^\circ\text{C}$  ( $523\text{ K} - 973\text{ K}$ ). At much higher temperatures ( $>800^\circ\text{C}$ ),  $\text{As}_4 + \text{C}_2\text{H}_4 + \text{H}_2\text{O}$  are the favored products (6f).

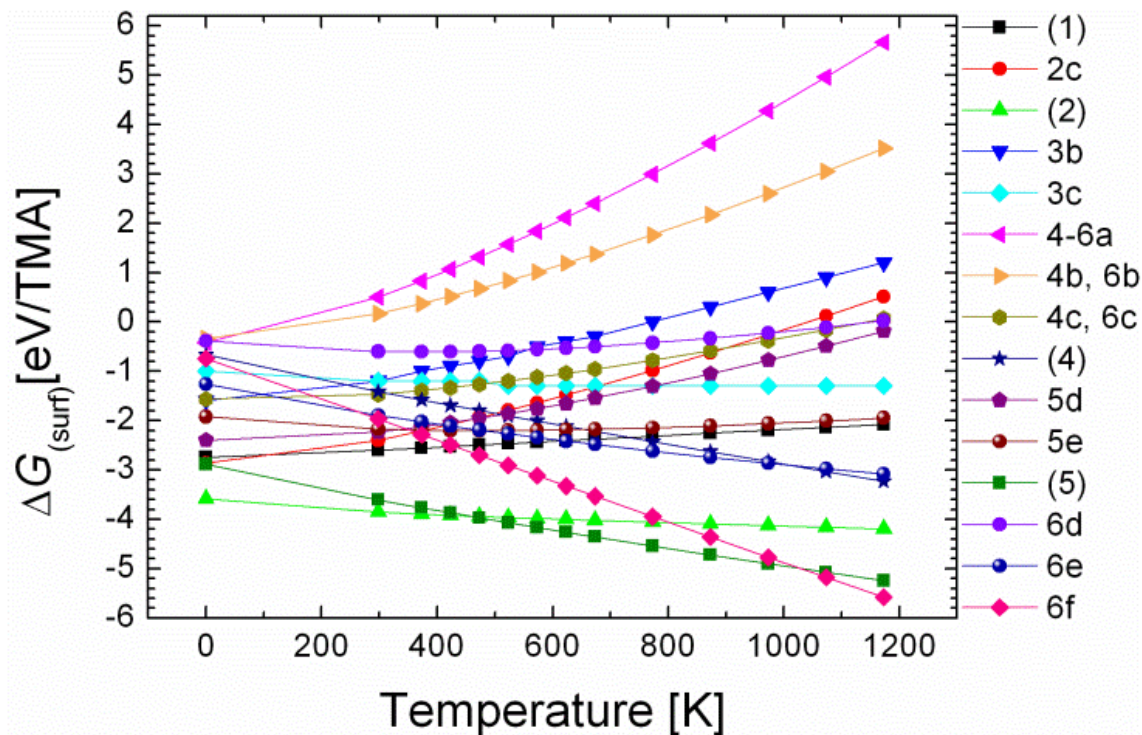


Figure 3-8. Temperature dependence of surface free energy for ‘clean-up’ reactions (1)-(6) and their intermediates 2a-6f.

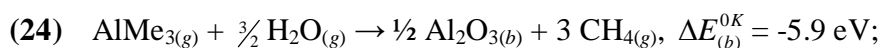
### 3.8 Discussion

We have computed different mechanisms of decomposition of TMA on arsenic (III) oxide that can be responsible for the ‘clean-up’ effect: methyl transfer, proton diffusion, methyl oxidation and arsenic reduction. The possible surface intermediates are  $\text{Al} - \text{Me}_n$ ,  $\text{As} - \text{Me}_n$ ,  $\text{O} - \text{Me}$ ,  $\text{As} - \text{As}$  and  $\text{Al} - \text{OH} - \text{As}$ . As a result, the possible desorption products are  $\text{As}_4$ ,  $\text{AsMe}_3$ ,  $\text{AsH}_3$ ,  $\text{H}_2\text{O}$ ,  $\text{CH}_4$ ,  $\text{C}_2\text{H}_6$ ,  $\text{C}_2\text{H}_4$  and/or  $\text{OMe}_2$ . The surface structures that we have generated (reaction intermediates) are linked together in order to reveal plausible reaction sequences. However, we have computed no actual pathways linking the structures (except where reactions occurred spontaneously during geometry optimizations, *e.g.* formation of  $\text{As} - \text{As}$  dimers). Transition state searches on a

more realistic model of the oxidized surface would be needed for this and the activation energies would give important information on the kinetics (albeit within the limited accuracy of DFT for activation energies). However, such a model would require a larger simulation cell and an improved description of van der Waals forces, which together would push the computational demands beyond current resources. In the absence of activation energies though, we can still discuss the overall shape of the potential energy surface formed by the minimum energy structures presented here.

Despite its limitations, the chosen surface model for As<sub>2</sub>O<sub>3</sub> as part of an oxidized III-V substrate is able to reproduce energetics for reactions like TMA adsorption or CH<sub>4</sub> formation which are in very good agreement with the same reactions reported on an Al<sub>2</sub>O<sub>3</sub> substrate [112]. Apparently, the molecular nature of arsenolite and its zero surface energy has a negligible effect on its reactivity with TMA, which is similar to that on other oxide surfaces. This suggests that TMA is a sufficiently strong combination of Lewis acidic Al and Lewis basic Me to adsorb and decompose on most oxide surfaces. Nevertheless we note that reconstructions of arsenolite are not accurate here because van der Waals forces are not taken into account. For this reason, we do not form any conclusions about the effect of multiple decomposition reactions in breaking As<sub>4</sub>O<sub>6</sub> cages and replacing them with a surface film of Al<sub>2</sub>O<sub>3</sub> and/or elemental As.

We assume that on the hydroxylated native oxide surface, protons are primarily eliminated as CH<sub>4</sub>, which does not affect As-O bonding and has little contribution to the ‘clean-up’ effect. Other mechanisms like OH transfer are excluded by the high exothermicity of methane formation, *i.e.*:



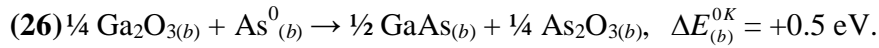
Therefore, as proposed before [10, 61, 62], the driving force behind the ‘clean-up’ mechanism is breaking As – O bonds and forming Al – O bonds. Since this transformation is achieved by all of the reactions (1)-(7) proposed here, it is reasonable that the calculations show them all to be exothermic. More surprisingly, we find that As – O bonds are also eliminated in a redox process when As – As dimers are formed, but this is not so energetically favorable. Therefore we can propose alternative reagents (*e.g.* AsH<sub>3</sub>) that should remove As<sub>2</sub>O<sub>3</sub> without the formation of Al<sub>2</sub>O<sub>3</sub> and this may be an interesting avenue for future experiments. Our calculations show that all the net bulk reactions are energetically downhill and we conclude that these reactions might occur simultaneously on the oxidized III-V substrate.

Bulk and surface energetics agree in the overall trend for reactions (1)-(6). Both methods predict reactions (6), (5) and (2) to be almost equally exothermic around a typical ALD temperature range, then reaction (3) and (1), with the least favored being reaction (4), in that order up to  $T \approx 750$  K. Above this temperature reaction (6) is more exothermic than (5), (2) and (3); (4) more favored than (1) (see [Figure 3-1](#) and [Figure 3-8](#)).

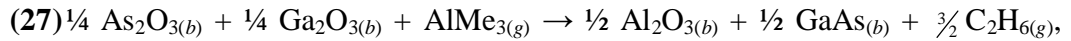
Although reaction (7) was not modeled explicitly on the surface, it is clear to us that the various pathways responsible for partial carbon oxidation (surface reactions (2)-(6)), may lead eventually to complete carbon oxidation in reaction (7) if there is enough reactant on the surface. Thermodynamics alone favor reaction (7), with products As<sub>4</sub>, CO<sub>2</sub> and H<sub>2</sub>O. However we argue that the multiple steps involved in ‘clean-up’ mean that thermodynamic products are not always accessible. Reaction (7) would need total decomposition of TMA and transfer of twenty-four electrons from C to As, as mentioned before. It is important to ask whether reactions (2), (3), (5), (6) and (7) will proceed without interruption until twelve electrons have accumulated in four surface arsenic atoms, allowing desorption as As<sub>4</sub>. Some possible competing reactions are now discussed.

The energetics of ligand transfer favor  $\parallel\text{As} - \text{Me}$  over  $\parallel\text{O} - \text{Me}$  and over  $\parallel\text{As} = \text{CH}_2$  (section 3.5) and drive towards  $\text{AsMe}_3$  (reaction (1)). However, if  $\text{O} - \text{Me}$  does occur, we predict that it will combine with any neighbouring  $\parallel\text{M} - \text{Me}$  to give  $\text{C}_2\text{H}_6$  (reaction (2)), desorbing irreversibly and precluding the Me group from losing a proton and forming  $\text{C}_2\text{H}_4$  (reactions (5)-(6)). This leaves partially reduced As at the surface, which is also precluded from desorbing as  $\text{AsMe}_3$ . As shown in Figure 3-4, the statistics of ligand diffusion favor this outcome. Alternative side-reactions (5) and (6), although energetically more favored, are statistically less likely, since these mechanisms require proton diffusion. Reactions (3) and (4) are both energetically and statistically less likely than (2). Therefore, reaction (2) may indeed predominate to a sufficient extent that four TMA adsorptions on  $\text{As}_2\text{O}_3$  yield a sequence of six desorbing  $\text{C}_2\text{H}_6$  molecules, followed by desorption of one  $\text{As}_4$  molecule.

On oxidized III-V substrates however, there are more possibilities for consumption of partially-reduced arsenic before desorbing as  $\text{As}_4$ . For instance, reduced arsenic may ‘getter’ oxygen from gallium oxide on the surface, driven by the formation of GaAs:



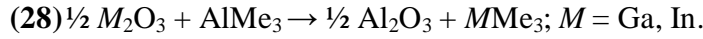
Adding this to reaction (2) we obtain:



$$\Delta G_{(b)}^{573K} / \Delta E_{(b)}^{0K} = -4.7/-4.9 \text{ eV},$$

which masks the fact that multiple partially-reduced As atoms at the surface are involved in this overall reaction. A similar reaction may be written for  $\text{In}_2\text{O}_3$  and InAs with computed  $\Delta G_{(b)}^{573K} / \Delta E_{(b)}^{0K} = -4.8/-5.0 \text{ eV}$ . Reaction (27) illustrates that, on the oxidized III-V surface, GaAs or InAs are possible sinks for the III-V elements, rather than volatile molecules like  $\text{As}_4$ ,  $\text{AsH}_3$ ,  $\text{AsMe}_3$ ,  $\text{GaMe}_3$  and  $\text{InMe}_3$ .

The technological interest is in applying this reaction to the removal of all native oxides from III-V substrates prior to deposition of a high- $k$  dielectric for an MOS structure. Therefore, having established the mechanism by which TMA achieves ‘clean-up’ of  $\text{As}_2\text{O}_3$ , we now consider whether this works on other native oxides. The native oxides that have been detected on  $\text{In}_{0.53}\text{Ga}_{0.47}\text{As}$  are  $\text{As}_2\text{O}_3$ ,  $\text{As}_2\text{O}_5$ ,  $\text{Ga}_2\text{O}_3$  and  $\text{In}_2\text{O}_3$  [11, 62, 83]. The less stable form of arsenic oxide  $\text{As}_2\text{O}_5$  is likely to be even more susceptible to reduction *via* reactions (2) than  $\text{As}_2\text{O}_3$ . By contrast,  $\text{Ga}_2\text{O}_3$  and  $\text{In}_2\text{O}_3$  are stable in oxidation state +3, and non-redox reaction (1) is the only likely candidate for TMA to directly ‘clean-up’ these oxides:



Calculated bulk energetics show that reaction (28) will take place:  $\Delta G_{(b)}^{573K} / \Delta E_{(b)}^{0K} = -2.1/-2.4$  eV for  $M = \text{Ga}$  and  $\Delta G_{(b)}^{573K} / \Delta E_{(b)}^{0K} = -2.1/-2.0$  eV for  $M = \text{In}$ . However, these energies are much smaller in magnitude than for  $M = \text{As}$  (see section 3.2, reaction (1)) and this might explain why arsenic oxides are more effectively cleaned-up than group III oxides by TMA [10, 11, 61, 62]. An analogous reaction is proposed in the literature [113] by which  $\text{SiO}_2$  is converted by TMA to  $\text{SiMe}_4$  at temperatures above 600 K (325°C), which is in that case supported by the relative formation energies of the oxides. We have recently proposed that the ‘clean-up’ of  $\text{Si}_3\text{N}_4$  by TMA may explain the substrate-enhanced ALD growth rate for  $\text{Al}_2\text{O}_3$  on this substrate [114]. However, as shown above, indirect ‘clean-up’ of gallium and indium oxides may also be possible *via* partially-reduced arsenic at the surface, driven by the formation of GaAs and InAs ((26), (27)). Indeed, this mechanism was subsequently confirmed in a very detailed and precise SRPS measurement, where it was showed that the  $\text{As}^{3+}$  component decreased rapidly in the first 2 pulses of TMA, while at the same time the As suboxide component increased. What is

more, the Ga<sup>3+</sup> signal started to decrease only from the second pulse onwards along with the As suboxide component. [63]

Based on our results, we suggest the following reasons why TMA works well in ‘clean-up’ of arsenic oxides. Firstly, it is stable against auto-decomposition in the gas phase (up to circa 640 K [31-33]) and so is delivered to the surface intact. Secondly, it is a Lewis acid and adsorbs strongly onto oxide surfaces, ensuring an adequate lifetime on the surface for subsequent decomposition. Third, ligand transfer, driven by formation of Al – O, leads to a variety of decomposition pathways, which all produce solid Al<sub>2</sub>O<sub>3</sub> and various gas-phase molecules containing C, H and As. The anionic Me groups in TMA are reducing agents and the thermodynamically predominant pathway for metalloid oxides is reduction, producing volatile molecules (*e.g.* As<sub>4</sub>, reactions (2)-(6)) or gettering oxygen from less reducible oxides (*e.g.* those of Ga, reaction (26)). An alternative pathway is non-redox ligand exchange (reactions (1), (28)), which allows non-reducible oxides (*e.g.* SiO<sub>2</sub>) to be cleaned-up; the key here is a strong bond between the ligand and the ion to be cleaned-up. We conclude therefore that the performance of ‘clean-up’ depends strongly on the electropositivity of the precursor metal, on the affinity of the precursor ligand to the oxide, and also on the chemical character of the oxide to be cleaned-up.

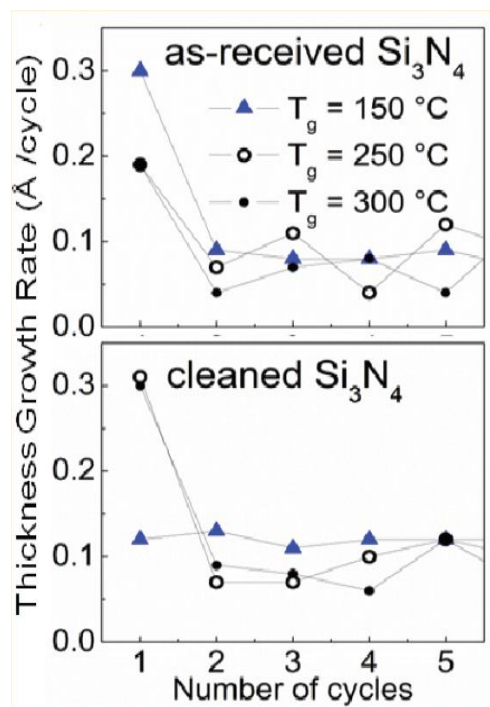
### 3.9 Conclusion

In this chapter we have proposed ligand transfer and ligand transfer accompanied by charge transfer as the mechanism of removal of As – O bonds on an oxidized GaAs or InGaAs substrate in the very first pulse of TMA during ALD of Al<sub>2</sub>O<sub>3</sub>, the process known as ‘clean-up’. In the light of the ligand dissociation in TMA molecule on the solid surface, we have investigated its stability in the gas phase by computing reaction energies for homolytic and heterolytic dissociation of methyl from Al center. The calculated dissociation energies suggest that the TMA molecule is moderately stable and is delivered



to the surface intact. From the computed thermodynamics (both in terms of potential energies and reaction statistics), we predict that the ‘clean-up’ of III-V native oxides mostly produces As<sub>4</sub> gas, but also GaAs solid or InAs solid. Most C is predicted to form C<sub>2</sub>H<sub>6</sub> (reaction (2)) but with some C<sub>2</sub>H<sub>4</sub>, CH<sub>4</sub> and H<sub>2</sub>O, and these products should be detectable during the TMA pulse. A wide variety of mechanisms are exothermic and therefore competitive. In all cases, Al<sub>2</sub>O<sub>3</sub> is formed in direct contact with the III-V substrate (*e.g.* Ga-O-Al linkages). We speculate that ||As-Me will be the most abundant surface intermediate, as well as transient ||As-As|| and ||O-Me that are markers for reactions (2)-(6), but we also note the necessity of assessing the kinetics of the proposed reactions in the future. As TMA exposure continues, ‘clean-up’ of the native oxides will finish and the surface will become covered with species like ||Al-Me, ||Ga-Me, ||In-Me and ||Al-Me<sub>2</sub> *etc.* We propose alternative reagents (*e.g.* AsH<sub>3</sub>) that should remove As<sub>2</sub>O<sub>3</sub> without the formation of Al<sub>2</sub>O<sub>3</sub>. ‘Clean-up’ of an oxide film is shown to strongly depend on the electropositivity of the precursor metal, affinity of the precursor ligand to the oxide and the redox character of the oxide. The predominant pathway for a metalloid oxide such as arsenic oxide is reduction, producing volatile molecules or getting oxygen from less reducible oxides. An alternative pathway is non-redox ligand exchange, which allows non-reducible oxides to be cleaned-up. This improved understanding of the chemical principles underlying ‘clean-up’ allows us to rationalize and predict how other precursors perform the reaction.

#### 4 Mechanisms for substrate-enhanced growth during the early stages of atomic layer deposition of alumina onto silicon nitride surfaces



The atomic layer deposition (ALD) of aluminum oxide ( $\text{Al}_2\text{O}_3$ ) from trimethylaluminium and water on silicon nitride was studied on as-received and HF-cleaned  $\text{Si}_3\text{N}_4$  surfaces. In situ spectroscopic ellipsometry during ALD, X-ray photoelectron spectroscopy, X-ray reflectivity, and time-of-flight secondary ion mass spectrometry were used to elucidate the growth rate, the chemical composition, and the density of  $\text{Al}_2\text{O}_3$ . These measurements were carried out at the MDM laboratory, Italy by L. Lamagna's and co-workers and are summarized in section 4.1.1. The effect of the substrate cleaning and of the growth temperature -varied in the 150–300 °C range- were analyzed by considering first principles calculations of the early stages of the growth on both  $\text{Si}_3\text{N}_4$  and  $\text{SiO}_2$  surfaces. Our work evidenced how not only complete ALD cycles (work conducted by M.E. Grillo and co-workers; summarized in section 4.1.2) but also complementary non-ALD reactions (our results, section 4.3) can account for the observed peculiarities related to the enhanced or inhibited growth rates on the  $\text{Si}_3\text{N}_4$  surfaces as a function of temperature.

Published as part of: Lamagna, L.; Wiemer, C.; Perego, M.; Spiga, S.; Rodríguez, J.; Santiago Coll, D.; Grillo, M. E.; Klejna, S.; Elliott, S. D., *Mechanisms for Substrate-Enhanced Growth during the Early Stages of Atomic Layer Deposition of Alumina onto Silicon Nitride Surfaces*. Chemistry of Materials 2012, 24 (6), 1080-1090.

## 4.1 Introduction

The increasing demand for more compact memory storage devices from a variety of electronic applications motivates the development of non-volatile flash memories based on the charge trapping mechanism of silicon nitride as in the SONOS device structure [115]. In the SONOS structure, the charge is trapped within a layer of amorphous silicon nitride ( $\text{Si}_3\text{N}_4$ ), inserted between two silicon oxide layers ( $\text{SiO}_2$ ), which act as tunnel dielectric and blocking layer to prevent charge injection from the control gate. A high dielectric constant (high- $k$ ) dielectric, such as alumina ( $\text{Al}_2\text{O}_3$ ) may alternatively be used as blocking oxide; this yields a good programming efficiency while allowing a thicker tunnel oxide and avoiding the retention issue [116, 117]. In this way, a higher field on the tunnel oxide will be obtained for the same applied voltage. Still, compatibility of the materials at the interface can be crucial to the desired mechanical and electrical properties. One of the key issues for the integration of materials into the memory stack is good electrical quality of the interface between  $\text{Al}_2\text{O}_3$  and  $\text{Si}_3\text{N}_4$ . Hence, a fundamental understanding of the deposition process is required in order to tailor the quality of the  $\text{Al}_2\text{O}_3$  film and its interfacial properties. To this end, the early stages of the deposition of  $\text{Al}_2\text{O}_3$  on silicon nitride and oxide surfaces have been studied in the present work by both theoretical and experimental techniques (the latter at MDM laboratory, Italy [118]).

Our aim is to characterise and understand the ALD growth process on a  $\text{Si}/\text{SiO}_2/\text{Si}_3\text{N}_4$  substrate, layer-by-layer at the atomic level, with the goal of controlling interface formation *e.g.*, *via* use of appropriate surface cleaning or deposition temperature. We consider here  $\text{Al}_2\text{O}_3$  on  $\text{Si}_3\text{N}_4$  substrates, but the approach may be applicable to other systems. We specifically seek to understand how substrate preparation affects the subsequent reaction with precursors (TMA and  $\text{H}_2\text{O}$ ) and what the consequences are for interfacial characteristics.

Here, we propose three possible chemical scenarios that may be at play during the growth from cycles of pulsed TMA and H<sub>2</sub>O. (i) The preparation of the substrate may affect the rate of the standard, self-limiting ALD reaction of TMA, primarily *via* the coverage of hydroxyl groups on the substrate (the reactive sites in equation (1) below). (ii) TMA is a reactive molecule and can be expected to undergo other (non-ALD) reactions depending on the chemical nature of the substrate, either contributing extra product or etching the substrate away. (iii) Steady-state ALD of Al<sub>2</sub>O<sub>3</sub> onto Al<sub>2</sub>O<sub>3</sub>. In the simplest case, substrate effects are limited to the earliest few ALD cycles, until a single monolayer of interfacial layer (IL) is formed, which is then followed by steady-state growth. However, the situation may be complicated if substrate and product mix to form a more extended inter-layer (IL) with its own distinct growth chemistry, as often the case when using an aggressive oxidizing agent such as ozone (O<sub>3</sub>) [119-121]. Alternatively, the product may grow as islands that ripen into a closed layer only after many ALD cycles.

#### 4.1.1 Summary of experimental results

Ultra-thin Al<sub>2</sub>O<sub>3</sub> films were deposited at MDM laboratory using TMA and H<sub>2</sub>O on Si<sub>3</sub>N<sub>4</sub> surfaces at different temperatures. The growth rates of the first few Al<sub>2</sub>O<sub>3</sub> monolayers were determined by *in situ* spectroscopic ellipsometry (SE). X-ray photoemission spectroscopy (XPS), time of flight secondary ion mass spectroscopy (ToF SIMS) and X-ray reflectivity (XRR) were used *ex situ* to assess the chemical composition, thickness and electron density of the substrates and films. The rate of alumina growth per ALD cycle was reported in two ways: the thickness growth rate (TGR), expressed in Å.cycle<sup>-1</sup>, and the molar growth rate (MGR), expressed in Al<sub>2</sub>O<sub>3</sub>.nm<sup>-2</sup>.cycle<sup>-1</sup>. The MGR can be converted to the TGR by dividing by the density of Al<sub>2</sub>O<sub>3</sub> units in the film (Al<sub>2</sub>O<sub>3</sub>.nm<sup>-3</sup>) and multiplying by ten.

XPS analysis indicated that the as-received Si<sub>3</sub>N<sub>4</sub> surface is covered by a SiO<sub>2</sub>-like native oxide, while the sample that was cleaned with HF showed a much reduced O signal. In the range of temperatures 150-300 °C, the chemical structure of the Al<sub>2</sub>O<sub>3</sub>/Si<sub>3</sub>N<sub>4</sub> interface in the final stack is strictly related to the specific chemistry of the starting Si<sub>3</sub>N<sub>4</sub> surface, *i.e.* that the final Al<sub>2</sub>O<sub>3</sub>/Si<sub>3</sub>N<sub>4</sub> interface depends on the initial state of the Si<sub>3</sub>N<sub>4</sub> surface. *In situ* SE shows that initial growth is always substrate-enhanced on as-received surfaces at low growth temperatures, while on HF-treated surfaces, the initial stages of the growth are substrate enhanced at 250°C and 300°C. An immediate transition from the high-rate reaction to a constant TGR ('steady- state') is observed after the first ALD cycle. A peculiar behaviour is detected when ALD is performed on cleaned Si<sub>3</sub>N<sub>4</sub> at 150°C. On as-received samples the XRR data show substrate-enhanced MGR at 150°C but substrate-reduced MGR at 250-300°C, both leading to low-density ILs, while the cleaned Si<sub>3</sub>N<sub>4</sub> substrates show no IL in XRR and no change in the MGR, regardless of temperature. [114]

#### 4.1.2 Summary of other theoretical results

Experimental [31] and theoretical [112] evidence indicates that the following reaction mechanism underlies the ALD of Al<sub>2</sub>O<sub>3</sub> from TMA and H<sub>2</sub>O. In both precursor pulses, the first step is chemisorption of the precursor onto unsaturated sites on the surface of the growing film: H<sub>2</sub>O onto Lewis acidic surface Al (surf-Al) and TMA onto Lewis basic surf-O or surf-OH. The adsorbed precursor may dissociate *via* further unsaturated sites (protons from H<sub>2</sub>O transferring to surf-O or Me ligands transferring to surf-Al) [112]. Combination of the surface-bound moieties is the reaction by which ligands are eliminated from the surface:



Assuming facile diffusion of ligands/protons, this elimination reaction will proceed, freeing up sites for further adsorption. In the TMA pulse, all residual protons from the previous H<sub>2</sub>O pulse will eventually be eliminated from the surface and a saturating coverage of Me ligands will be obtained. At this point, there are no unsaturated sites for TMA adsorption. This self-limiting chemistry in the TMA pulse ensures an upper limit on the amount of Al deposited per cycle, which is characteristic of ideal ALD. From the point of view of the substrate, we can identify requirements for the ideal ALD mechanism to occur: Lewis acidic/basic sites for chemisorption and the capacity to produce surface protons that are sufficiently Brønsted acidic for elimination. Therefore, density functional theory (DFT) was used to compute the surface acidity and hydroxyl coverage of nitride and oxide surfaces, both bare and hydroxylated, in order to estimate the effect of the substrate on the growth reactions and growth rates of ideal ALD.

Two representative models were created for the as-received and cleaned Si<sub>3</sub>N<sub>4</sub> surfaces in order to analyze the potential surface reactivity towards TMA and H<sub>2</sub>O pulses. Moreover, the effects of the surface acidity on the growth rate were taken into account.  $\alpha$ -SiO<sub>2</sub>(111) was selected as the model for the as-received samples. In this case the high MGR of the IL detected at a growth temperature of 150°C could not be explained by standard ALD reactions on hydroxylated SiO<sub>2</sub>. On the other hand, the finding of a low MGR for the IL at 300°C is consistent with standard ALD predicted from DFT, *i.e.*, the substrate-retarded MGR is due to low coverage of OH on hydroxylated SiO<sub>2</sub> at 250-300°C.

$\beta$ -Si<sub>3</sub>N<sub>4</sub>(0001) was chosen as the model for cleaned samples. A constant and temperature-independent MGR is consistent with standard ALD, since the OH coverage of hydroxylated Si<sub>3</sub>N<sub>4</sub> is predicted by DFT to be approximately equal to that of hydroxylated Al<sub>2</sub>O<sub>3</sub> in steady-state regime and to be also temperature-independent.

Therefore, in this case the SE observation of substrate-enhancement at 250 and 300°C could not be explained. [114]

Obtaining a higher experimental growth rate than the prediction, indicates that the reaction of TMA with the surface is not self-limiting and that a different mechanism is contributing to the growth of the oxide. In this chapter we present our findings on alternative growth mechanisms also investigated with DFT.

## 4.2 Computational method

We consider two models for alumina deposition: as-received (oxidized) (which means covered with silicon oxide) and HF-cleaned  $\text{Si}_3\text{N}_4$  (“cleaned”) in section 4.3. All bulk and surface structures were calculated using the generalized gradient approximation to DFT of Perdew, Burke and Ernzerhof (PBE) [97] and the all-electron projector-augmented wave (PAW) method [122] as implemented in the VASP package [79, 123]. Other DFT codes were used for specific analysis, as noted below.

### 4.2.1 Models of bulk crystals

The total energy versus volume of bulk  $\alpha\text{-SiO}_2$  in the crystalline  $\alpha$ -quartz trigonal structure  $D_6^3$  was optimized with respect to the crystallographic lattice parameters  $a$  and  $c/a$ , and to the internal coordinates of the 9 atoms (6 O and 3 Si) per unit cell. A grid of ( $3 \times 3 \times 3$ ) special points for Brillouin zone integrations and a kinetic energy cut-off of 400 eV was adopted in the calculations. The optimized lattice parameters  $a$  of 4.980 Å and  $c/a$  of 1.09 thereby obtained are consistent with experimental values of 4.913 Å and 1.10, respectively [124]. The hexagonal primitive cell of  $\beta\text{-Si}_3\text{N}_4$  with space group  $P6_3m$  was also optimized with respect to the crystallographic lattice parameters and to the four inner parameters of the coordinates of the 14 atoms (6 Si and 8 N) per unit cell. A detailed description of the computational set-up, and account of the resulting bulk structure has

been published elsewhere [125]. A model of  $\alpha$ -Al<sub>2</sub>O<sub>3</sub> was optimized with a 500 eV cut-off and 48  $k$ -points (4×4×2 Monkhorst-Pack grid). Geometry optimisation of both ion and cell coordinates was performed to a convergence of less than 10<sup>-3</sup> eV. The resulting equilibrium lattice parameters agreed well with experiment:  $a = 4.808 \text{ \AA}$ ,  $c/a = 2.731$  (experimental values:  $a = 4.759 \text{ \AA}$ ,  $c/a = 2.730$ ) [82].

#### 4.2.2 Models of substrate surfaces

The natural cleavage plane (0001) of  $\beta$ -Si<sub>3</sub>N<sub>4</sub>, consisting of nearly planar stoichiometric layers, was adopted to model the cleaned substrate. The bulk truncation exhibits unsaturated three-coordinated Si and two-coordinated N sites. For direct TMA interaction with bare silicon nitride surface, 2×2 supercell was used with three stoichiometric layers of Si<sub>3</sub>N<sub>4</sub> and 15 Å of vacuum layer. The calculations used Brillouin zone integration at 2×2×1 Monkhorst-Pack  $k$ -point mesh (six irreducible  $k$ -points), a plane-wave cut-off of 400 eV and a 0.2 meV.Å<sup>-2</sup> threshold for atomic forces.

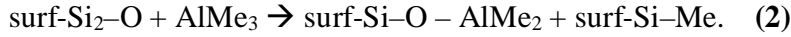
#### 4.2.3 Models of gas-phase molecules

For the gas-phase species, optimisation was performed in a cubic or orthorhombic simulation box with sides of at least 15 Å, with six  $k$ -points at the edges of the first Brillouin zone to reduce spurious interaction through periodic boundary conditions. The free energy change was computed from  $\Delta G = \Delta E - T\Delta S_{\text{gas}}$ , assuming negligible contribution to entropy changes from the solid surfaces with adsorbates. Entropies of gaseous species ( $S_{\text{gas}}$ ) were computed by vibrational analysis using the non-periodic code TURBOMOLE [95]. These calculations used unrestricted DFT within the PBE parametrization [97], the resolution-of-the-identity approximation [98, 99] and atom-centred triple-zeta valence basis functions, augmented by double polarization functions TZVPP2 [100].

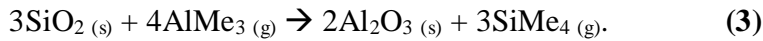


### 4.3 Non-ALD decomposition reactions

It is well known that on silica surfaces, TMA reacts with equal probability with OH groups of silica in a Brønsted acid-base reaction (Equation (1)) and with siloxane bridges through dissociation [18, 126-129]:



It is observed that repeated dissociation of methyl groups leads to surf-Si-Me<sub>x</sub> (x = 1, 2, 3) and can therefore lead to desorption of SiMe<sub>4</sub> according to:



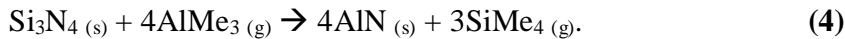
For this overall reaction, we compute  $\Delta E_{\text{bulk}} = -6.7$  eV and  $\Delta G_{\text{bulk}}^{300^\circ\text{C}} = -9.7$  eV, showing that it is thermodynamically favourable. For comparison, note that the ALD reaction (Equation (1)) is computed by the same method to show  $\Delta E_{\text{bulk}} = -23.7$  eV for 4AlMe<sub>3</sub> over an entire ALD cycle.

Desorption of SiMe<sub>4</sub> was measured with Quadrupole Mass Spectroscopy (QMS) by Bartram *et al.* [113]. It is shown that by 325°C multiple methyl groups bind to silicon atoms in sufficient concentration to form SiMe<sub>4</sub>. This leads to substitution of Al for Si and accommodation of Al in the silica lattice. The Al – Si interdiffusion has also been reported by Levy *et al.* [130]. Other indications of desorption of SiMe<sub>4</sub> can be found in NMR measurements by Lakomaa *et al.* [33], where the OSiMe<sub>3</sub> peak disappears after the first reaction cycle of Al<sub>2</sub>O<sub>3</sub> ALD. A similar effect of TMA on oxides is also found in the literature for III-V substrates. Removal or reduction of Ga and As oxides after the first pulse of TMA during ALD of alumina on oxidised GaAs and InGaAs substrates was reported by many groups [12, 55, 62, 107].

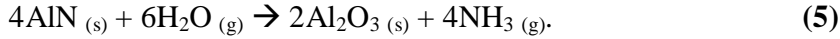
The mechanism responsible for this ‘clean-up’ effect was found to be complicated [131], involving reduction of metalloids like As, but also transfer of the methyl ligands from Al to the substrate, like the one proposed here for the silicon oxide.

ToF-SIMS shows that SiO<sub>2</sub> remains at the interface after deposition, which implies that any ‘clean-up’ of the native oxide has not gone to completion. Nevertheless, this non-ALD reaction would explain the SE observation of substrate-enhanced TGR in the first cycle on as-received samples. However, XRR shows this to be spread over multiple cycles and (when correlated with the low density of the IL) to generate a MGR enhancement at 150°C and a MGR depletion at 250-300°C. By contrast, a non-ALD decomposition of TMA like this would be expected to become more dominant as temperature is raised. SE and XRR analyses therefore argue against such a reaction taking place.

By analogy with the reaction of TMA on silica and III-V substrates, we can propose instead the following reaction on bare silicon nitride:



In a subsequent H<sub>2</sub>O pulse, the AlN product can be hydrolysed:



Our calculations of the bulk energetics show that these processes are exothermic ( $\Delta G_{\text{bulk}}^{300^\circ\text{C}}/\Delta E_{\text{bulk}} = -5.3/-8.2$  eV and  $-5.7/-8.0$  eV for Equation (4) and Equation (5), respectively) and that the effect of temperature on these reactions is fairly constant.

Using the Si<sub>3</sub>N<sub>4</sub> (0001) slab as a representative surface for the “cleaned” substrate, we have computed surface intermediates that are likely to occur during the individual methyl transfer steps of Equation (4). As shown in [Table 4-1](#) and [Figure 4-1](#), the surface reaction producing SiMe<sub>4</sub> is exothermic. Although no activation energies were computed here, we do see uphill steps between minimum-energy intermediates in the surface reaction, corresponding to crowding between multiple methyl groups on one Si. It is therefore reasonable to suggest that the reaction is limited by kinetics and is more likely to proceed as temperature of growth is raised.

Therefore, if a non-ALD reaction such as Equations (4) and (5) is responsible for

substrate-enhanced growth, we would expect the effect to increase with temperature. Indeed, SE experiments indicate that some substrate-enhanced TGR occurs in the first cycle at 250-300°C on the cleaned sample, but not at 150°C. This can not be accounted for by standard ALD reactions on hydroxylated Si<sub>3</sub>N<sub>4</sub>, so it may be a non-ALD reaction. While XRR sees no difference in density or MGR over the 150-300 °C temperature range, this may simply indicate that the non-ALD and ALD-derived products are both Al<sub>2</sub>O<sub>3</sub> of similar density.

Reaction intermediate	$\Delta E_{(\text{surf})}^{0 \text{ K}}$ [eV]	$\Delta G_{(\text{surf})}^{573.15 \text{ K}}$ [eV]
Si <sub>3</sub> N <sub>4</sub> (surf) + AlMe <sub>3</sub> (g)	0.0	0.0
-AlMe <sub>2</sub> +   Si-Me	-2.7	0.5
-AlMe + 2   Si-Me	-5.8	-2.6
-AlMe +   Si-Me <sub>2</sub>	-2.0	1.1
-Al +   Si-Me <sub>3</sub>	-3.6	-0.4
3   Si + 4 AlMe <sub>3</sub> (g) → 4   -Al + 3 SiMe <sub>4</sub> (g)	-6.7	-3.7

**Table 4-1 Reaction energies for mechanism of TMA dissociation on cleaned Si<sub>3</sub>N<sub>4</sub>, quoted relative to gas-phase TMA and the bare Si<sub>3</sub>N<sub>4</sub> (0 0 0 1) surface.**

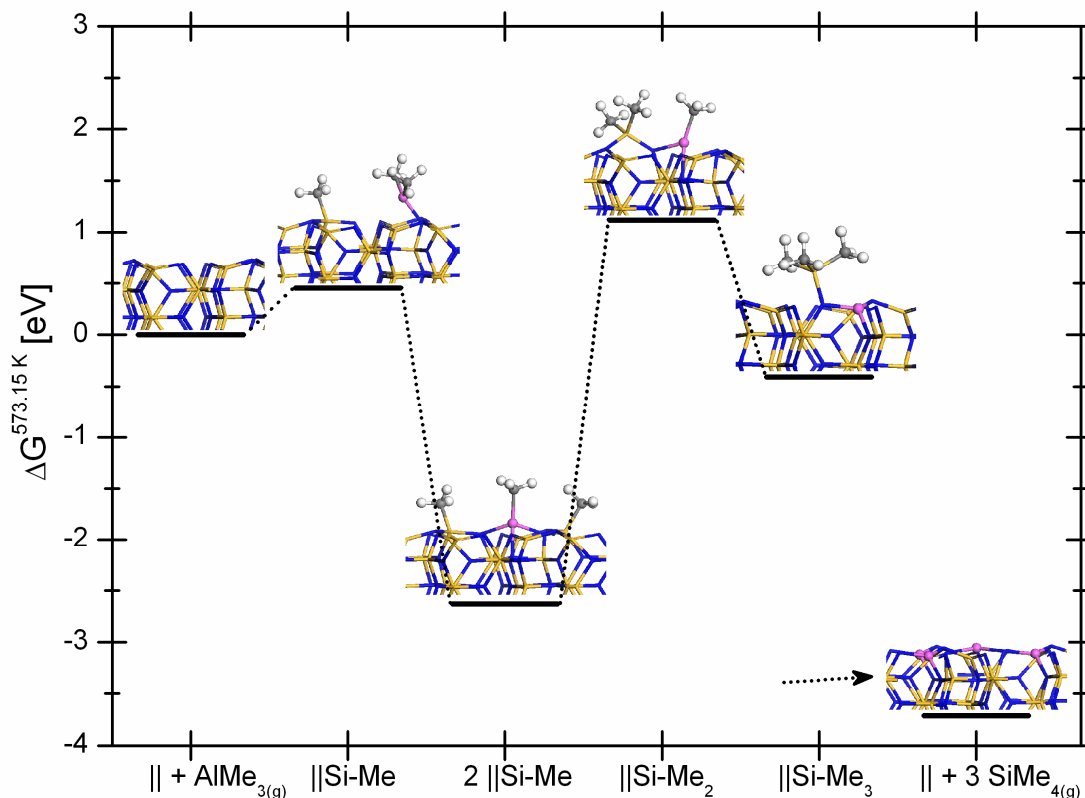


Figure 4-1 Potential energy surface showing minima for mechanism of TMA dissociation on bare  $\text{Si}_3\text{N}_4$ . Corresponding reactions and numerical values are shown in Table 4-1.  $\Delta G_{(\text{surf})}^{573.15 \text{ K}}$  computed under the assumption of zero change in surface entropies. Ball and stick representations of surface models: yellow Si, blue N, pink Al, grey C and white H.

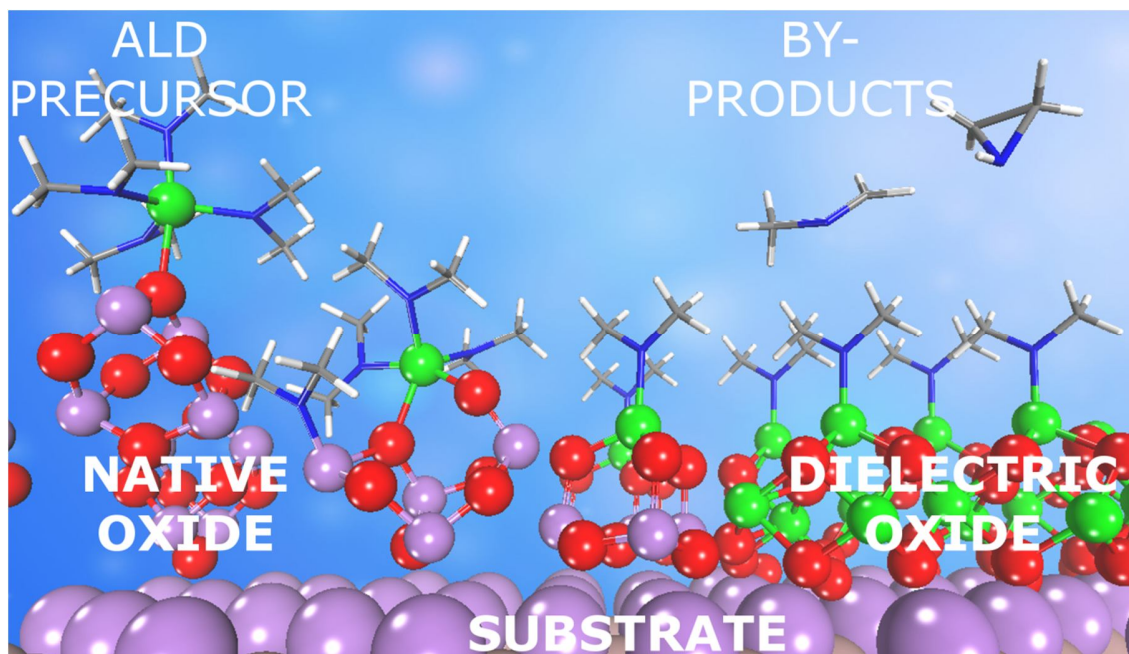
#### 4.4 Conclusion

A detailed *in situ* and *ex situ* characterisation of the ALD process and products provided an almost complete analysis of the growth details, confirming some expectations but also revealing some peculiar behaviour. In particular, substrate-enhanced growth was revealed in the first ALD cycle and tentatively addressed, both taking into account the film structural and chemical properties and the surface chemistry and reactivity. Theoretical calculations accounting for the different starting substrates provided possible explanations for the experimentally-revealed anomalous growth step. Combining theory and experiment, we thus suggest the following mechanisms for substrate-directed growth occurring during the early stages of ALD.

Standard ALD alone gives substrate-enhanced (low growth temperature) or substrate-retarded growth (high growth temperature) on oxidised and hydroxylated ( $\text{SiO}_2$ -like) substrates. Both result in a monolayer of low-density alumina IL, after which steady-state alumina ALD proceeds and forms the main part of the film. By contrast, non-ALD decomposition of TMA on HF-cleaned silicon nitride at high growth temperature can explain substrate-enhanced growth in that case. However, no effect on layer density is observed and there is no evidence of the formation of an IL.

Given the results from experimental data and theoretical modeling, an HF treatment for cleaning the  $\text{Si}_3\text{N}_4$  substrate would be recommendable. To obtain an abrupt  $\text{Al}_2\text{O}_3/\text{Si}_3\text{N}_4$  interface with minimal side-reactions during the early stages of ALD, a growth temperature of  $150^\circ\text{C}$  appears to be suitable.

## 5 Decomposition of metal alkylamides, alkyls and halides for self-cleaning atomic layer deposition of dielectrics onto III-V substrates



*An interfacial cleaning mechanism has been observed during ALD of  $\text{Al}_2\text{O}_3$ ,  $\text{HfO}_2$ ,  $\text{TiO}_2$  and  $\text{Ta}_2\text{O}_5$  with various degrees of success. We undertake a comprehensive study using density functional theory (DFT) to explain differences in the performance of various classes of precursor chemicals in removing native oxide from III-V substrates. The study covers the metals Ta(V), Ti(IV), Zr(IV), Hf(IV), Al(III), Mg(II) combined with methyl, amide and chloride ligands. We show that the electropositivity of the metal cation determines the clean-up ability of the precursor and so clean-up is most effective when depositing MgO. Clean-up with metal alkylamides has a similar mechanism to clean-up with metal methyls insofar as oxygen is scavenged by the metal. The difference in operation of alkylamide and methyl ligands lies in the affinity of the ligand to the substrate. Alkylamide is shown to be prone to decomposition rather than the migration of the entire ligand evinced by methyl. We investigate the multi-step chemical processes associated with decomposition of alkylamide. These results explain the experimentally-observed accumulation of metallic arsenic and arsenic suboxide at the interface. Such understanding can help achieve control of oxide-semiconductor interfaces through the appropriate choice of chemical precursor.*

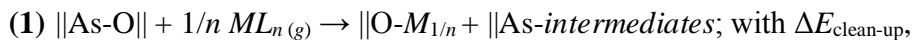
## 5.1 Introduction

In this study we try to provide an improved understanding of the chemical principles underlying ‘clean-up’ and thus rationalize the experimental observations. An interfacial cleaning mechanism has been observed during ALD of  $\text{Al}_2\text{O}_3$ ,  $\text{HfO}_2$ ,  $\text{TiO}_2$  and  $\text{Ta}_2\text{O}_5$  with various degrees of success. We consider the process of clean-up of oxides from some technologically relevant III-V surfaces; namely As(III), Ga(III) and In(III) oxide with more detailed investigation of the example of arsenic (III) oxide for surface reactions. For this surface, we focus mainly on clean-up process utilizing  $\text{Hf}[\text{N}(\text{CH}_3)_2]_4$  during  $\text{HfO}_2$  ALD. Decomposition of the dimethylamido ligand (dma) is studied by first principles methods, assuming formation of the dielectric oxide as the driving force for the clean-up effect. This allows us to look explicitly at the interaction of the precursor’s ligand with the III-V oxide surface and investigate potential redox properties of the ligand. A set of general reactions is generated and comparison is made between the mechanisms of interfacial cleaning with different metal precursors: alkylamides, methyls and chlorides.

## 5.2 Computational method and approach

In this investigation we consider the process where the adsorbed metal precursor molecules, with the general formula  $ML_n$  ( $M = \text{Mg(II)}, \text{Al(III)}, \text{Ti(IV)}, \text{Zr(IV)}, \text{Hf(IV)}, \text{Ta(V)}$ ;  $L = [\text{N}(\text{Me})_2]^-$ ,  $[\text{Me}]$ ,  $[\text{Cl}]^-$ ;  $n = \text{oxidation state of metal}$ ), undergo a series of clean-up transformations leading to removal of the native oxides of III-V substrates. As outlined in section 5.1, we propose that the main and most thermodynamically stable product of these transformations is a film of dielectric metal oxide with the general formula  $M_2O_n$ . (Thus, there is no reduction or oxidation of  $M$ ). Another factor in the successful clean-up performance is affinity of the precursor ligand  $L$  to the III-V oxide substrate. We can describe formation of one O- $M$  bond and subsequent transformations of

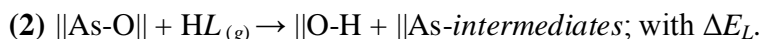
the ligand on the sample III-V oxide surface (*i.e.* a clean-up process) with the following equation:



where || stands for surface bound intermediates and *g* for gas-phase molecules.

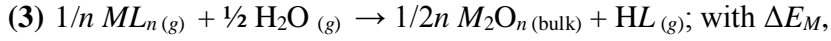
In the above equation we assume that the formed metal oxide is stoichiometric: upon increasing the coordination number of the metal centre to the native oxide oxygen, the coordination to the ligands decreases and ligands are released to interact with the substrate. The equation also shows that *M*-O formation and interaction of ligands with As can be viewed as separate events, to a first approximation.

Identification of these separate factors allows for an efficient description of interactions of the surface intermediates that are formed as a result of ligand decomposition, and of associated chemical processes that lead to formation of the clean-up products. Computing the intermediates from just one ligand should be computationally less expensive and easier to understand than computing the decomposition of the entire precursor molecule. Therefore, in this chapter we take advantage of this methodology and reduce equation (1) to a description of chemical processes associated only with the interaction of one ligand with the substrate independent of *M*, as per the reaction:

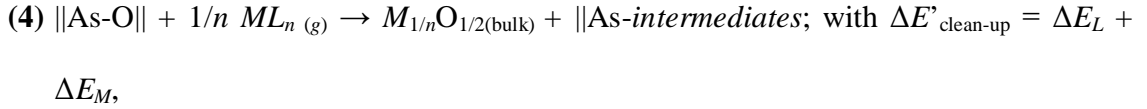


A proton is included to ensure overall charge neutrality and so on the right hand side of the reaction a hydroxyl group ||O-H is formed. The formation of one *M*-O bond in equation (1) can then be described by the model reaction for various *M*:

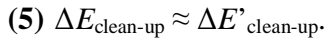




which is the overall ALD reaction. Combination of the ligand reaction (2) and the metal-dependent correction (3) gives essentially reaction (1):



but at much lower computational effort. Therefore:



Nevertheless, we note that explicit simulation of the whole precursor molecule according to equation (1) cannot be avoided for a proper description of some types of chemical processes and is the subject of chapter 6 in which we consider alkylamide precursor.

The technical details of the DFT method and *ab initio* thermodynamics described in section 2.2 apply to this chapter. We use a 2×2 surface expansion of (010)-*arsenolite* that contains 1 layer totaling 8 molecular units of As<sub>4</sub>O<sub>6</sub> (80 atoms) and a 2×2×1 *k*-point mesh for surface calculations. Additionally, to study the stability of surface intermediates we performed DFT molecular dynamics in the canonical ensemble at around 300° C for 0.4 ps. At the end of these simulations all surface intermediates were found to be bonded the same as their initial configuration, suggesting that no spontaneous reactions occur and that there are barriers to overcome on the potential energy surface for any following chemical transformations.

In section 5.3 thermodynamic energies are presented for formation of metal oxides from gas phase precursors determined using DFT,  $\Delta E_M$  (equation (3)). In the subsequent

sections different types of intermediates that are formed during clean-up as a result of decomposition of selected precursors are examined and their structures are illustrated in **Figure 5-2**. Types of reactions included are: dissociation of the precursor through scission of the  $M-L$  bond in section 5.4, decomposition of the dma ligand through scission of the C-H and N-C bonds in section 5.5 and multiple decomposition steps combining these elementary steps described in section 5.6. Energetics for the interaction of ligands with the substrate,  $\Delta E_L$ , is given in **Table 5-1**. The effectiveness of different metal precursors in performing clean-up of III-V oxides is evaluated by correcting  $\Delta E_L$  with  $\Delta E_M$  (also **Table 5-1**).  $\Delta E_M$  and  $\Delta E_L$  along with overall  $\Delta E'_{\text{clean-up}}$  are summarized in **Figure 5-1** and **Figure 5-3**. A reaction scheme considered for the decomposition of the dma ligand is illustrated in **Figure 5-4**. A series of proposed elementary steps can give rise to desorption of multiple clean-up products. Based on the thermodynamic accessibility of these elementary surface steps and some kinetic indications, we discuss in each section which clean-up mechanism and associated by-product is competitive in the ALD process. Because of limitations of our current model, we cannot generally compute the complete energetics for each mechanism here. As we focus in this study on the decomposition of the ligand, our model naturally does not cover molecular or dissociative adsorption of the precursor and associated steric effects. These are the subject of future work.

### 5.3 Formation of metal oxides from gas phase precursors

Reaction (3) contains information about the reactivity of precursors towards formation of bulk oxide and bonding changes upon elimination of ligands as HL. Computed energetics for a selection of metals and ligands are summarized and illustrated in Figure 5-1. Values for reaction (3) can be found in Table 5-1 under  $\Delta E'_{\text{clean-up}}$  for  $\Delta E_L = 0$  eV (see equations (3) and (4)).

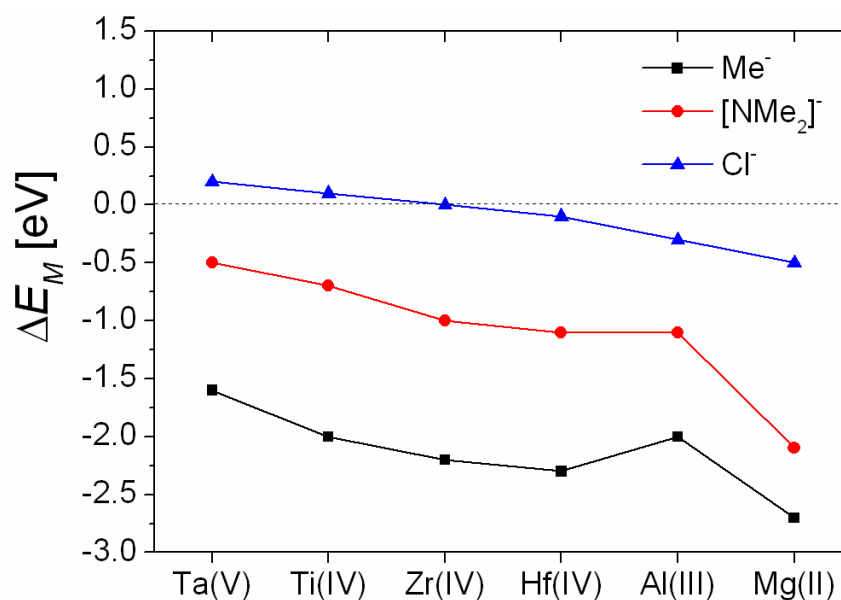


Figure 5-1 Computed energetics,  $\Delta E_M$ , for formation of metal oxides from gas phase precursors  $ML_n$  (x axis:  $M = \text{Mg(II)}, \text{Al(III)}, \text{Ti(IV)}, \text{Zr(IV)}, \text{Hf(IV)}, \text{Ta(V)}$ ;  $L = [\text{N}(\text{Me})_2]^-$ ,  $[\text{Me}]^-$ ,  $[\text{Cl}]^-$ ;  $n$  – oxidation state of metal) and water according to:  $1/n ML_n(g) + 1/2 H_2O(g) \rightarrow 1/2n M_2O_n(\text{bulk}) + HL(g)$  (equation (3)). Lines are to guide the eye.

L	products at surface:	$\Delta E_L$	$\Delta E'$ clean-up for M:					
			Ta	Ti	Zr	Hf	Al	Mg
[N(Me) <sub>2</sub> ] <sup>-</sup>	As – O   + HNMe <sub>2(g)</sub>	0.0	-0.5	-0.7	-1.0	-1.1	-1.1	-2.1
	<b>A</b>   O – H +   As – NMe <sub>2</sub>	+0.1	-0.4	-0.6	-0.9	-1.0	-1.0	-2.0
	<b>B</b> 2  O – H +   As – N(Me)CH <sub>2</sub> – As	+0.6	+0.1	-0.1	-0.4	-0.5	-0.5	-1.5
	<b>C</b> 2  O – H +   As – N(Me)CH <sub>2</sub> – O   + 2e <sup>-</sup>	+1.3	+0.8	+0.6	+0.3	+0.2	+0.2	-0.8
	<b>D</b>   O – H +   As – N(Me)CH <sub>2</sub> – As   +   As – H - 2e <sup>-</sup>	+2.1	+1.6	+1.4	+1.1	+1.0	+1.0	0.0
	<b>E</b>   O – H +   As – N(Me)CH <sub>2</sub> – O   +   As – H	+1.2	+0.7	+0.5	+0.2	0.1	0.1	-0.9
	<b>F</b>   O – H +   As = NMe +   O – Me	+1.5	+1.0	+0.8	+0.5	+0.4	+0.4	-0.6
	<b>G</b>   O – H +   As = NMe +   As – Me - 2e <sup>-</sup>	+1.6	+1.1	+0.9	+0.6	+0.5	+0.5	-0.5
	<b>H</b> 3  O – H +   As – N(CH <sub>2</sub> – As  ) <sub>2</sub>	+1.3	+0.8	+0.6	+0.3	+0.2	+0.2	-0.8
	<b>I</b> 4  O – H +   As = NCH=CH <sub>2</sub> + 2e <sup>-</sup>	+2.2	+1.7	+1.5	+1.2	+1.1	+1.1	+0.1
	<b>J</b> 2  O – H +   As – N=CH <sub>2</sub> +   As – Me	+0.9	+0.4	+0.2	-0.1	-0.2	-0.2	-1.2
<b>K</b> 3  O – H +   As – N=CH – As   +   As – Me	+1.9	+1.4	+1.2	+0.9	+0.8	+0.8	-0.2	
[Me] <sup>-</sup>	As – O   + CH <sub>4(g)</sub>	0.0	-1.6	-2.0	-2.2	-2.3	-2.0	-2.7
	<b>A'</b>   O – H +   As – Me	+0.7	-0.9	-1.3	-1.5	-1.6	-1.3	-2.0
[Cl] <sup>-</sup>	As – O   + HCl <sub>(g)</sub>	0.0	+0.2	+0.1	0.0	-0.1	-0.3	-0.5
	<b>A''</b>   O – H +   As – Cl	-0.3	-0.1	-0.2	-0.3	-0.4	-0.6	-0.9

Table 5-1 List of possible clean-up intermediates: A-K, A' and A'' that are formed during ALD III-V substrate exposure to various metal precursors. Energies are in eV relative to ||As – O|| + HL<sub>(g)</sub> as per reaction (2) with L = [N(Me)<sub>2</sub>]<sup>-</sup>, Me<sup>-</sup>, Cl<sup>-</sup>. The effect of different M = Ta, Ti, Zr, Hf, Al, Mg is included by adding the correction  $\Delta E_M$  obtained from reaction (3) (see section 5.2 for details).

The energetics indicate that the most reactive precursor family for formation of metal oxides and elimination of HL are metal methyls. The most reactive of the six considered is MgMe<sub>2</sub> with  $\Delta E_M = -2.7$  eV per methyl ligand. The least reactive among the hypothetical methyl precursors is TaMe<sub>5</sub> with  $\Delta E_M = -1.6$  eV per Me for formation of Ta<sub>2</sub>O<sub>5</sub>. AlMe<sub>3</sub> with  $\Delta E_M = -2.0$  eV per Me presents similar reactivity to TiMe<sub>4</sub>, not to HfMe<sub>4</sub> or ZrMe<sub>4</sub>. Al, Hf and Zr alkylamides with  $\Delta E_M \approx -1.0$  eV per ligand have similar reactivity and the Ta and Ti alkylamides are slightly less reactive. The most reactive for

formation of oxide among metal alkylamides is  $\text{Mg}[\text{N}(\text{CH}_3)_2]_2$  with  $\Delta E_M = -2.1$  eV per alkylamide ligand. According to our computations the smallest driving force for formation of  $M_2O_n$  is shown by chloride precursors.  $\Delta E_M$  for  $L = \text{Cl}^-$  ranges from -0.5 eV per Cl for Mg to +0.2 eV per Cl for Ta. These trends are consistent with previous calculations [132, 133].

#### 5.4 Dissociation of ligand by M-L scission

By calculating DFT energies for dissociation of the ligand from the metal center, we investigate the affinity of the ligand to the oxide to be cleaned-up. This gives us  $\Delta E'_{\text{clean-up}}$  for the elementary step that leads to a ligand exchange mechanism. The elementary steps that we have considered involve the transfer of a dimethylamide, methyl and chloride group to the surface As atom in structures A, A' and A'' respectively, shown in [Figure 5-2](#). Energetics for formation of intermediates A show that the alkylamide ligand can readily dissociate from the  $M$  center to the available As site and form a thermodynamically stable product  $\|\text{As} - \text{N}(\text{CH}_3)_2$  plus oxide of  $M$  (see [Table 5-1](#) and [Figure 5-3](#) for energetics). According to reaction (2) and correction for the  $M$ -O bond formation, reaction (3), this ligand transfer process is exothermic for all considered metals. The energy for this reaction ranges from -0.4 eV per ligand for  $\text{Ta}[\text{N}(\text{CH}_3)_2]_5$  to -2.0 eV for  $\text{Mg}[\text{N}(\text{CH}_3)_2]_2$ . If this reaction is not hampered by a high kinetic barrier, it will proceed until the surface is saturated with  $\|\text{As} - \text{N}(\text{CH}_3)_2$  species.

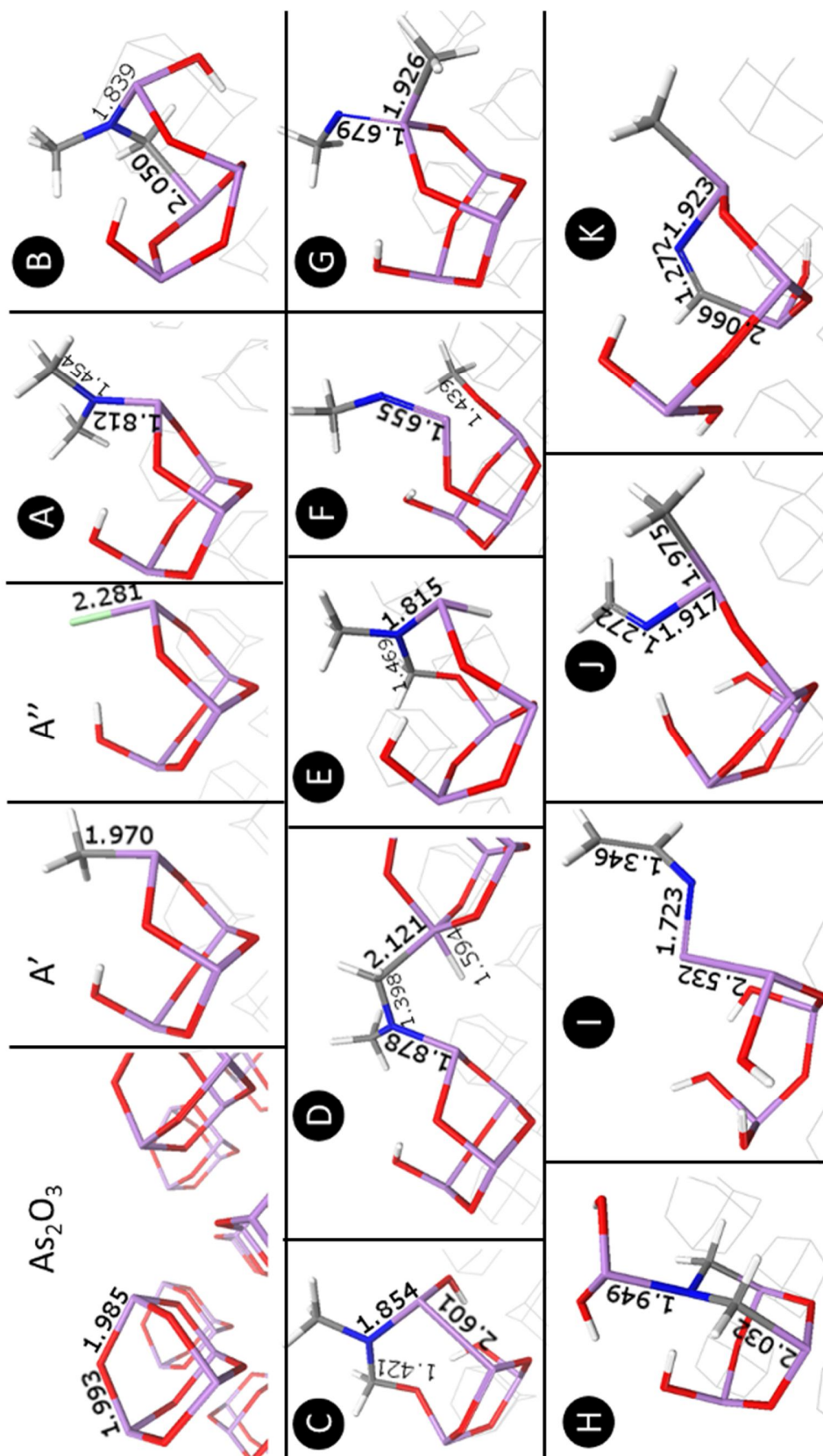


Figure 5-2 Surface models for  $As_2O_3$  and decomposition species of metal methyls, A', metal chlorides, A'', and metal alkylamides, A-K. Stick representation: purple As, red O, white H, gray C, green Cl, blue N. Selected bond lengths are given in Å. Thin lines show adjacent substrate atoms.

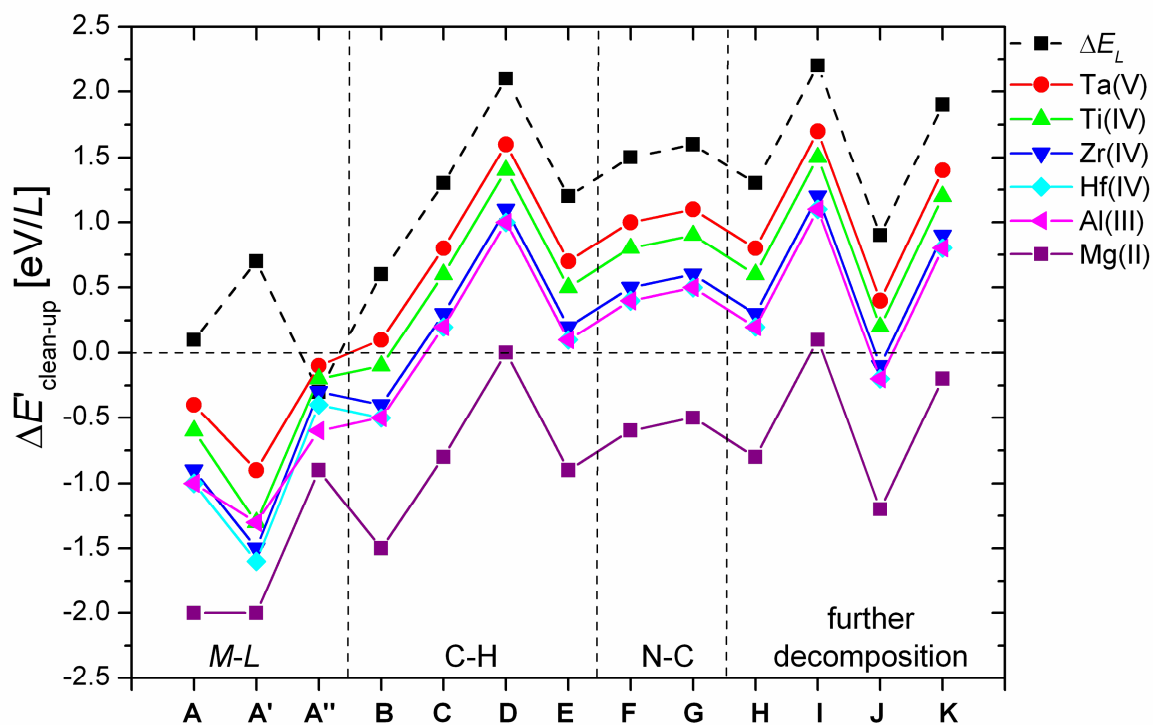


Figure 5-3 Computed energetics for surface intermediates, *intermediates* A-K, which are formed during clean-up of  $\text{As}_2\text{O}_3$ . As listed in Table 5-1, A, A' and A'' are surface products of precursor decomposition through scission of  $M-L$  bond ( $M = \text{Mg(II)}$ ,  $\text{Al(III)}$ ,  $\text{Ti(IV)}$ ,  $\text{Zr(IV)}$ ,  $\text{Hf(IV)}$ ,  $\text{Ta(V)}$ ) for  $L = [\text{N}(\text{Me})_2]$ ,  $[\text{Me}]$ ,  $[\text{Cl}]$  respectively; B-E are surface products of decomposition of  $[\text{N}(\text{Me})_2]$  through scission of C-H bond; F and G surface products of decomposition of  $[\text{N}(\text{Me})_2]$  through scission of N-C bond; H-K are surface products when further decomposition occurs through scission of both C-H and N-C bonds.  $\Delta E_L$  (equation (2)) describes interaction of the ligand  $L$  with the  $\text{As}_2\text{O}_3$  substrate (black data points). It is subsequently corrected with  $\Delta E_M$  (equation (3)) and gives overall  $\Delta E'_{\text{clean-up}}$  for various  $M$  (equation (4)). Lines are to guide the eye and do not imply a reaction sequence (see instead Figure 5-4).

Energetics show that the methyl ligand is very reactive towards the arsenic oxide substrate and more reactive than alkylamide (A' Figure 5-3). The energy ranges from -0.9 eV for  $\text{Ta}(\text{CH}_3)_5$  to -2.0 eV for  $\text{Mg}(\text{CH}_3)_2$ . The energy for exchange of a  $\text{Cl}^-$  ligand between the precursor metal center and the native oxide, with product A'' in Figure 5-2, ranges from -0.1 eV for  $\text{TaCl}_5$  to -0.9 eV for  $\text{MgCl}_2$ , indicating that it is less thermodynamically favored than for alkylamides and methyls.

Sufficient concentration of these  $\text{As} - L$  groups may lead to formation of  $\text{AsL}_3$ : tris(dimethylamino)arsine, TDMAAs,  $\text{As}[\text{N}(\text{CH}_3)_2]_3$ ; trimethylarsine,  $\text{As}(\text{CH}_3)_3$  and arsenic trichloride  $\text{AsCl}_3$ , as volatile products in processes utilizing alkylamides, methyl

and chloride precursors respectively. Desorption of these molecules means that  $\text{As}_2\text{O}_3$  has been transformed into  $M_2\text{O}_n$ , *i.e.* clean-up. Indeed, this ligand transfer mechanism has been proposed by others [11, 56]. Experimental study clearly shows enhancement of the clean-up process with increasing temperature when metal alkylamides are used [60, 66]. If there are significant kinetic requirements for the ligand exchange reaction, they may originate from steric effects. There was evidence for this in our previous study for TMA, where we showed that the rate limiting step for the ligand transfer process could be crowding of methyl ligands at one surface site [114]. We suspect that this process can be even more difficult for the bulkier alkylamides. Thus, steric effects may have a pronounced influence on the kinetics of ligand transfer to TDMAAs, which may stop this reaction before going to completion, and promote ligand decomposition instead. In fact, TDMAAs is known to thermally decompose on the GaAs surface [134-136]. Therefore, it is reasonable to suspect that the alkylamide can decompose, or partially decompose, in contact with the native oxide surface, and give rise to other clean-up products rather than form TDMAAs. Ligand decomposition is investigated in subsequent sections.

In the case of chlorides, although they are successfully used in ALD of different metal oxides, there is no agreement in the literature about their interfacial self-cleaning abilities [9, 57, 58]. Our study shows that chloride chemistry is different. The main driving force that we have postulated, namely formation of the metal oxide dielectric during clean-up, does not seem to be adequate for clean-up with these chemicals:  $\Delta E_M \geq 0$ . Most of the metal chlorides are weak Lewis acids. Their electrophilic characteristic allows them to form Lewis adducts like  $\text{TaOCl}_3$ , complexes like  $[\text{TiCl}_6]^{2-}$  or even hydrates, *e.g.*  $\text{MgCl}_2(\text{H}_2\text{O})_x$  [137]. Formation of oxychlorides, *e.g.*  $\text{TiOCl}_2$ , or even hydroxychlorides,  $\text{TiCl}_3\text{OH}$ , during clean-up with  $\text{TiCl}_4$  for  $\text{TiO}_2$  deposition, could explain observed removal of O and surface passivation with Cl [58]. As proposed before, clean-up with this ligand can be accounted for *via* an agglomeration reaction mechanism [57].



Ligand affinity for Ga and In is discussed in section 5.7.

## 5.5 Decomposition of dma ligand

For the following consideration of decomposition processes of alkylamide ligand on the example of dimethylamide we use the highly stable product A  $\text{||As} - \text{N}(\text{CH}_3)_2$ , as a starting species for further clean-up transformations B-K. Decomposition of the alkylamide ligand is possible *via* activation of a C-H bond, releasing anionic or cationic H, or of an N-C bond, releasing anionic or cationic  $\text{CH}_3$  as schematically shown in [Figure 5-4](#). In this section we examine mechanistic paths for these H and  $\text{CH}_3$  moieties to attack As and O sites. We consider all possible reactions and highlight redox processes that may enhance the clean-up effect.

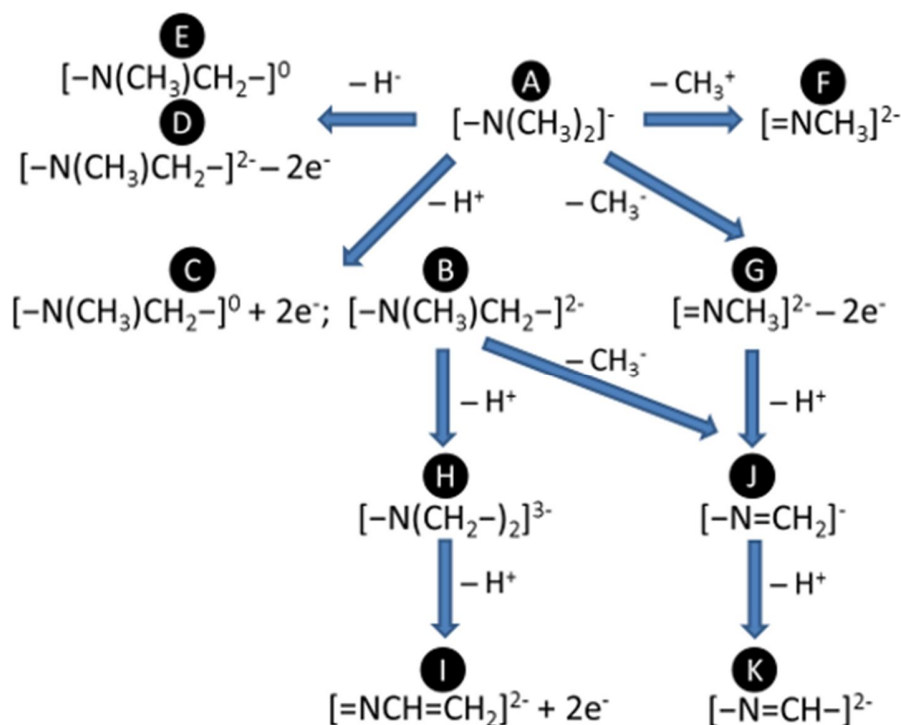


**Figure 5-4** Reaction scheme for decomposition of dimethylamido ligand  $[-\text{N}(\text{CH}_3)_2]^-$  on metal oxide surfaces (species A-K). Notation: ‘ $-\text{H}^{+/ -}$ ’ means dissociation of proton/hydride from ligand to the surface; ‘ $-\text{Me}^{+/-}$ ’ means dissociation of methyl/methanide group from ligand to the surface; ‘ $+2e^-$ ’ means oxidation of ligand by surface (reduction of surface by ligand); ‘ $-2e^-$ ’ means reduction of ligand by surface (oxidation of surface by ligand).

### 5.5.1 C-H scission and H elimination (B-E)

The C-H bond of the ligand is weakened by the electron density of the lone pair of electrons on the neighboring N atom, so that H  $\alpha$  to the N atom can dissociate and bond to an available surface site. First we investigate scission of the C-H bond and formation of an O-H bond in the intermediates B shown in [Figure 5-2](#). Our calculations show that upon the proton ( $H^+$ ) transfer from a ligand to a surface O atom, the As-O bond is broken. The electronic density around the C atom in the remaining methylene ( $CH_2$ ) moiety of the ligand increases by  $\Delta q = +1.5e$ . This Lewis basic C atom can interact with the surface As cation that lost coordination to the O atom. The bond formed between the As atom and the C atom is 2.0 Å long which is typical of single As-C bond. As a result a N-methylmethylenimido ion ( $[-N(Me)CH_2]^{-2}$ ) is attached to the surface. Our attempts to find a competitive minimum for the N-methylmethylenimido ligand with tricoordinated N atom featuring a N=C double bond (*i.e.*  $[-N(Me)=CH_2]^-$ ) were not successful. The thermodynamically stable state preserves tricoordinated N and tetrahedral C. This process is the most exothermic out of the decomposition processes with a calculated  $\Delta E'_{\text{clean-up}}$  ranging from +0.1 eV for  $Ta[N(CH_3)_2]_5$  to -1.5 eV for  $Mg[N(CH_3)_2]_2$  ([Table 5-1](#)).

We also examine the redox process mediated by ligand attack of the  $CH_2$  moiety onto the O site, instead of the As site, to form product C ([Figure 5-2](#)). This is analogous to the migration of  $CH_3$  from As to O that we observed to be responsible for clean-up with TMA [131]. In this elementary step two As-O bonds are broken, promoting formation of the O-H (1.0 Å) bond and the O-C bond (1.4 Å). Two electron-deficient surface metal cations are forced to interact and as a result a metallic As-As dimer is formed along with the intermediates  $\parallel As - NCH_3CH_2 - O \parallel$ . Electrons are transferred to surface arsenic (+1.0e and +1.1e on the dimer atoms) from the C atom of  $CH_2$  (-1.6e) but also from N (-0.5e), elongating the N-As bond by around 2% as compared to structure A. Decomposition of the alkylamide *via* this process is thus reducing the As oxide surface

and contributing to clean-up. This oxidation of the C atom is endothermic for most of the precursors: tantalum, titanium, zirconium amides (+0.8, +0.6, +0.3 eV respectively), almost neutral for hafnium amide (+0.1 eV) and exothermic for magnesium amide (-0.8 eV) according to equations (2) + (3) ( $\Delta E'_{\text{clean-up}}$ , Table 5-1). It is less favorable than formation of the As-C bond in the structure B described above.

For completeness we studied scission of the C-H bond and the transfer of H to an As site. This process essentially involves hydride (H<sup>-</sup>) dissociation from the alkylamide ligand and formation of products D and E with structures illustrated in Figure 5-2. In the intermediates D two new bonds are created: As-H and As-C, increasing the coordination number of the As atom from three to five. Formation of these two bonds is expected to cause the withdrawal of the electronic density from the oxide substrate and so its local oxidation (see scheme in Figure 5-4). Charge analysis suggests a decrease in electronic populations by only -1.0e on the oxidised pentacoordinated As and an increase of +1.0e on the H atom bonded to this arsenic. The absence of charge transfer between this arsenic and CH<sub>2</sub> suggests some charge retraction that is explained as follows. The CH<sub>2</sub> moiety of the created surface product ||As – N(Me)CH<sub>2</sub> – As|| becomes more Lewis acidic (-0.4e on the C atom) and the N atom more Lewis basic (+0.5e), attracting each other (4% shorter N-CH<sub>2</sub> bond, relative to the same bond in B) and repelling bonded arsenic atoms (both: As-N and As-CH<sub>2</sub> bonds are elongated by 4%, relative to the same bonds in B or C). This indicates that desorption of the N-methylmethylenimido ligand as neutral Me–N=CH<sub>2</sub> should be preferred over formation of the dianion ([–N(Me)CH<sub>2</sub>–]<sup>2-</sup> and substrate oxidation. The oxidation of As upon hydride dissociation is not favorable. In fact this is one of the least favorable processes that we have computed with energy ranging from +1.6 eV to +1.0 eV for almost all of the precursors and energetically neutral only for Mg[N(CH<sub>3</sub>)<sub>2</sub>]<sub>2</sub>. We observe that no As-O bond is broken in this elementary process, *i.e.* it does not contribute to clean-up.

Our results indicate that energy for hydride dissociation can be lowered by 0.9 eV when this process is accompanied by oxidation of the C atom and formation of the surface product E:  $\parallel\text{As} - \text{NCH}_3\text{CH}_2 - \text{O}\parallel + \parallel\text{As} - \text{H}$ . In this case As-H and O-C bonds are formed breaking one As-O bond (see [Figure 5-2](#)). We note that electronic densities are withdrawn from the O-CH<sub>2</sub>-N entity (-1.0e) by the newly-formed hydride (+1.0e) and there is no charge transfer to the substrate. The attack of CH<sub>2</sub> onto the O site and transfer of H<sup>-</sup> to the As site is slightly endothermic for most of the precursors (+0.7 to +0.1 eV) and exothermic for the magnesium precursor (-0.9 eV).

DFT calculations show that decomposition of alkylamide ligand through scission of the C-H bond  $\alpha$  to N is thermodynamically feasible. This pathway is often referred to in the literature as  $\beta$ -H elimination. Most likely this process will result in hydroxylation of the native oxides and formation of C-As(Ga, In) bonds (B). A possible volatile product of this clean-up transformation is N-methyl methyleneimine (MMI). Desorption of imine in the considered system requires reorganization in the electronic density with the formation of an N=C double bond and cleavage of As-N and As-C bonds, which is speculated to be kinetically demanding. Simultaneously, charge transfer to the surface As should occur resulting in formation of metallic As-As bonds. We calculate that desorption of imine according to the reaction:  $\parallel\text{As} - \text{NCH}_3\text{CH}_2 - \text{As}\parallel \rightarrow \parallel\text{As-As}\parallel + \text{CH}_3\text{NCH}_2(g)$  costs +0.7 eV relative to formation of B. This suggests that the clean-up reactions producing imine need temperature activation.

The weakening effect of the N-lone pair on the C-H bonds in the  $\alpha$  position has been observed in vibrational spectroscopy, where an unusually low frequency of vibration of the C-H mode in TDMAH has been reported [138]. It has been reported that the C-H dissociation is possible already upon adsorption of alkylamide precursors onto silicon substrates at very low temperature of 220 K [139, 140]. As mentioned in the previous section MMI is a detected product of etching GaAs surface by TDMAAs [134]. Several

reports can be found where metal alkylamides are shown to decompose to produce imine and amine [141, 142]. We show here that H elimination can occur from a ligand that has migrated to the native oxide surface ( $A \rightarrow B$ ). Product B can then undergo other transformations  $B \rightarrow H-K$ , leading to different clean-up products as described later, or desorption of imine can occur. Either process leads to arsenic oxide removal and/or reduction to metallic arsenic, and so may contribute to the clean-up effect.

Another clean-up product that can arise from H elimination in the structures D and E is arsine,  $AsH_3$ . However, the unfavourable energetics computed by DFT for elementary steps leading to surface functionalization with  $||As - H$  groups suggests that formation of arsine from intermediates D or E is a minor clean-up channel.

### 5.5.2 N-C scission (F-G)

We next examined possible pathways for  $CH_3$  dissociation resulting with products F and G (for pathways see [Figure 5-4](#), for structures of products [Figure 5-2](#)). First we considered activation of the N-C bond in the presence of the available Lewis basic O site of the substrate (F). As the  $CH_3$  group coordinated to the N atom in the alkylamide ligand has Lewis acidic character (formally  $CH_3^+$ , methylium cation), we expect no redox during transfer to the substrate in this step. Upon this transfer the As-O bond is broken, promoting formation of a double bond between the As and N atoms (1.7 Å). Our results indicate that the reaction along this pathway is moderately endothermic with a thermodynamic energy of +1.0 to +0.4 eV for Ta, Ti, Zr, Hf, Al precursors and exothermic by -0.6 eV for the Mg precursor ( $\Delta E^{\text{clean-up}}$ , [Table 5-1](#)).

Another possibility is for the  $CH_3$  moiety to attack an As surface site (G). The DFT calculations show that, similarly, an  $As=N$  double bond is formed, but As-O bonds are not affected. We observe oxidation of the As atom (-1.9e), which is now pentacoordinated, and reduction of the C atom of the dissociated  $CH_3$  moiety (+1.9e),

consistent with transfer as  $\text{CH}_3^-$  (methanide anion). This elementary step is therefore the reverse of clean-up. The bond formed between the C atom and the As atom is 1.9 Å long. This decomposition structure is a little more unstable than F with respect to reactants, at a calculated energy difference of +0.1 eV relative to the energy for formation of product F. Pathways involving dissociation of the methyl group lead to functionalization of the surface with  $\text{||O} - \text{CH}_3$  (F) or formation of the  $\text{||As} - \text{CH}_3$  groups (G) along with the  $\text{||As} = \text{NCH}_3$  fragment. This can thus lead to desorption of gaseous dimethyl ether,  $\text{O}(\text{CH}_3)_2$ , or trimethylarsine,  $\text{As}(\text{CH}_3)_3$ . Additionally, if a source of protons is present, methane  $\text{CH}_4$  can be formed from  $\text{||As} - \text{CH}_3$ . However, our calculations show that elementary steps for F and G formation that could give dimethyl ether or trimethylarsine as clean-up products are less competitive when compared to the elementary steps leading to formation of TDMAAs or MMI (A or B, see [Table 5-1](#)). During ALD of metal oxide films, protons can derive from the  $\text{H}_2\text{O}$  pulse, but are supposedly eliminated in reaction with alkylamide ligands to produce amine, the main ALD product.  $\text{||O-H}$  groups are also formed during the H elimination process investigated above. We will see later that the sequence of production of B and G intermediates is competitive and can directly lead to methane production.

## 5.6 Further decomposition of dma ligand

### 5.6.1 Multiple redox steps – dehydrogenation H-I

Based on the results shown above, we assume that the main reaction channel for the elimination of H atoms from alkylamide ligands on the oxide substrate is formation of the surface hydroxide and carbon-arsenic bound intermediates as in product B. In this section we investigate the most stable products of successive dehydrogenation of the alkylamide ligand.

The stability of the surface intermediate H decreases by about 0.7 eV relative to B after a second proton transfer. The electronic density increases on both C atoms (+1.2e and +1.3e) and a total of two protons are transferred to the oxide surface. There are now two CH<sub>2</sub> entities that form bonds with acidic As atoms through basic C atoms. A loss of electronic density on N of -0.5e is observed in Bader analysis. This affects the As-N bond, which is weakened (about 8% longer than the As-N bond in product B) suggesting that the  $\pi$  character of this bond decreases. The lone pair of electrons on N is no longer stabilized and N becomes nearly pyramidal in this structure (see [Figure 5-2](#)). This process requires energy and so it is clear that it requires some thermal activation.

Further dehydrogenation is possible *via* carbon disproportionation yielding a methylidyne fragment (HC) that inserts into the C-N bond in the intermediates I. The surface product features a double bond between As and N (1.7 Å) that is now bound to a vinyl moiety CH=CH<sub>2</sub> (C=C bond length: 1.3 Å). Three hydroxide groups and an As-As dimer with the bond length of 2.5 Å are formed at the expense of four As-O bonds. Bader analysis confirms reduction of the dimer As atoms (+1.1e and +1.4e for the As atoms bound to N) which means that this reaction contributes to clean-up. We also observe disproportionation of charge between C atoms (increase of electronic population on methylene group of +0.6e and decrease on methylidyne group of -0.3e relative to populations on methyl groups in amide ligand in structure A). We note some charge transfer to the N atom of +0.5e. Formation of an  $[=NCH=CH_2]^{2-}$  adsorbate is the most endothermic of the considered processes (+1.6 eV relative to B formation).

Our computations thus show that successive dehydrogenation becomes progressively less favored. It may result in the formation of the following volatile products: imine from species B as mentioned above; aziridine, HN(CH<sub>2</sub>)<sub>2</sub>, from H; ethylene, C<sub>2</sub>H<sub>4</sub>, and subsequently molecular nitrogen, N<sub>2</sub>, from I. The energetics for pathways leading to desorption of these species suggest that this is only possible through thermal activation –

moderate temperatures for imine formation and high temperatures for desorption of molecular nitrogen.

Aziridine may be produced from structure H by a reaction of cleaving As-C bonds, forming a C-C bond (for this process we calculate +0.5 eV relative to formation of H), subsequent coupling with adjacent protons if available and desorption, all of which has a DFT energy of just +0.3 eV relative to H. This contributes to clean-up, leaving the surface with metallic As-As bonds according to:  $\|As - N(CH_2 - As)\|_2 + \|O - H \rightarrow \|As - O\| + \|As - As\| + HN(CH_2)_2 (g)$ . The rate limiting step may be breaking As-C and forming a three membered C-C-N ring. Aziridine is one of the stable products detected in the *in situ* mass spectroscopy experiment of thermal decomposition of TDMAAs below 450°C [142].

C<sub>2</sub>H<sub>4</sub> was detected as a desorption product originating from secondary surface reactions when a tantalum surface was exposed to Ta[N(CH<sub>3</sub>)<sub>2</sub>]<sub>5</sub> at 550 K [143]. One of the proposed mechanisms envisages dehydrogenation of methyleneimido intermediates, insertion of a methylidyne moiety into the carbon-nitrogen bond and subsequent hydrogenation of the vinyl fragment to produce ethylene and leave an adsorbed N atom [143]. We suggest that, on the reducible arsenic oxide substrate following coupling of adsorbed N atoms to form N<sub>2</sub> could be possible at highly elevated temperatures, which would result in clean-up according to:  $2 \|As = NCH=CH_2 + 2 \|O - H \rightarrow \|As - As\| + 2 C_2H_4 (g) + N_2 (g)$ .

### 5.6.2 Multiple redox steps J-K

In this section we study sequences of CH<sub>3</sub> dissociation and alkylamide dehydrogenation reactions that give rise to new clean-up products. Assuming, as previously, that the most probable pathway for alkylamide dehydrogenation is arsenic oxide hydroxylation, we can consider pathways where the CH<sub>3</sub> group formally dissociates either as the methylium



cation or as the methanide anion (as the above investigation of processes producing F and G revealed a competition between them). Here we show the most stable products of these reactions. All other possible reactions can be found in the supplementary information.

Our investigations suggest that the more stable products are those formed during reactions that do not involve charge transfer to the oxide substrate. For instance, dehydrogenation of the alkylamide ligand followed by dissociation of the methanide anion in structure J (Figure 5-1) is preferred over dissociation of the methylum cation that combined with proton dissociation results in substrate reduction:  $[-N(CH_3)_2]^- \rightarrow [-N=CH_2]^- + [CH_3]^+ + [H]^+ + 2e^-$  (not showed in Figure 5-1). The step leading to product J is among the few steps that we find to be exothermic or neutral at 0 K for most of the regarded precursors (Table 5-1). The reorganized electron density in the proton dissociation process (see section 5.5.1 for description of the proton elimination process in structure B) can be attracted by a  $CH_3$  group instead of a  $CH_2$  group. Bader analysis shows an increase in the electronic populations on the C atom of  $CH_3$  ( $+1.9e$ ) and decrease on the C atom belonging to the methylene moiety ( $-1.2e$ ). The acidic methylene forms a double bond with the N atom ( $1.3 \text{ \AA}$ ), instead of bonding to surface cation like in structure B. The basic methanide bonds with the As atom ( $2.0 \text{ \AA}$ ). We note some increase of electronic density on the N atom that is now even more basic ( $+0.5e$ ) than in the original alkylamide ligand in structure A.

Proton dissociation accompanied by the formation of the methanide anion could be a low temperature channel for the formation of  $CH_4$ . According to our computations formation of methane from surface intermediate J is slightly exothermic with energy  $-0.1 \text{ eV}$  (neglecting entropy).  $CH_4$  was observed in some studies as a product of decomposition of the amido ligands. Infrared (IR) spectroscopy and temperature-programmed desorption (TPD) investigations of  $Ti[N(CH_3)_2]_4$  on a Si substrate showed that methane desorbs at temperatures below 400 K [140]. In the same study DFT

calculations suggest that facile generation of methane right above room temperature is due to the surface activation of C – H and C – N bonds of amido ligand. In the thermal chemistry investigation of Ta[N(CH<sub>3</sub>)<sub>2</sub>]<sub>5</sub> CH<sub>4</sub> is a decomposition product detected throughout the studied temperature range up to 600 K [143]. Our DFT results suggest that scission of the N-C bond is triggered by the H elimination process on the oxide substrate and thermodynamically is not as demanding as other decomposition processes. Although formation of methane is plausible, desorption of this chemical alone from the oxidised III-V system does not directly result in self-cleaning. In this pathway methane is formed according to: ||As – Me + ||O – H → ||As – O|| + CH<sub>4</sub>, so arsenic oxygen bonds are formed. However, other products can arise as a consequence of saturation of the native oxide surface with [–N=CH<sub>2</sub>]<sup>–</sup> groups after CH<sub>4</sub> desorption in species J: C<sub>2</sub>H<sub>4</sub> and subsequently N<sub>2</sub>. Eventual desorption of CH<sub>4</sub>, C<sub>2</sub>H<sub>4</sub> and N<sub>2</sub> would finally lead to clean-up resulting in reduction of arsenic oxide to metallic arsenic, but involving multiple redox steps: 2 ||As – N=CH<sub>2</sub> → ||As – As|| + C<sub>2</sub>H<sub>4</sub> (g) + N<sub>2</sub> (g). This process requires energy to break the double bond between N and C atoms, combining two CH<sub>2</sub> groups and two N moieties on the surface. As remarked in our discussion of possible products arising from intermediates I, processes involving multiple redox steps are presumably possible at highly elevated temperatures.

Further dehydrogenation of the methylene group in the [–N=CH<sub>2</sub>]<sup>–</sup> adsorbate described above, yields a methyldiyne (CH<sup>+</sup>) ion in surface product K. This is less favored by +1.0 eV relative to previous process J (see [Table 5-1](#)). Proton dissociation to another O site renews C basicity (+1.0e with respect to the [–N=CH<sub>2</sub>]<sup>–</sup> adsorbate) that now can attack another As site. The [–N=CH–]<sup>2–</sup> ion is bound to surface arsenic atoms through N and C, forming bonds 1.9 Å and 2.0 Å long respectively (K [Figure 5-1](#)). Generation of the [–N=CH–]<sup>2–</sup> surface intermediate can directly lead to desorption of hydrogen cyanide, HCN, another clean-up product: ||As – N=CH – As|| → ||As – As|| + HCN (g). HCN was

detected to desorb at 600 K during tantalum alkylamide exposure to a tantalum substrate [143].

## 5.7 Effect of substrate on clean-up

Our model supposes that clean-up can be achieved by successive dissociation of ligands from the absorbed precursor. One can expect that the  $M - L$  bond can be easily activated on the oxide surface when the substrate metal oxide is less stable than the deposited metal oxide  $M_2O_n$ . The metal center of the precursor then becomes chemically active towards penetrating the III-V oxide substrate and scavenging the oxygen. A similar technique is used for equivalent-oxide-thickness scaling for complementary metal–oxide–semiconductor devices [25]. With different variations scaling is achieved *via* a scavenging reaction between the scavenging element (metal) and  $SiO_2$  and the driving force is also formation of the metal oxide rather than maintaining  $SiO_2$ . We showed previously that the driving force of the clean-up effect is removing As(Ga, In) – O bonds and forming  $M - O$  bonds [25, 131]. As has lower electropositivity and therefore lower affinity to O than the metals considered: Mg, Hf, Zr, Ti, Ta and Al. In thermodynamic equilibrium, formation of any of the oxides of these metals is assumed to be favored over formation of the As oxide. DFT energetics for the ligand exchange mechanism supports this supposition, independent of the ligand in use (see [Figure 5-3](#) A, A' and A''). Among the III-V elements (As, Ga, In) it is again As that has the lowest electropositivity and forms the weakest oxides. To emphasize this we calculate from first principles bulk energies for ligand exchange between the regarded precursors and Ga(III) and In(III) native oxides and compare them with the exchange energy for As(III) native oxide:

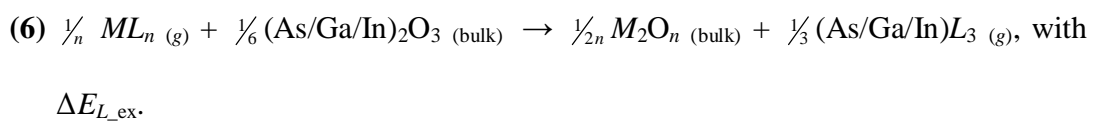


Figure 5-5 shows the energetics for the above reaction on the example of alkylamide precursors ( $L = [\text{NMe}_2]^-$ ). It is clearly seen that  $\text{As}_2\text{O}_3$  is the weakest and the most reactive among these native oxides towards exchanging O with ligands and therefore is the easiest to clean-up. It seems that In oxide resists clean-up more than Ga oxide and is less likely to bind to ligands at the surface. This result holds true for different ligands (see Figure 5-6).

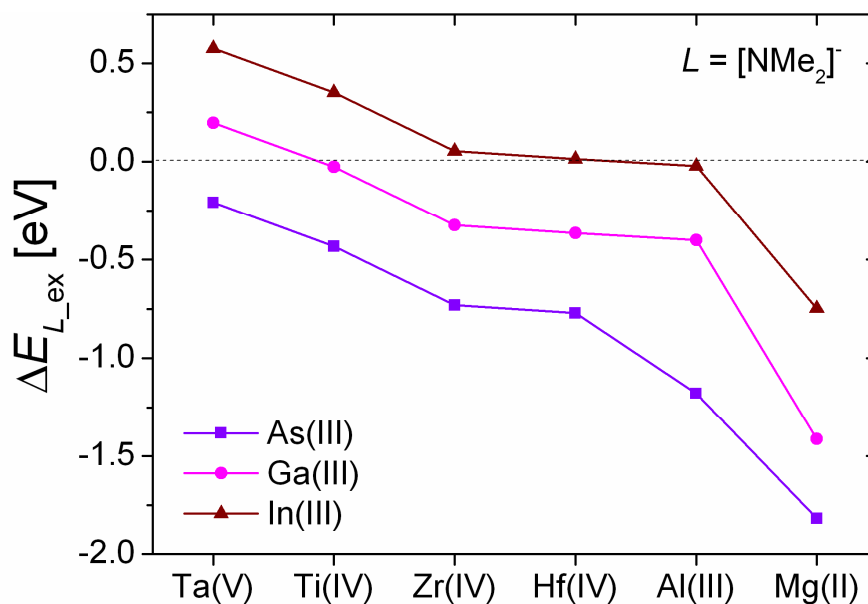


Figure 5-5 Computed energetics for ligand exchange of alkylamide between precursor metal center and bulk III-V oxide:  $\text{As}_2\text{O}_3$ ,  $\text{Ga}_2\text{O}_3$  and  $\text{In}_2\text{O}_3$  according to:  $1/n \text{ML}_n(\text{g}) + 1/6 (\text{As/Ga/In})_2\text{O}_3(\text{bulk}) \rightarrow 1/2n \text{M}_2\text{O}_n(\text{bulk}) + 1/3 (\text{As/Ga/In})\text{L}_3(\text{g})$  for  $M = \text{Mg(II)}$ ,  $\text{Al(III)}$ ,  $\text{Ti(IV)}$ ,  $\text{Zr(IV)}$ ,  $\text{Hf(IV)}$ ,  $\text{Ta(V)}$  and  $L = [\text{N(Me)}_2]^-$ . Lines are to guide the eye.

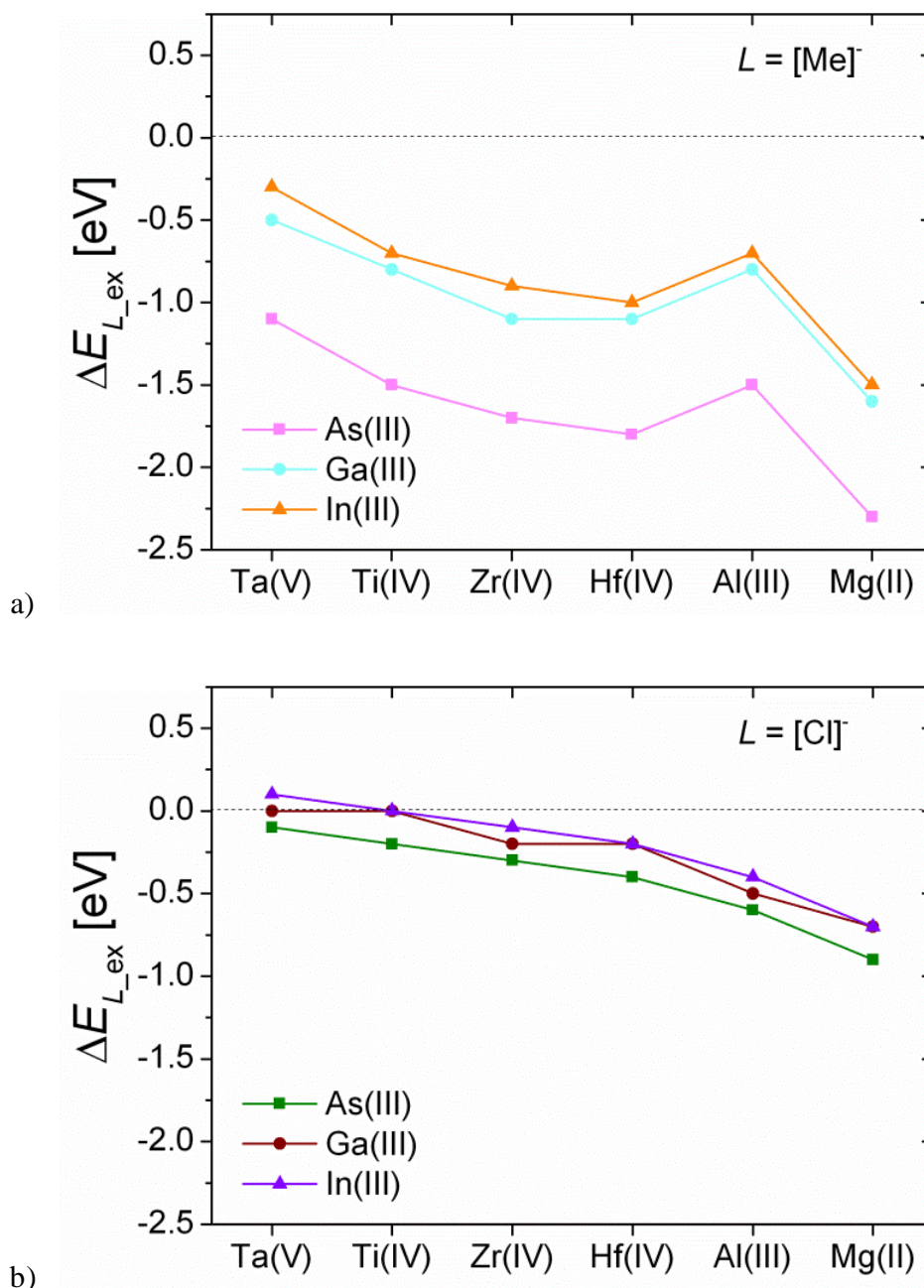
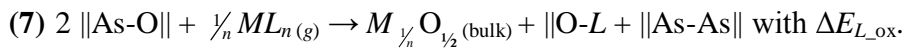


Figure 5-6 Computed energetics for ligand exchange between precursor metal center and bulk III-V oxide:  $\text{As}_2\text{O}_3$ ,  $\text{Ga}_2\text{O}_3$  and  $\text{In}_2\text{O}_3$  according to:  $1/n ML_n (\text{g}) + 1/6 (\text{As/Ga/In})_2\text{O}_3 (\text{bulk}) \rightarrow 1/2n M_2\text{O}_n (\text{bulk}) + 1/3 (\text{As/Ga/In})L_3 (\text{g})$  for  $M = \text{Mg(II)}$ ,  $\text{Al(III)}$ ,  $\text{Ti(IV)}$ ,  $\text{Zr(IV)}$ ,  $\text{Hf(IV)}$ ,  $\text{Ta(V)}$  and  $L = \text{a) [Me]⁻}$  b)  $[\text{Cl}]⁻$ . Lines are to guide the eye.

Additionally, ligands left on the surface can enhance the clean-up effect by interacting with the substrate and this depends on the affinity of the ligand to the substrate and on the chemical character of the substrate. We consider first ligand affinity. Metalloid oxides, like  $\text{AsO}_x$ , are susceptible to reduction in contact with reducing agents, *e.g.* by the methanide anion  $\text{Me}^-$  in TMA as we showed previously [131] or by  $\text{CH}_2$  from

deprotonated alkylamide (section 5.5.1, C). Self-cleaning by TMA was shown to be governed by mobility of the methyl group, which undergoes oxidation, transferring electrons to the surface. Various elementary steps were found to be thermodynamically competitive and to lead to a surprising range of by-products. However, dma  $[\text{NMe}_2]^-$  and chloride  $\text{Cl}^-$  anions are not as strong reducing agents as  $\text{Me}^-$ . This is supported by DFT energies, shown in **Figure 5-7**, for reactions of transferring those ligands from the metal center of the precursor to a surface O site on the  $\text{As}_2\text{O}_3$  substrate. Formation of  $\|\text{O} - \text{L}$  surface intermediates causes reduction of metalloid oxides:



In **Figure 5-7** we can see that the chloride ligand, almost independently of which metal center it is bound to, is resistant to oxidation with  $\Delta E_{L_{\text{ox}}}$  around +2.5 eV. The same holds for dma with  $\Delta E_{L_{\text{ox}}} \approx +1.2$  eV, except for  $\text{Mg}(\text{NMe}_2)_2$  that can dissociate its ligand to the O in the  $\text{As}_2\text{O}_3$  substrate with  $\Delta E_{L_{\text{ox}}}$  a little below 0 eV. On the contrary, the methyl group is always susceptible to oxidation with exothermic  $\Delta E_{L_{\text{ox}}}$  for all metal precursors selected.

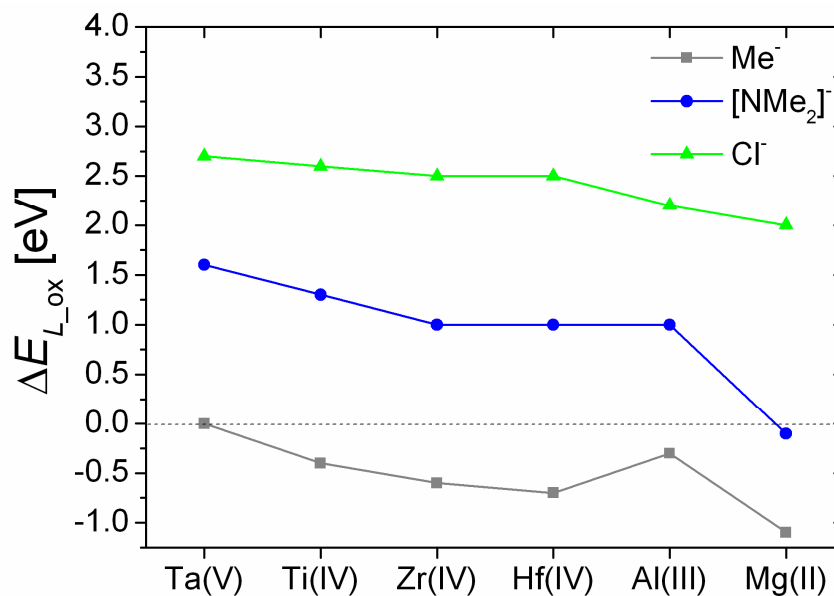


Figure 5-7 Computed energetics for ligand oxidation at the surface,  $L = [N(Me)_2]^-$ ,  $[Me]^-$ ,  $[Cl]^-$ , and  $As_2O_3$  reduction according to:  $2 ||As-O|| + 1/n ML_n (g) \rightarrow M_{1/n}O_{1/2} (bulk) + ||O-L + ||As-As||$  for  $M = Mg(II)$ ,  $Al(III)$ ,  $Ti(IV)$ ,  $Zr(IV)$ ,  $Hf(IV)$ ,  $Ta(V)$ . Lines are to guide the eye.

The second factor affecting clean-up is substrate chemistry. If a ligand is susceptible to decomposition, specific sites on the surface can activate some bonds of the ligand and this can trigger secondary surface reactions that result in clean-up. C-H and N-C bonds of the dma ligand can be activated even at relatively low temperature as discussed in previous sections. It has been shown that especially mixed nucleophilic-electrophilic character of the surface sites, *e.g.* the zwitterionic character of silicon, affects reactivity and transformations of alkylamides [139, 140]. Such reactivity of alkylamides is confirmed by experimental observation of formation of Si-H bonds accompanied by the formation of Si-C bonds (leading to incorporation of carbon into the deposited film). Low temperature production of methane has also been observed, which is evidence for N-C reactivity when depositing oxide films on bare Si or hydrogen terminated Si substrates. In our calculations, we see similar behaviour of the alkylamide ligand on the relatively weakly amphoteric  $As_2O_3$  substrate. On this oxide substrate H is removed from the ligand as a proton and formation of O-H bonds is plausible. In this process clean-up is achieved, as

well as producing additional reactive sites (OH) for ALD, but at the same time  $M$ -C bonds are formed. This is because proton elimination causes changes in electronic density on alkylamide carbons: the  $\text{CH}_2$  fragment becomes Lewis basic and this promotes  $M$ -C formation (B), or the  $\text{CH}_3$  fragment attracts the charge, and  $\text{CH}_3^-$  detachment is promoted, resulting also in  $M$ -C formation (J). Some of these reactions may be more strongly favoured on the mixture of more electropositive  $\text{Ga}^{3+}$  and  $\text{In}^{3+}$  sites of the real III-V surfaces or even the  $M^{n+}$  sites of the growing film, where bonds tend to be more ionic rather than covalent. Based on this we can conclude that the above-mentioned mechanisms account for the reactivity and behaviour of metal alkylamides and can be expected on various substrates featuring Lewis acid/base sites.

An important aspect is whether these processes occur during homodeposition (*e. g.* during the later stages of growth of  $\text{HfO}_2$  onto  $\text{HfO}_2$ ) and give a CVD component to standard ALD. Clearly during homodeposition there is no extra driving force from  $M_2O_n$  formation. On the other hand, decomposition reactions may be more favoured on the growing film owing to its pronounced nucleophilic-electrophilic or Lewis acid/base character, as mentioned above. According to our computations processes yielding B-K are uphill from formation of intermediate A onwards. However the formation of B and J are only +0.5 eV and +0.8 eV uphill respectively at 0 K for clean-up process on the  $\text{As}_2\text{O}_3$  substrate and can be expected at elevated temperatures. This finding is supported by experimental observation of increased efficiency of clean-up with increased temperature.

. Another aspect is simple consideration of strength of As-O bond and Hf-O bond. Clearly the Hf-O bond, once it is formed, is much stronger and less reactive, which is not in favour of CVD reactions. An explicit investigation of CVD reactions on the  $\text{HfO}_2$  surface is necessary to fairly judge the importance of the CVD contribution in case of alkylamide ALD, but is beyond the scope of this work.



## 5.8 Conclusion

We have successfully applied our model for clean-up to explain the differences in the performance of various classes of precursor chemicals in removing native oxide from III-V substrates. Building on the example of TMA, we identify two separate factors governing the clean-up effect: formation of the metal oxide as the primary driving force and affinity of the precursor ligand to the III-V oxide substrate as the ancillary force. That allows an efficient description of interactions of the various precursor ligands with an oxidised III-V substrate, and of the associated multi-step chemical processes that lead to formation of the clean-up products. We map out reaction sequences for the alkylamide ligand that lead plausibly to products that are detected experimentally (aziridine, ethylene, MMI, HCN, methane). Through this approach, a set of general reactions is generated and comparison is made between several different precursors, including metal alkylamides  $\text{Mg}[\text{N}(\text{CH}_3)_2]_2$ ,  $\text{Al}[\text{N}(\text{CH}_3)_2]_3$ ,  $\text{Ti}[\text{N}(\text{CH}_3)_2]_4$ ,  $\text{Zr}[\text{N}(\text{CH}_3)_2]_4$ ,  $\text{Hf}[\text{N}(\text{CH}_3)_2]_4$ ,  $\text{Ta}[\text{N}(\text{CH}_3)_2]_5$ ; metal methyls:  $\text{Mg}(\text{CH}_3)_2$ ,  $\text{Al}(\text{CH}_3)_3$ ,  $\text{Ti}(\text{CH}_3)_4$ ,  $\text{Zr}(\text{CH}_3)_4$ ,  $\text{Hf}(\text{CH}_3)_4$ ,  $\text{Ta}(\text{CH}_3)_5$ ; and metal chlorides:  $\text{MgCl}_2$ ,  $\text{AlCl}_3$ ,  $\text{TiCl}_4$ ,  $\text{ZrCl}_4$ ,  $\text{HfCl}_4$ ,  $\text{TaCl}_5$ . We can therefore predict the best reagent for achieving the clean-up effect.

We predict that the investigated methyl precursors are the best reagents for deposition of dielectrics and performing clean-up. Unfortunately, most of them are very unstable compounds. Clean-up is most effective when depositing  $\text{MgO}$ , as  $\text{Mg}^{2+}$  works as the most effective scavenger of  $\text{O}^{2-}$ . Clean-up with metal chlorides has a fundamentally different mechanism, probably involving removal of the O from the native oxide film and passivation with Cl groups.

The first principles study shows that clean-up with metal alkylamides has a similar mechanism to clean-up with metal methyls as regards the scavenging of oxygen from weak As, Ga and In oxides. Arising from this, ligand exchange can in principle lead to a clean-up product: tris(dimethylamino)arsine. However steric hindrance and the bulky

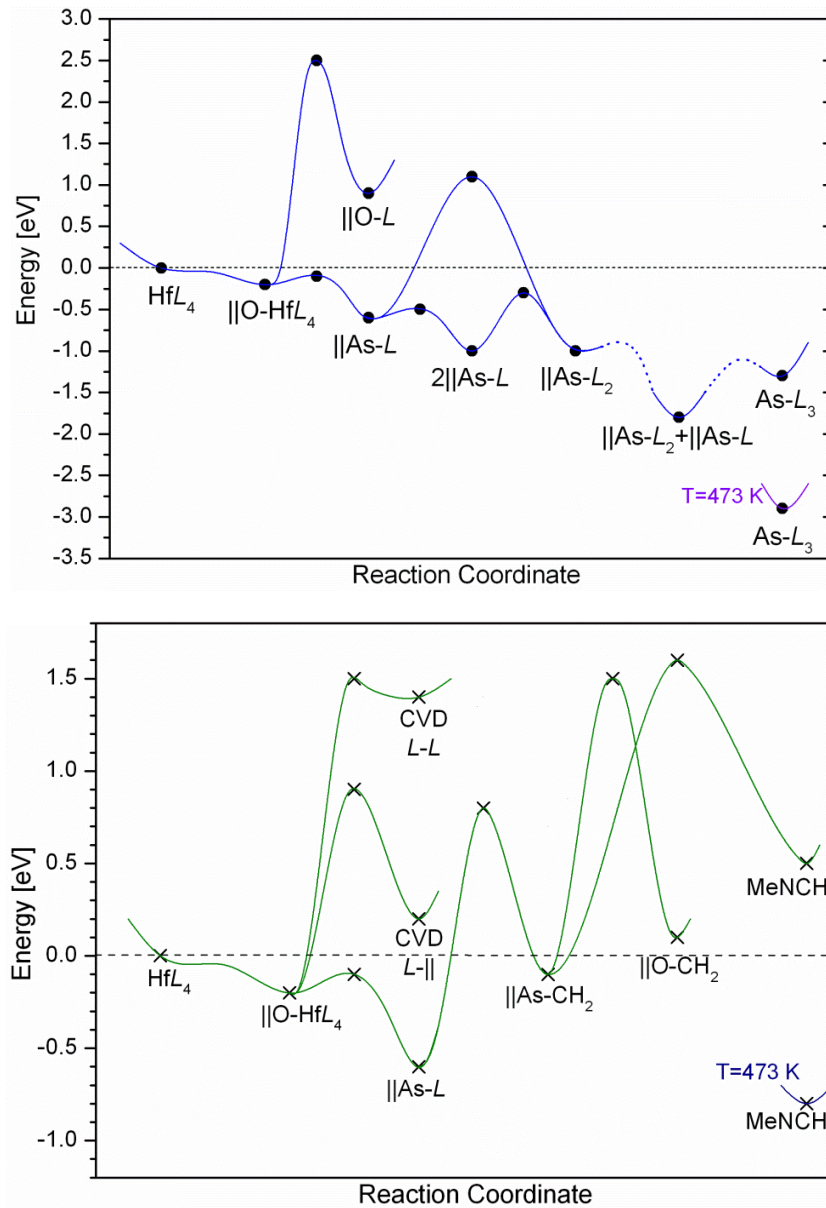
character of the alkylamide ligand are rate limiting factors, which in this case are very pronounced and suggest that this particular reaction will not proceed.

Our study also shows the difference in mechanism underlying the consumption of III-V oxides with alkylamido precursors from the one taking place with TMA. In the case of the alkylamide ligand, thermal decomposition rather than migration of the entire ligand on the oxide surface is dominant, taking into account the bulky character of the ligand and its known reactivity in contact with a semiconductor or metallic surface. Clean-up of the reducible As oxide substrate is therefore enhanced by secondary decomposition surface reactions, not by oxidation of the entire alkylamide. The H elimination process that forms hydroxyl groups and As-C bound species (B) is exothermic or neutral at 0 K and so very plausible. The migration of these decomposition intermediates from As site to O site (C) and direct reduction of the substrate is only slightly endothermic. Successive dehydrogenation though becomes progressively less favored. Instead, the first H elimination may be followed by another plausible reaction – N-C bond scission (J), which can lead to low temperature methane production, albeit without clean-up effect. Thermal activation is needed for formation and desorption of products that arise from these decomposition structures: most likely N-methylmethyleimine and aziridine possibly along with methane, ethylene and dinitrogen. A specific requirement of the substrate is that it contain both Lewis acid and Lewis base sites, which can activate secondary surface reactions of ligands that are susceptible to decomposition, like the dimethylamido group. These redox processes do lead to the reduction of arsenic oxides to metallic arsenic, which in turn can reduce gallium and indium oxides to pure III-V material. Some of the reactions that we have presented therefore account for the clean-up effect.

More generally we show that organometallic reagents react readily with substrates featuring less electropositive metals. In presence of metals like Si, As, Ga and In, a reactive polar metal-organic ligand bond, *e.g.* Al-C, is broken and formation of more

covalent bond, *e.g.* As-C, is favoured. These reactions might be possible during homodeposition and can thereby give a CVD component to standard ALD, as is well-documented for alkylamides. The mechanisms described here are in line with observations on Si surfaces as well. The same mechanisms can therefore be expected on other substrates, such as oxides and nitrides, that show a mix of Lewis acid/base sites.

## 6 Mechanisms for decomposition of metal alkylamides at reducible oxide surfaces



*In this chapter mechanisms occurring during initial cycles of the atomic layer deposition of hafnium oxide films on an oxidized III-V substrate are investigated. Bulk reaction energies were obtained for candidate processes achieving the clean-up effect and this indicated which processes are favoured overall. Through these investigations we proved that tetrakis(dimethylamido)hafnium is a clean-up reagent. Quantitative structures and energetics along the reaction pathways were also obtained in order to investigate the actual mechanisms occurring on the native oxide surface.*

## 6.1 Introduction

Various metal alkylamides have been utilized for the interfacial cleaning during ALD deposition of dielectrics onto III-V semiconductors. We consider a process for the clean-up effect during HfO<sub>2</sub> deposition using the example of arsenic (III) oxide and TDMAH. As showed in chapter 5, this process is governed by HfO<sub>2</sub> formation. The interaction of the metal precursor with the substrate and, in case of metal alkylamides, decomposition of the ligand lead to the scavenging of oxygen and formation of the volatile products from the organic ligands.

In the previous chapter we investigated the decomposition of the dimethylamido ligand on an As<sub>2</sub>O<sub>3</sub> substrate and plausible products arising from the lowest energy surface intermediates were revealed. We showed that the alkylamide ligand can readily dissociate from the precursor metal center to the native oxide substrate. The ligand as a whole is not susceptible to the oxidation but, when released to the substrate, is prone to further transformations. The H elimination process that results in formation of hydroxyl groups and As-C bound species is very plausible. Our DFT study suggested also that scission of the N-C bond becomes plausible when preceded by H elimination and results in formation of As-CH<sub>3</sub> groups. Successive dehydrogenation of the dimethylamido ligand becomes more and more endothermic and is temperature dependent. The thermodynamic accessibility of these elementary steps led us to the conclusion that tris(dimethylamino) arsenic, N-methyl methyleneimine, aziridine and, along with methane, ethylene and nitrogen are possible products of the clean-up with the use of alkylamides. However reaction energetics were not presented in chapter 5. The mechanisms resulting in desorption of these chemicals certainly involve ligand exchange, decomposition of the ligand and reduction of the arsenic oxide substrate, but the detailed pathways remain to be determined.

In the current chapter, we examine thermodynamic energetics for formation of clean-up by-products during ALD with alkylamides. Also, we consider the temperature dependence of their formation by computing energies plus entropies applied to bulk solids and gas-phase molecules. This analysis gives a first overview on the favorable interactions of the alkylamide precursor with a III-V substrate. While these gas-solid computations are useful for screening over a wide range of potential clean-up products, they cannot reveal the exact mechanisms that take place. To investigate the details of the interactions between the precursor and the substrate we use the slab model of the surface. In this more realistic approach we can study adsorption of the precursor at the surface, precursor-surface interactions and in particular reaction barriers, which allow us to examine which mechanistic path is kinetically accessible. Taken together, along with previous investigations, these models reveal some important aspects of the interfacial self-cleaning during deposition of the dielectrics onto semiconductor substrates.

## 6.2 Survey of possible products using bulk and gas-phase models

Sample overall clean-up reactions (1)-(8) are given in Table 6-1 along with the DFT energetics at 0 K. The temperature dependence over the range of 0 – 1200 K for the free energy for those reactions is illustrated in Figure 6-1. Reactions (1)-(7) are all based on the assumption that all available oxygen originating from III-V native oxides is scavenged by incoming precursor metal to form dielectric oxide. This leads to transformation of the arsenic in the native oxide into possibly volatile products. We regard four different classes of arsenic products based on the mechanisms leading to their formation: ligand exchange leads to tris(dimethylamino) arsine, TDMAAs,  $\text{As}[\text{N}(\text{CH}_3)_2]_3$ , in reaction (1); ligand decomposition through dissociation of Me groups to surface As can result in production of trimethyl arsine,  $\text{As}(\text{CH}_3)_3$ , (2) and (5); ligand decomposition through dissociation of H to As results in desorption of arsine,  $\text{AsH}_3$ , (3) and (6); and electron

transfer mechanism leading to reduction of the oxide surface to metallic arsenic, As, (4) and (7). The organic by-products arising directly from these mechanisms are: dimethyldiazene, N<sub>2</sub>Me<sub>2</sub>, as a result of N-Me scission in (2); N-methyl methyleneimine, MeNCH<sub>2</sub> (MMI), is formed in the H elimination process (3) and tetramethylhydrazine, N<sub>2</sub>Me<sub>4</sub>, when electrons are transferred to the oxide surface as a result of ligand oxidation (4).

Reaction				$\Delta E_{(b)}^{0K}$	
(1)	$\frac{1}{4}$ Hf(NMe <sub>2</sub> ) <sub>4</sub>	$+\frac{1}{6}$ As <sub>2</sub> O <sub>3</sub>	$\rightarrow\frac{1}{4}$ HfO <sub>2</sub>	$+\frac{1}{3}$ As(NMe <sub>2</sub> ) <sub>3</sub>	-0.8
(2)				$+\frac{1}{3}$ AsMe <sub>3</sub> + $\frac{1}{2}$ N <sub>2</sub> Me <sub>2</sub>	-0.3
(3)				$+\frac{1}{3}$ AsH <sub>3</sub> + MeNCH <sub>2</sub>	+0.2
(4)				$+\frac{1}{3}$ As + $\frac{1}{2}$ N <sub>2</sub> Me <sub>4</sub>	-0.6
(5)				$+\frac{1}{3}$ AsMe <sub>3</sub> + $\frac{1}{2}$ N <sub>2</sub> + $\frac{1}{2}$ CH <sub>4</sub> + $\frac{1}{4}$ C <sub>2</sub> H <sub>4</sub>	-1.0
(6)				$+\frac{1}{3}$ AsH <sub>3</sub> + $\frac{1}{2}$ N <sub>2</sub> + $\frac{1}{2}$ CH <sub>4</sub> + $\frac{3}{4}$ C <sub>2</sub> H <sub>4</sub>	-0.3
(7)				$+\frac{1}{3}$ As + $\frac{1}{2}$ N <sub>2</sub> + CH <sub>4</sub> + $\frac{1}{2}$ C <sub>2</sub> H <sub>4</sub>	-1.0
(8)		$+\frac{1}{3}$ As <sub>2</sub> O <sub>3</sub>	$+\frac{2}{3}$ As + $\frac{1}{2}$ N <sub>2</sub> + CH <sub>4</sub> + $\frac{1}{2}$ C <sub>2</sub> H <sub>4</sub> + $\frac{1}{4}$ O <sub>2</sub>	0.0	

Table 6-1 Energies at 0 K for possible products of ‘clean-up’ reaction of As<sub>2</sub>O<sub>3</sub>. Given energies are bulk potential energies. All energies are shown in eV.

DFT reaction energies at 0 K suggest that the clean-up transformation will lead most likely to production of TDMAAs or metallic As (Table 6-1, reaction (1), (4) in comparison with (2) and (3)). Less competitive are processes resulting in desorption of trimethyl arsine or arsine (Table 6-1, reactions (2) and (3)). However, computed thermodynamics show these processes to be more favored with increasing temperature and to become dominant above around 400 K (Figure 6-1). This consideration is rather simplistic and represents one extreme where we scan possible final products of arsenic. The residual organics can further transform, which is investigated below.

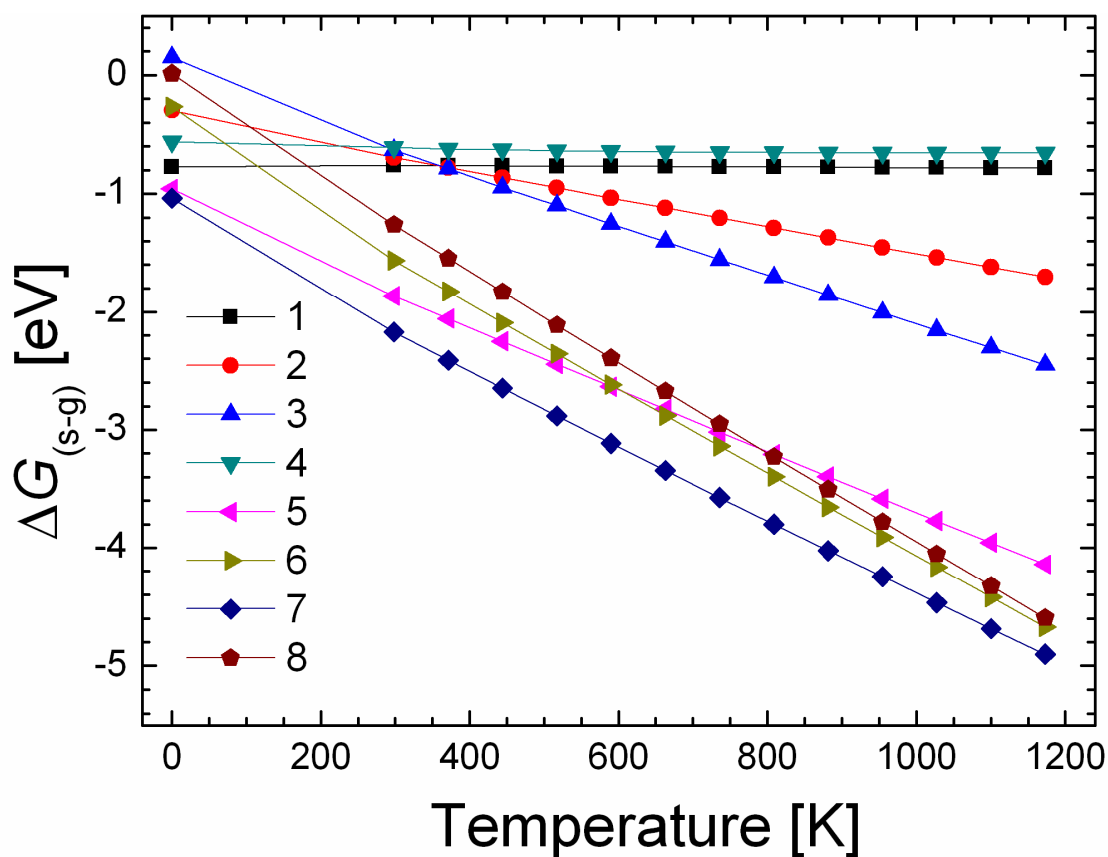


Figure 6-1 Temperature dependence of free energy for ‘clean-up’ with  $\text{Hf}(\text{NMe}_2)_4$  reactions applied to bulk solids and gas-phase molecules. Corresponding reactions are given in Table 6-1.

The residual organic ligands are prone to decompose in the contact with an oxide substrate and possible decomposition products are listed in Table 6-2 along with the 0 K energetics.



Reaction			$\Delta E^{0K}$
(9)	$\frac{1}{2} \text{N}_2\text{Me}_4$	$\rightarrow \frac{1}{2} \text{N}_2 + \text{CH}_4 + \frac{1}{2} \text{C}_2\text{H}_4$	-0.5
(10)		$\rightarrow \frac{1}{2} \text{Me(H)NCH}_2\text{NMe}_2$	-0.4
(11)		$\rightarrow \frac{1}{2} \text{HNMe}_2 + \frac{1}{2} \text{MeNCH}_2$	-0.1
(12)		$\rightarrow \text{H}_2\text{NCHCH}_2 + \frac{1}{2} \text{H}_2$	+0.2
(13)		$\rightarrow \frac{1}{2} \text{N}_2\text{Me}_2 + \frac{1}{2} \text{CH}_4 + \frac{1}{4} \text{C}_2\text{H}_4$	+0.2
(14)		$\rightarrow \text{HNCH}_2 + \frac{1}{2} \text{CH}_4 + \frac{1}{4} \text{C}_2\text{H}_4$	+0.4
(15)		$\rightarrow \text{HCN} + \text{CH}_4 + \frac{1}{2} \text{H}_2$	+0.7
(16)		$\rightarrow \text{HN(CH}_2)_2 + \frac{1}{2} \text{H}_2$	+1.0
(17)		$\text{C}_2\text{H}_6$	$\rightarrow \text{CH}_4 + \frac{1}{2} \text{C}_2\text{H}_4$
(18)	$\rightarrow \text{C}_2\text{H}_4 + \text{H}_2$		+1.8
(19)	$\rightarrow \text{C}_2\text{H}_2 + 2 \text{H}_2$		+4.1

Table 6-2 Possible decomposition products of tetramethylhydrazine,  $\text{N}_2\text{Me}_4$ , or ethane,  $\text{C}_2\text{H}_6$ , and the relevant energetics at 0 K. All energies are shown in eV.

Reaction energies are computed relative to a half of  $\text{N}_2\text{Me}_4$ , which stoichiometrically corresponds to one unit of the ligand  $[\text{NMe}_2]$ . Thermodynamics suggest that the most exothermic at 0 K, and in the whole temperature range (Figure 6-2), is oxidation of N to molecular  $\text{N}_2$  and desorption of carbon species possibly as methane,  $\text{CH}_4$ , and ethene,  $\text{C}_2\text{H}_4$  in reaction (9).  $\text{CH}_4$  and  $\text{C}_2\text{H}_4$  are shown by reactions (17)-(19) to be the most favorable products from the methyl group. In Figure 6-2 we see that methane and ethene start to be more competitive than ethane around 400 K (17). Therefore, although there are other possible transformations, *e.g.* leading to production of molecular hydrogen in (18) and (19),  $\text{CH}_4$  and  $\text{C}_2\text{H}_4$  are expected to be the main volatile compounds containing carbon. We compute an energy change of -0.5 eV at 0 K for reaction (9) relative to formation of tetramethylhydrazine. Similar energetics at 0 K, but constant regardless of temperature, are presented by the process in which N-methyl-N'-dimethyl-diaminomethane,  $\text{Me(H)NCH}_2\text{NMe}_2$ , is formed (10). Other possible products of

decomposition are dimethyl amine,  $\text{HNMe}_2$ , along with  $\text{MeNCH}_2$ . Although the energy of reaction (11) is slightly higher at 0 K than for reaction (10),  $\Delta E^{0K} = -0.1$  eV, this process becomes more favored with increased temperature. Reactions (12)-(15) resemble each other in terms of thermodynamics. Formation of the aminoethene,  $\text{H}_2\text{NCHCH}_2$ , and hydrogen,  $\text{H}_2$ , in reaction (12);  $\text{N}_2\text{Me}_2$ ,  $\text{CH}_4$ , and  $\text{C}_2\text{H}_4$ , in (13); methyleneimine,  $\text{HNCH}_2$ , along with  $\text{CH}_4$  and  $\text{C}_2\text{H}_4$  in (14) and hydrogen cyanide,  $\text{HCN}$ , with  $\text{CH}_4$  and  $\text{H}_2$  in (15) costs +0.2; +0.2; +0.4 and +0.7 eV at 0 K respectively. These reactions become exothermic and competitive at elevated temperatures. The least competitive, but also activated with increased temperature, is desorption of aziridine,  $\text{HN}(\text{CH}_2)_2$  and  $\text{H}_2$  as by-product with  $\Delta E^{0K} = +1.0$  eV (16).

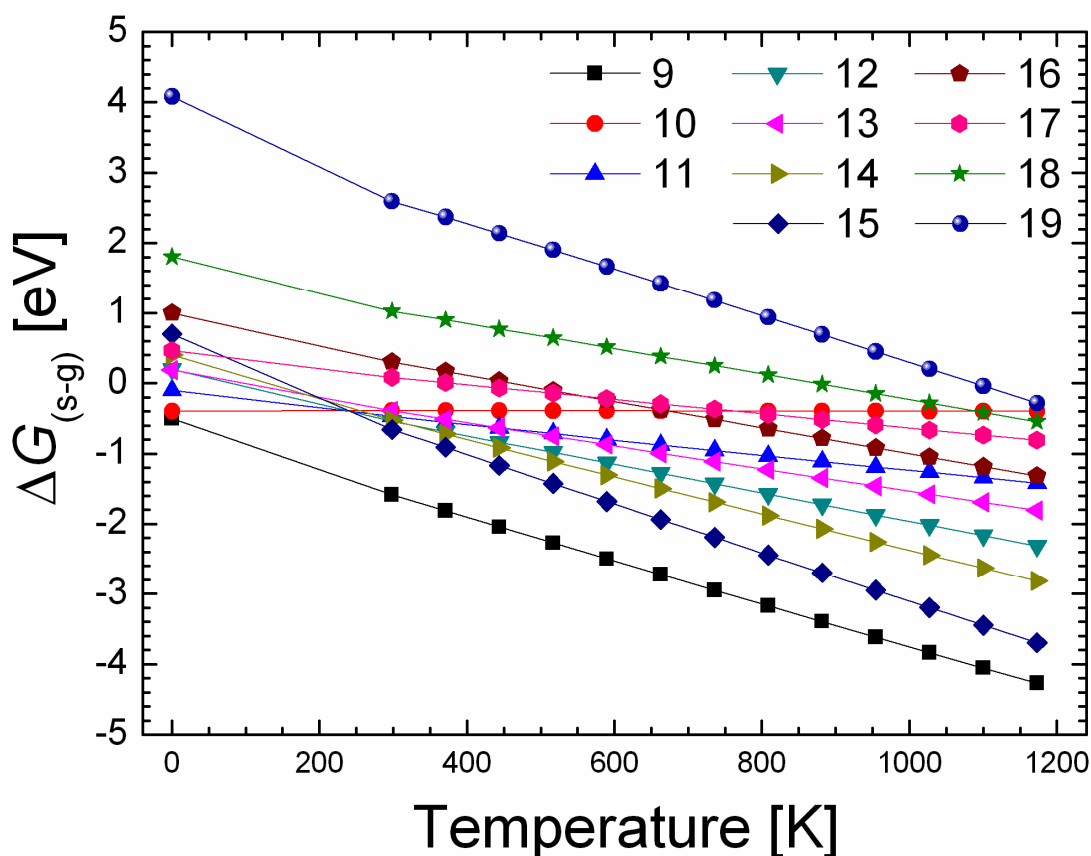


Figure 6-2 Temperature dependence of free energy for decomposition reactions of tetramethylhydrazine,  $\text{N}_2\text{Me}_4$ , or ethane,  $\text{C}_2\text{H}_6$ . Corresponding reactions are given in Table 6-2.

Through reactions (9)-(19), the variety and number of possible by-products is exposed. The most exothermic is transformation of dimethylamide ligand into molecular nitrogen, methane and ethene. Although oxidation of organic ligands to these products is unlikely during the ALD process, we consider reactions (5)-(7) as a second extreme of competing reactions. As expected, this set of processes is much more exothermic than reactions (1)-(4) (see Figure 6-1). Metallic arsenic turns out to be the most favorable form of arsenic products in reaction (7).

Finally, in order to investigate whether oxygen can be transformed into another form than hafnium oxide, we consider an alternative stoichiometry in reaction (8). As another extreme case we consider production of molecular oxygen, O<sub>2</sub>, along with HfO<sub>2</sub>, but other oxygen products are possible *e.g.* dimethyl ether, OMe<sub>2</sub>, or water, H<sub>2</sub>O.  $\Delta E^{0K}$  for reaction (8) is neutral however this process becomes strongly exothermic with temperature. Comparing Gibbs free energies for reaction (8) and for the most favorable process in which all available oxygen in arsenic oxide is bound with hafnium, reaction (7), we can conclude that these processes are competitive though process (7) might be dominating (Figure 6-1). Looking at the stoichiometries, process (8) can be more dominant in the early stages when the substrate consists mainly of arsenic (III) oxide, as the proportion of As<sub>2</sub>O<sub>3</sub> formula units to the number of precursor molecules is 4:3, while for reaction (7) is only 2:3.

The above consideration of bulk potential energies for selected processes helps to identify main reaction mechanisms. Most of the regarded processes are redox (except (1)). Transformation of arsenic oxide into volatile trimethyl arsine or arsine ((2), (3), (5), (6)) is a redox process in which charge is transferred within organic ligands. The most exothermic process is the one where arsenic (III) oxide is reduced to metallic arsenic ((4), (7) and (8)). The charge is transferred from organic ligands to the oxide substrate (4) and

within the ligand in the disproportionation reactions (7) and (8). Redox and disproportionation reactions are possible *via* direct oxidation of the ligand and/or *via* decomposition processes: H elimination and N-C bond scission. In the remainder of this section we examine the processes of nitrogen oxidation by investigating the stability of the As<sub>2</sub>O<sub>3</sub> in the presence of nitrogen. In subsequent sections redox mechanisms are considered on the surface model.

Bulk potential energies computed at 0 K for nitrogen oxidation to all possible nitrogen oxides and arsenic oxide reduction to metallic arsenic are given in Table 6-3. As expected, N<sub>2</sub> is very weak reducing agent and conversion of arsenic oxide into metallic arsenic through formation of N-O bonds is highly unlikely. We compute +1.1 eV per N atom for formation of dinitrogen monoxide, N<sub>2</sub>O (20); +3.4 eV for nitrogen monoxide, NO (21); +3.1 eV for dinitrogen trioxide, N<sub>2</sub>O<sub>3</sub> (22); +4.3 eV for nitrogen dioxide, NO<sub>2</sub> (23); and +4.5 eV for dinitrogen pentoxide, N<sub>2</sub>O<sub>5</sub> (24). Based on this we can conclude that redox and disproportionation processes occur most likely through decomposition of the alkylamide ligand rather than direct oxidation *via* N-O bond formation.

Reaction				$\Delta E^{0K}$
(20)	$\frac{1}{6} \text{As}_2\text{O}_3$	+ $\frac{1}{2} \text{N}_2$	$\rightarrow \frac{1}{2} \text{N}_2\text{O} + \frac{1}{3} \text{As}$	+1.1
(21)	$\frac{1}{3} \text{As}_2\text{O}_3$		$\rightarrow \text{NO} + \frac{2}{3} \text{As}$	+3.4
(22)	$\frac{1}{2} \text{As}_2\text{O}_3$		$\rightarrow \frac{1}{2} \text{N}_2\text{O}_3 + \text{As}$	+3.1
(23)	$\frac{2}{3} \text{As}_2\text{O}_3$		$\rightarrow \text{NO}_2 + \frac{4}{3} \text{As}$	+4.3
(24)	$\frac{5}{6} \text{As}_2\text{O}_3$		$\rightarrow \frac{1}{2} \text{N}_2\text{O}_5 + \frac{5}{3} \text{As}$	+4.5

Table 6-3 Stability of As<sub>2</sub>O<sub>3</sub> at 0 K in presence of nitrogen. Given energies are bulk potential energies. All energies are shown in eV per N atom.

### 6.3 Adsorption at bare native oxide surface

To investigate the interaction of the precursor molecule with the substrate we start by looking at the adsorption mechanisms. We use a 2×2 surface expansion of (010)-

*arsenolite* that contains 1 layer totaling 8 molecular units of  $\text{As}_4\text{O}_6$  (80 atoms) and a  $2 \times 2 \times 1$   $k$ -point mesh for surface calculations as in the previous chapter. Additionally, because of the larger size of the alkylamide molecule, the energy of the slab with increased vacuum separating periodic images up to 20 Å was tested. This test showed that also in this case a total vacuum of 10 Å thickness is sufficient to decrease interaction in the  $z$  direction of the supercell. In **Figure 6-3** we show the relaxed structure of the surface and the adsorbed  $\text{Hf}(\text{NMe}_2)_4$  precursor. The initial contact of the precursor molecule with the native oxide can occur through interaction of the precursor metal center with the O site, N Lewis base attack of the As site and through H elimination. A number of geometries have been tested and the most stable are shown in **Figure 6-3 a), b) and c)**.

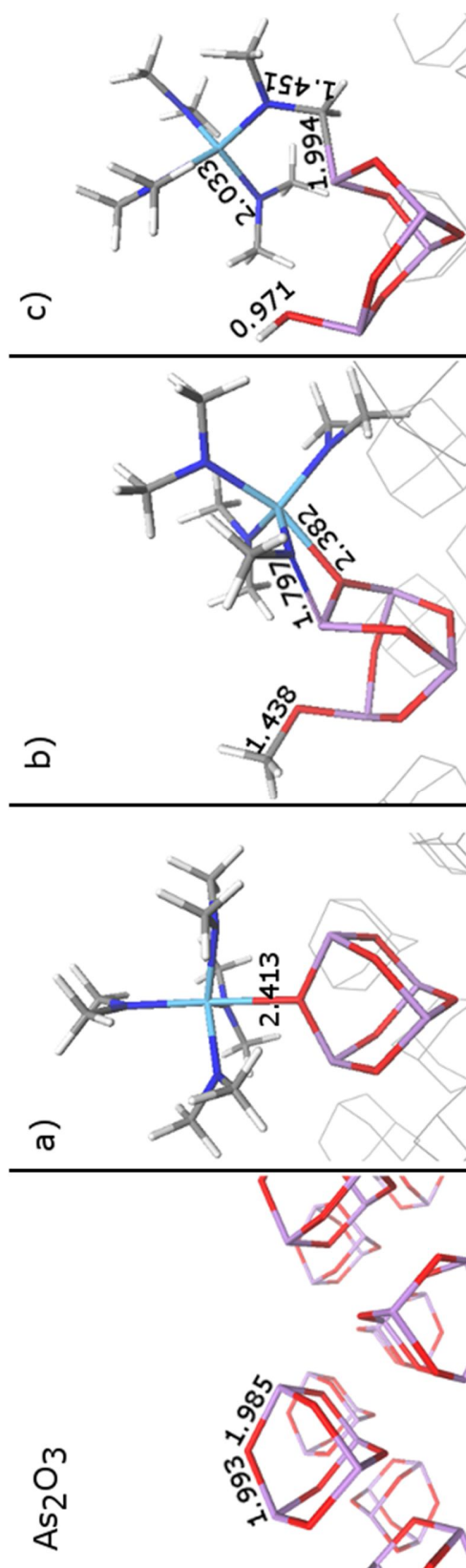


Figure 6-3 Surface models for *arsenolite*-As<sub>2</sub>O<sub>3</sub> and different adsorption modes for Hf(NMe<sub>2</sub>)<sub>4</sub> precursor: a) molecular chemisorption; b) dissociative chemisorption through scission of N-C bond; c) dissociative chemisorption through scission of C-H bond. Stick representation: purple As, red O, white H, gray C, green Cl, blue N, light blue Hf. Selected bond lengths are given in Å. Thin lines show adjacent substrate atoms.

A Lewis adduct is formed as a result of the interaction of the precursor metal center with the exposed O site of the native oxide surface (**Figure 6-3 a**). The Hf-O bond is formed upon overlap of the metal *d*-orbitals with the lone pair of electrons on O. The length of the formed bond is computed to be 2.4 Å. There are no substantial changes in the geometry of the adsorbed precursor compared with the gas phase, nor in the oxide substrate, except of course that the metal center increases its coordination number from 4 to 5. We compute -0.2 eV of energy gain upon this form of weak chemisorption. This is typical for other metal precursors as well as other oxide surfaces [112, 131].

Further sticking of the alkylamide precursor to the substrate can derive from the ligand N atom. The Lewis basic N in the alkylamide ligand can attack a surface As site. This drives the reaction to the state in which a methyl group dissociates as methylium cation and binds with a surface O. The relaxed geometry is shown in **Figure 6-3 b**. This dissociative chemisorption is endothermic with +0.5 eV with respect to the separated reactants. The structure is quite strained as also Hf interacts with the nearest O lone pair forming a bond of length 2.4 Å. This affects the bond between reactive N and Hf, which is weakened (about 6% shorter than the Hf-N bond in the precursor gas molecule) and distorts the planar geometry of the original ligand.

H elimination upon precursor adsorption onto the oxide substrate is conceivable. In this mechanism H is eliminated from a ligand as a proton ( $H^+$ ) and diffuses to a surface O site. The precursor molecule can then easily bind with a Lewis acidic As site through the Lewis basic C in the remaining  $CH_2$  moiety (**Figure 6-3 c**). The computed As-C bond is around 2.0 Å long. In the precursor, the Hf-N and N-C distances are consistent with those of the gas phase molecule, being around 2.0 Å and 1.5 Å respectively. However, the DFT energy change computed for this dissociative adsorption is positive, +0.7 eV.

We thus show that adsorption of the alkylamide precursor at the native oxide surface is due to an interaction of the metal center with a surface oxygen. The energetics suggests

that the nature of the adsorption is weak molecular chemisorption due to lowered Lewis acidity of the Hf hindered by bulky ligands. Dissociative adsorption is endothermic and therefore less probable. This is typical and desired behaviour for ALD precursors. Although reports on metal alkylamides are rich in examples indicating the possibility of C-H or N-C dissociation during adsorption, *e.g.* on Si substrate [140], these mechanisms are less feasible in the contact with an oxide surface.

#### **6.4 Migration of the ligand at bare native oxide surface**

In the following sections, we investigate the multi-step chemical processes associated with decomposition of the alkylamide precursor. We focus on characterizing the kinetics of elementary steps through exploration of their activation energies. Most of the processes were identified above as redox reactions. However, as shown in our previous study [131], migration of the ligand from the precursor center to the substrate, but also on the substrate, might be crucial for this kind of system. On the metal oxide surface we consider two pathways for ligand dissociation: the ligand exchange pathway when the ligand migrates to an As site and the redox pathway when the ligand migrates to an O site.



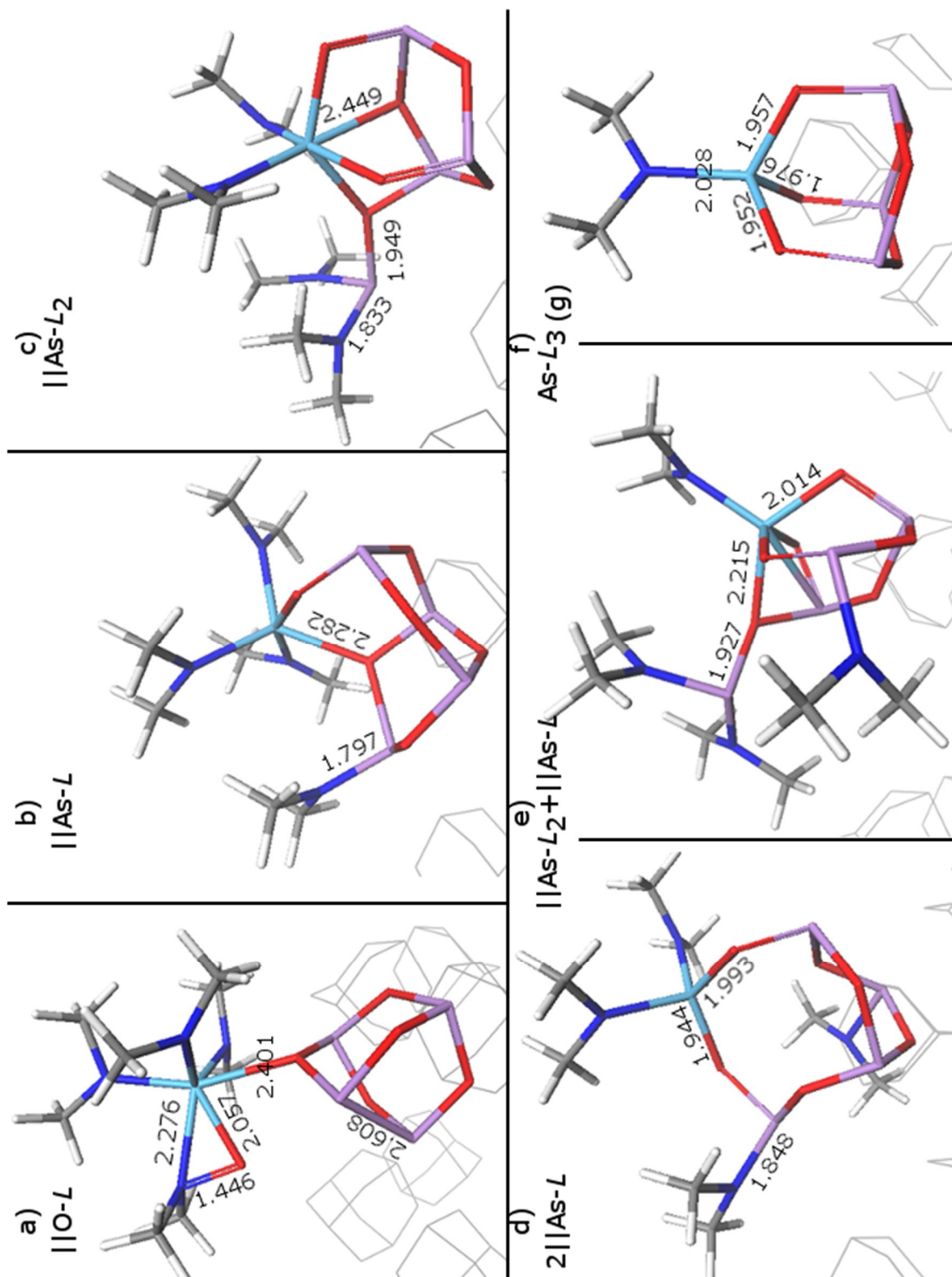


Figure 6-4 Surface models showing products of the migration of dimethylamide ligand,  $L = [\text{NMe}_2]$ , on bare *arsenolite*- $\text{As}_2\text{O}_3$  surface: a) migration to the O site; b) migration to the As site. Surface models c) – e) illustrate products formed in the process of successive migration of ligands to surface As. Surface model f) shows product after desorption of tris(dimethylamino)arsine,  $\text{AsL}_3$ . Stick representation: purple As, red O, white H, gray C, green Cl, blue N, light blue Hf. Selected bond lengths are given in Å. Thin lines show adjacent substrate atoms.

In the first mechanistic path of ligand dissociation we examine scission of the Hf-N bond and formation of the O-N bond. The most stable relaxed structure that we have found is shown in [Figure 6-4 a](#)). In this reaction an O atom is pulled up out of the oxide surface by the alkylamide ligand forming an N-O-Hf-N link. The optimized structure shows the Hf-N bond elongated by around 11 % relative to the original distance between Hf and ligand, but not broken. The bonds formed between N-O and O-Hf are 1.5 and 2.1 Å long respectively. The coordination number of Hf increases from five to six at the expense of two As-O bonds. Formation of the 2.6 Å long As-As metallic bond is evidence of considerable charge reorganization. Bader analysis shows an increase in the electronic density on both As dimer atoms by  $+1.1e$  each and a decrease on the N atom by  $-1.0e$ . Interestingly, charge analysis indicates a charge withdrawal of  $-0.9e$  also from the surface O atom taking part in the reaction. The alkylamide ligand is oxidised upon migration to the O site; electrons are transferred from N and O to As, As is reduced and As-As metallic bond is formed. The calculated energy profile along the minimum energy path (shown in [Figure 6-5](#),  $\|O-L, L = [NMe_2]$ ) shows that oxidation of the alkylamido ligand is endothermic by  $+0.9$  eV and requires a high activation energy of  $+2.7$  eV, perhaps due to the substantial changes in charge and location of O.

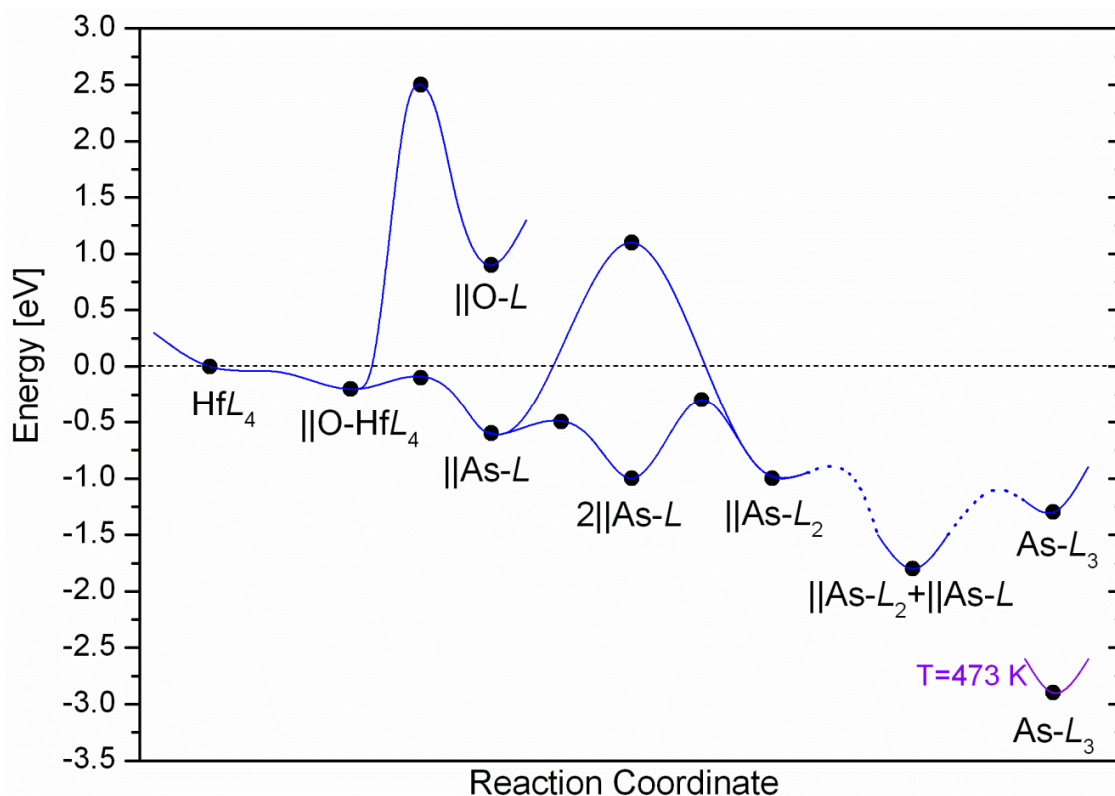


Figure 6-5 Reaction profile for successive migration of dimethylamide ligand,  $L = [\text{NMe}_2]$ , from  $\text{HfL}_4$  adsorbed at the bare arsenolite- $\text{As}_2\text{O}_3$  surface,  $\text{||O-HfL}_4$ . The zero of energy is precursor in the gas phase and bare surface. DFT energetics of the transformations are computed at 0 K and desorption of  $\text{As-L}_3$  product formed (final data point on right-hand side) is corrected with the entropy computed at 473 K. The black dots mark the relative energy of optimized stationary points (either minimums of the structures shown in Figure 6-4 or saddle points of transition states). The solid line indicates the possible reaction pathway; the dotted line represents assumed height of unknown reaction barriers.

Migration of the alkylamide ligand from the precursor metal center to an As site, *i.e.* formation of  $\text{||As-L}$ , is exothermic with reaction energy of -1.0 eV and extremely facile with an activation energy of only +0.1 eV. The reaction profile is shown in Figure 6-5. In this elementary process, scission of the Hf-N bond is followed by formation of the As-N bond, as in the surface product illustrated in Figure 6-4 b). The coordination number of Hf to O is increased at the expense of one As-O bond. There is a negligible reorganization in electronic populations on As, O and Hf atoms. The As-N bond length is shorter by about 14% compared to the Hf-N bond. The alkylamide ligand stays planar about N as in the original geometry of the precursor molecule. In transition metal alkylamides this planarity is due to the stabilization of N lone pair by dative  $p\pi-d\pi$  bond [144]. Although Bader analysis indicates some electron transfer from C atoms (-0.3e and -0.4e) to the N atom

(+0.9e) as the ligand migrates to As, there is no change in N-C bond lengths and the As-N bond preserves significant  $\pi$  character. In this case the lone pair of electrons is conjugated with empty  $p$  orbitals on As.

The results presented in this section so far clearly show that the migration of the alkylamide ligand is only possible in mechanisms not involving charge transfer. Formation of the N-O bond is shown to be not only inaccessible thermodynamically but also hampered by a high activation energy. The computed thermodynamic barrier for this surface reaction is consistent with the bulk energies examined above for formation of nitrogen oxides (section 6.2). On the other hand, migration of the same ligand from the metal center of the precursor to the metal site of the substrate is shown to be extremely facile, both thermodynamically and kinetically. These findings support previous investigations [131]. This non-redox ligand exchange pathway may occur repeatedly and thereby lead directly to desorption of TDMAAs as per reaction (1). However, in the next paragraphs we show that steric hindrance is an obstacle, difficult to overcome, for this type of mechanism.

The reaction profile in [Figure 6-5](#) shows computed and estimated barriers for pathway leading to formation and desorption of TDMAAs molecule. The reaction profile plots the energy change at 0 K upon formation of the various intermediate adsorption structures and entropy-corrected energy change at 473 K upon desorption of the volatile product. Energies are relative to the initially separated oxide surface and precursor.

When a second ligand is transferred from Hf to As, the reaction of surface-adsorbed  $\parallel\text{As-L}$  to  $\parallel\text{As-L}_2$  leads to a gain in energy of 0.4 eV. The  $\parallel\text{As-L}_2$  surface structure is shown in [Figure 6-4 c](#)). The Hf center has a coordination number of six, as it is bound to four oxygen atoms and the remaining two ligands, with Hf-O distances between 2.0-2.5 Å. The  $\text{AsL}_2$  moiety is bound with oxygen through the interaction of the As atom with the lone pair of electrons on the O, forming a 1.9 Å long bond. The reaction profile in [Figure](#)

6-5 shows that there is a considerable barrier of +1.2 eV to be overcome for this reaction. However, the DFT study reveals that this high kinetic requirement can be decreased when transfer of the second ligand proceeds in two steps. The first step is transfer of a second ligand from the precursor metal center to a different As site (not the one already occupied). We denote the surface intermediate formed in this reaction as  $2\parallel\text{As-L}$  and its structure is illustrated in [Figure 6-5 d](#)). The activation energy computed for this reaction is the same as for first ligand transfer, +0.1 eV. The energy gain is the same as for straightforward formation of  $\parallel\text{As-L}_2$ . The surface product features Hf coordinated to two oxygen atoms and two As sites occupied by two ligands. In the second step, both dissociated ligands are transferred to one As site:  $2\parallel\text{As-L} \rightarrow \parallel\text{As-L}_2$ , with no gain in energy. We compute a moderately low barrier for this transition, +0.7 eV ([Figure 6-5](#)).

Further consideration of the path leading to formation of gaseous TDMAAs assumes that the activation energy for transfer of the third ligand from the metal center to an unoccupied As atom is +0.1 eV and from this As site to the occupied As site (crowding on one atom) is +0.7 eV. Computed reaction energies show a gain in energy in each ligand transfer step. The third ligand transfer to an unoccupied As site ( $\parallel\text{As-L}_2 + \text{As-L}$ ) gives -1.8 eV at 0 K and desorption of the formed molecule yields  $\Delta G = -2.9$  eV at 473 K. Structures of the surface intermediates are shown in [Figure 6-4 e](#)) and [f](#)). When the third ligand is transferred to the substrate, the coordination number of Hf to O increases again to four. The formed bonds are between 2.0-2.2 Å long. When  $\text{AsL}_3$  desorbs, the coordination number decreases back to three. In this intermediate, the Hf center is left with one remaining alkylamide ligand. Hf-O bonds are around 2.0 Å long which is consistent with the Hf-O distances in  $\text{HfO}_2$  bulk (~2.1 Å).

The ligand exchange mechanism with no charge transfer is an exothermic process with each mechanistic step being downhill. As mentioned earlier, the driving force is formation of Hf-O bonds and exchanging polar Hf-N with more covalent As-N bonds.

Our arsenolite model can only partially predict the ‘densification’ [145] of the precursor metal center to the surface oxygen. Generally, the coordination number of Hf increases in each ligand transfer step. However, densification is limited by the number of As and O atoms in the *arsenolite* cage and reaches a maximum of four bonds to O for certain geometries ( $\parallel\text{AsL}_2$  and  $\parallel\text{AsL}_2 + \parallel\text{As-L}$ ). This is due to the peculiarity of the molecular solid structure. This does not necessarily affect the energetics, as the gain in energy is obtained regardless of the degree of densification (compare *e.g.*  $\parallel\text{As-L}_2$  with  $2\parallel\text{As-L}$ ).

This mechanism is clearly favored by thermodynamics. Kinetics, however, favors channels that require available Lewis acidic sites in the close neighborhood of the metal center. This is due to the transition state structure that we predict to feature an Hf-N-As link. When not crowded metal surface sites are present within close proximity, we expect that the surface becomes saturated very quickly with  $\parallel\text{As-L}$  groups (Figure 6-4 b, d). At the same time the Hf center densifies to surface oxygen, removing itself from the neighborhood of As sites (Figure 6-4 c, e). Crowding ligands onto one metal center becomes more difficult as Hf densifies, because of the distance between  $\parallel\text{As-L}$  groups (Figure 6-4 d, e). Although the transition from  $2\parallel\text{As-L}$  to  $\parallel\text{As-L}_2$  has an accessible activation energy, our model arsenic oxide cluster becomes highly distorted at the transition state, which is unlikely to occur at the real surface. What is more, the transition from  $\text{AsL}_2$  to  $\text{AsL}_3$  might be even more difficult when the bulky character of the alkylamide ligand is taken into account. An alternative channel is simple exchange of the ligands between two metal atoms, but we showed that this is hampered by a high kinetic barrier, as it also requires distortion of the *arsenolite* cluster at the transition state. Finally, we have to remember that this model supposes an area of the substrate of  $2.5 \text{ nm}^2$  per precursor molecule, which is equivalent to a very low precursor coverage. This gives a lot of space for surface transformations. For comparison, our DFT structures show that

molecularly adsorbed Hf alkylamide precursor occupies an area of just 0.6 nm<sup>2</sup> with two As sites in the close proximity.

## 6.5 CVD reactions

$\beta$ -hydride elimination is a well-known mechanism in the chemistry of metal alkylamides. This mechanism often leads to elimination of amine and imine from an alkylamide molecule, which affects the metal center. A change in the oxidation state of the metal center as a result of ligand interactions is undesirable for the type of ALD considered here and in this sense these reactions are called ‘CVD-type’ hereafter. Two modes of ligand decomposition after molecular adsorption are considered: (i)  $\alpha$ -H exchange in case of dimethylamido ligands and (ii) H diffusion to the III-V substrate. The optimized structures are shown in [Figure 6-6 a\)](#) and [b\)](#) respectively.

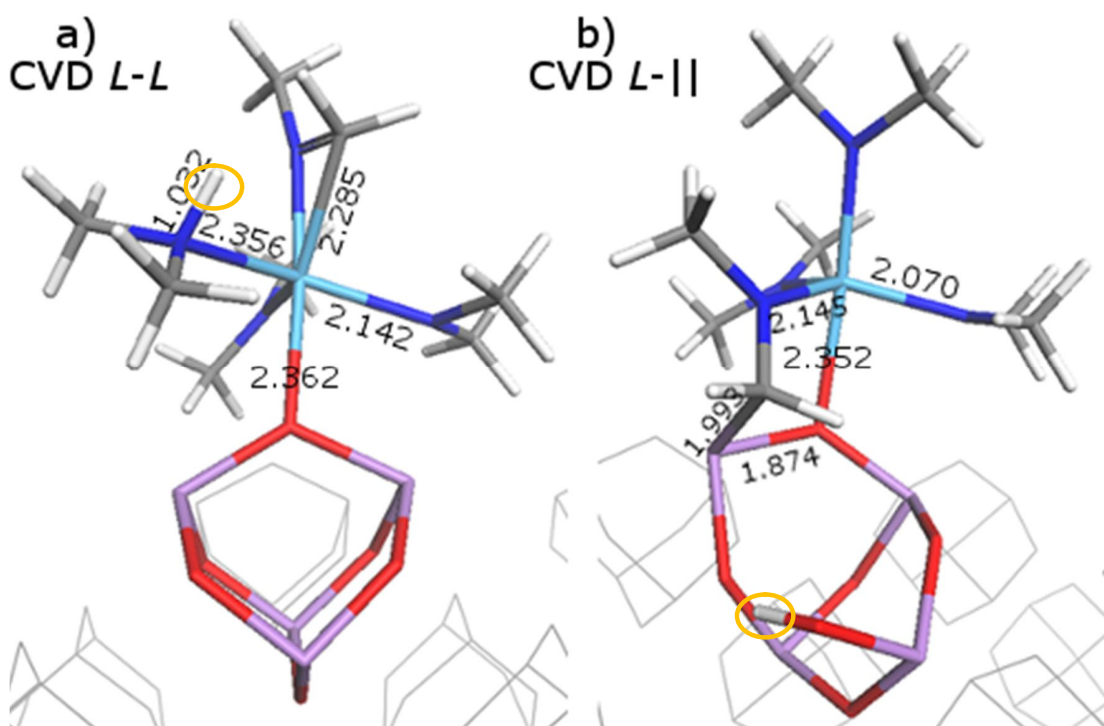


**Figure 6-6** Surface models showing products of H elimination mechanism leading to the decomposition of molecularly adsorbed Hf(NMe<sub>2</sub>)<sub>4</sub> precursor: a) H (highlighted by the orange circle) eliminated from one ligand to another; b) H (highlighted by the orange circle) eliminated from ligand to the As<sub>2</sub>O<sub>3</sub> surface. Stick representation: purple As, red O, white H, gray C, green Cl, blue N, light blue Hf. Selected bond lengths are given in Å. Thin lines show adjacent substrate atoms.

During the ALD metal precursor pulse, we predict that the precursor adsorbs molecularly through the Hf metal center that is attracted by negative charge on oxygen sites (see section 6.3 above). Saturation of the surface with adsorbed precursor molecules can force interaction between bulky ligands. H can be exchanged between two ligands (intramolecularly on the same adsorbate or intermolecularly between neighbouring adsorbates) possibly driven by the formation of amine and imine. For the intramolecular case, we calculate that this process is strongly endothermic with a reaction energy of +1.6 eV relative to the molecular adsorption. [Figure 6-7](#) shows the computed barrier for this reaction of 1.7 eV. Looking at the optimized structure ([Figure 6-6 a](#)), we see that formed species of dimethylamine,  $\text{HNMe}_2$ , and N-methyl methyleneimine,  $\text{CH}_2\text{NMe}$ , are attached to the metal center. The bond between amine moiety and metal center is around 7% longer compared to the Hf-N bond in the gaseous precursor, meaning that the lone pair of electrons on N is more weakly stabilized by  $p\pi-d\pi$  overlap. Additionally C in the  $\text{CH}_2$  group of the imine moiety is attracted by Hf, forming a bond of 2.3 Å. Bader analysis indicates that the charge released during proton diffusion from one ligand to another is accommodated on Hf, N of the amine species and C of the  $\text{CH}_2$  group.

In the second example we consider proton diffusion from the adsorbed precursor to the III-V substrate. The oxidised III-V substrate can store protons in the form of hydroxyl groups. The DFT  $\Delta E$  for this type of process is moderately endothermic, +0.2 eV. However this process is kinetically hampered; we compute +1.1 eV of activation energy for this reaction pathway ([Figure 6-7](#)). The relaxed structure pictured in [Figure 6-6 b](#) shows that the N-methyl methylenimido ion is attached through N to the Hf center and is bound through C with the III-V metal (As). The mechanism for this type of process was described in detail in section 5.5.1. The high activation energy is a consequence of the unfavorable structure of the transition state. We find that the transition from dimethylamido ligand to N-methyl methylenimido ion goes through a configuration in



which N is tricoordinated, featuring an N=C double bond. Taking part in the reaction As becomes under-coordinated, losing one bond to O. This activation energy depends only on the strength of the III-V metal – oxygen bond, and can be expected to be higher for other III-V's.

Desorption of neutral species formed in the H elimination mechanism, amine and imine, would cause charge transfer and therefore reduction of the metal center of the precursor. Reductive elimination in amido metal complexes was reported by Zaera's group. Their thermal decomposition experiments identify the threshold for thermal conversion of the vapor of dialkylamido compounds between 300 and 500 K and several products including amines, imines and hydrazines [146]. Our DFT study shows that these reactions are quite inaccessible, at least at low temperature on a III-V substrate.

An alternative to reduction of the metal center is densification of the Hf to nearby O, along with reduction of a substrate oxide. This would be facilitated by desorption of ligands from Hf. In the case of desorption of amine and imine from the surface intermediate shown in [Figure 6-6 a](#)), followed by coordination of Hf to three O atoms and formation of an As-As bond, we calculate a substantial gain in energy of -1.8 eV relative to the reaction energy for CVD *L-L*. However, this process is not spontaneous. It seems that Hf densification is triggered by a mechanism in which Hf is under-coordinated or the coordination sphere around Hf is open and not completely surrounded by attached groups. Such situations are easily obtained, *e.g.* when one of the ligands is transferred to the surface. In the next section we consider the kinetics of decomposition of alkylamide ligands in direct contact with the substrate and at a stage where the precursor center is already densified.

## 6.6 Secondary decomposition surface reactions

Since CVD reactions do not affect the III-V substrate in a direct way, we consider the same types of mechanisms but occurring directly on the substrate. We focus on H elimination pathways leading to the most thermodynamically favorable reduction of the native oxide. As shown in previous chapter 5, scission of the N-C bond can also be feasible, but scission of the C-H bond was shown to be the most exothermic. Generation of by-products like N-methyl methyleneimine (MMI) or ethylene imine (aziridine) releases charge to the substrate. The reaction profile in [Figure 6-7](#) shows computed barriers for the pathway leading to formation and desorption of the MMI molecule. The surface intermediates formed along this process are illustrated in [Figure 6-8](#).

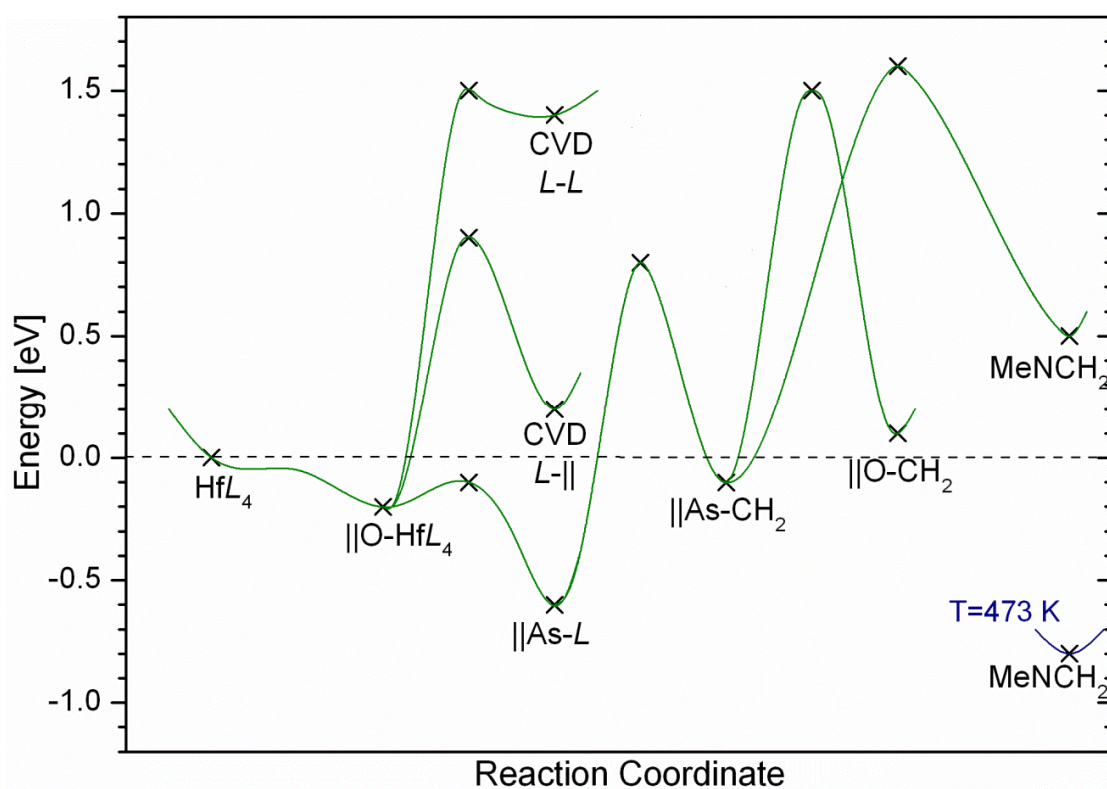


**Figure 6-7** Reaction profile for decomposition of dimethylamide ligand,  $L = [\text{NMe}_2]$ , from  $\text{HfL}_4$  adsorbed at the bare arsenolite- $\text{As}_2\text{O}_3$  surface,  $\text{||O-HfL}_4$ . The zero of energy is precursor in the gas phase and bare surface. DFT energetics of the transformations are computed at 0 K and desorption of  $\text{MeNCH}_2$  product is corrected with the entropy computed at 473 K. The black crosses mark relative energies of optimized stationary points (either minimums of the structures shown in [Figure 6-6](#) and [Figure 6-8](#) or saddle points of transition states). The solid lines indicate possible reaction pathways that link these points.

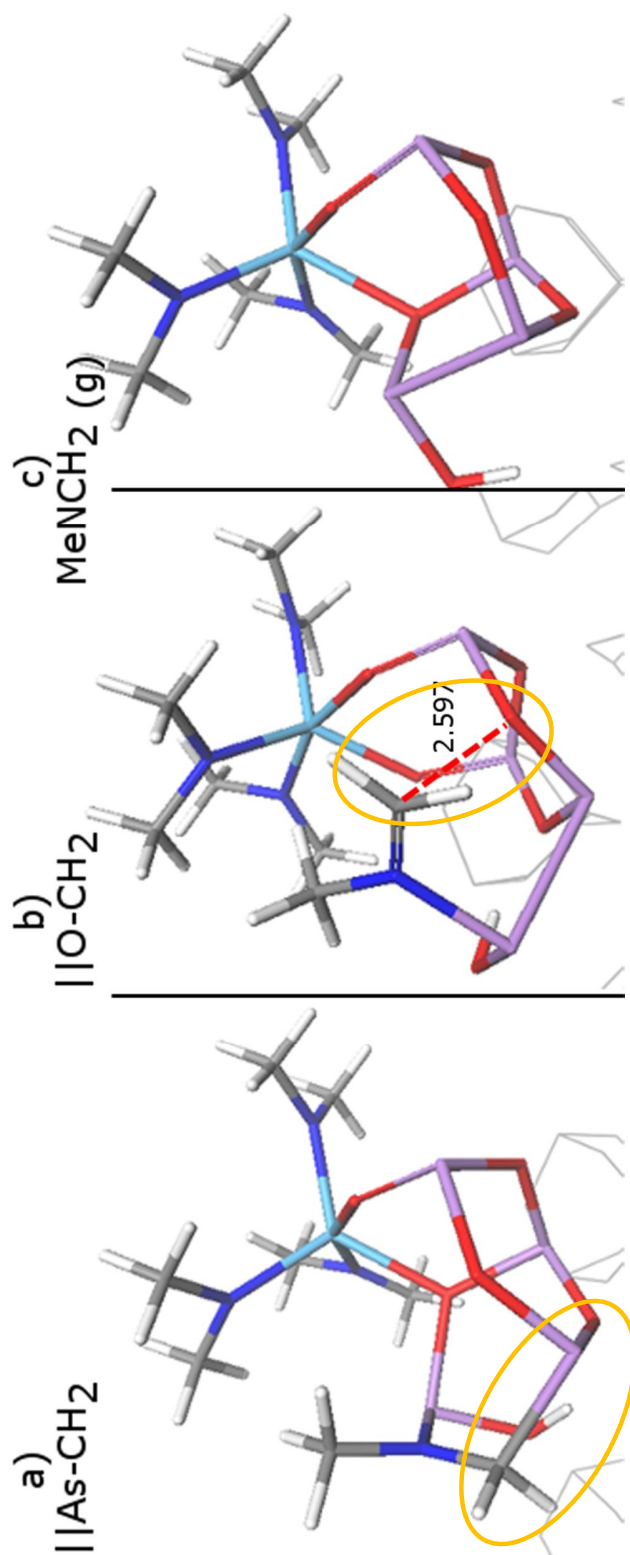


Figure 6-8 Surface models showing products of the interaction of dimethylamide ligand,  $[\text{NMe}_2]$ , with bare *arsenolite*- $\text{As}_2\text{O}_3$  surface: a) H elimination from the ligand to the surface; b) migration of  $\text{CH}_2$  moiety from an As to an O site; c) product of desorption of N-methyl methyleneimine,  $\text{MeNCH}_2$ . Stick representation: purple As, red O, white H, gray C, green Cl, blue N, light blue Hf. Thin lines show adjacent substrate atoms.

Formation and subsequent desorption of MMI requires a reorganization in the electronic density with the formation of an N=C double bond and breaking As-N and As-C bonds. Simultaneously, charge transfer to the surface As occurs and an As-As metallic bond appears for each formation of MMI. Although formation of  $\parallel\text{As-CH}_2$  (Figure 6-8 a) is energetically uphill from migration of the ligand to the substrate ( $\parallel\text{As-L}$ ), it is exothermic with respect to the separated precursor and the surface. Proceeding from  $\parallel\text{As-CH}_2$ , breaking As-C and forming an N=C double bond, which we denote as  $\parallel\text{O-CH}_2$  (surface species shown in Figure 6-8 b) is slightly uphill, with  $\Delta E^{0K} = +0.1$  eV. We view this transformation as reductive migration of decomposition intermediates from the As to the O site, similar to the migration of the methyl group in the case of TMA (chapter 3) [131]. Desorption of the MMI molecule gives a gain in energy of -0.8 eV at 473 K relative to the precursor in the gas phase and the surface product is illustrated in Figure 6-8 c). The computed kinetic barrier for the first step of this process, H elimination to the surface O and formation of  $\parallel\text{As-CH}_2$ , is of the same magnitude as for the formation of the CVD  $L-\parallel$  intermediate, around 1.4 eV. In the next step we predict either creation of an N=C double bond and subsequent charge transfer, or desorption of imine also resulting in charge transfer. The reaction profile in Figure 6-7 shows a similar, considerable activation energy of around 1.6 eV for those transformations.

The reaction barrier for H elimination seems to be independent of the geometry. Whether the ligand is attached to the precursor metal center or substrate metal, N is tricoordinated, featuring the N=C double bond and the substrate metal is under-coordinated at the transition state. Similarly, charge transfer reactions require transitions through configurations featuring under-coordinated surface metal sites. Therefore, these are kinetically demanding. However, due to the densification process of the precursor metal center to the native oxygen in the substrate, III-V metal - oxygen bonds can be

weakened. This might substantially facilitate ligand interaction with surface metal sites. Nevertheless, our model predicts that decomposition reactions of ligands at the surface and the associated charge transfer reactions are thermodynamically exothermic or neutral processes, but that there are considerable kinetic requirements that may impede occurrence of these processes at low temperature. Indeed, it has been shown experimentally that elevating the temperature of the process significantly enhances the clean-up abilities of alkylamides [60]. As shown in [Figure 6-1](#) (page 111), formation of MMI along with arsine in reaction (3) requires temperature activation but already at room temperature becomes more exothermic than the ligand exchange reaction (1).

## 6.7 Conclusion

This study sheds light on the mechanisms occurring during initial cycles of the atomic layer deposition of hafnium oxide films on an oxidized III-V substrate. DFT calculations were carried out on bulk structures, gas phase molecules and slab models of representing native oxide surface (010) *arsenolite*-As<sub>2</sub>O<sub>3</sub>. Bulk reaction energies were obtained for candidate processes achieving the clean-up effect and this indicated which processes are favoured overall. Quantitative structures and energetics along the reaction pathways were also obtained in order to investigate the actual mechanisms occurring on the native oxide surface.

Through investigation of bulk potential energies we proved that tetrakis(dimethylamido)hafnium is a clean-up reagent. The variety and number of possible by-products was exposed in a number of exothermic processes. Metallic arsenic turns out to be the most favorable form of arsenic products, which agrees with the experimental observations of accumulation of metallic arsenic and arsenic suboxide at the interface during alkylamide-based ALD [59, 64]. The most exothermic reaction is transformation of dimethylamide ligand into molecular nitrogen, methane and ethene.

While production of oxygen during clean-up is thermodynamically accessible, formation of nitrogen oxides is endothermic.

Surrounded by dimethylamide ligands, the Hf centre in the precursor is a poor Lewis acid and adsorbs weakly onto the native oxide surface. Densification of this Hf atom to the substrate oxygen was shown to be crucial. Densification is activated by a mechanism in which Hf is under-coordinated or the coordination sphere around Hf is open and not completely surrounded by attached groups. Therefore, on the bare native oxide surface Hf increases its Lewis acidity when ligands migrate away from it to the surface. We showed that migration of the entire alkylamide ligand to the O site is thermodynamically and kinetically inaccessible. Therefore, oxidation of alkylamide as an intact unit is not an important redox channel. Instead, the thermodynamics are clearly in favor of the migration of the ligand to the As site. The kinetics favors channels where there are unhindered Lewis acidic sites in the close neighborhood of the Hf center. If the surface is highly under-saturated, then ligand exchange from Hf to As is predicted to proceed very quickly. Crowding ligands onto one As center though becomes more difficult as Hf densifies. Therefore, steric hindrance is an obstacle, difficult to overcome, for this type of mechanism.

Our model predicts that some ligand decomposition reactions and charge transfer reactions are thermodynamically exothermic or neutral processes, but that there are considerable kinetic requirements that may impede occurrence of these processes at low temperature. Processes in which products like imine or aziridine are formed can be thus controlled depending on the temperature.

## 7 Summary and Suggestions for Further Work

In this thesis we have presented theoretical investigation of nucleation during the incubation period of ALD of dielectric thin films on technologically important substrates: III-V semiconductors and silicon nitride.

Atomic-scale simulations in the framework of DFT were conducted on the bulk structures, surface models and gas phase molecules. *Ab initio* thermodynamics provided a bridge between zero-temperature, zero-pressure DFT and real experiments. We have analysed and described the interaction of the precursors with the considered substrates: starting from initial adsorption of the gaseous molecule, through its transformation in contact with native oxides, until formation of surface intermediates that can be lost as by-products. The structure and chemical state of surface intermediates were described in detailed. Some kinetic aspects of the incubation mechanisms were also revealed. Based on the trends arising from the initial computations, we have developed a comprehensive model that allows us to compare the operation of different classes of precursor chemicals and assess their properties for self-cleaning ALD.

On the example of TMA we identified two separate factors governing the clean-up effect: formation of the metal oxide as the driving force and affinity of the precursor ligand to the III-V oxide substrate as the ancillary force. 'Clean-up' of an oxide film is shown to strongly depend on the electropositivity of the precursor metal, and thus always results in formation of dielectric film from native oxide. However, self-cleaning ALD does not necessary result in substrate-enhanced growth, as the clean-up effect can be spread over a few cycles. The choice of ligand determines bonding at the interface and the overall type of clean-up. The predominant pathway for a metalloid oxide such as arsenic oxide is reduction, producing volatile molecules or gettering oxygen from less reducible oxides. An alternative pathway is non-redox ligand exchange, which allows non-reducible oxides to be cleaned-up.

TMA was shown to be a superior precursor for self-cleaning ALD, considering the good properties of  $\text{Al}_2\text{O}_3$  film as an interfacial layer in the transistor gate stack. Thanks to the lability of the methyl ligand that has affinity to both Lewis basic and acidic sites, a number of mechanisms are exothermic and competitive. We proposed TMA clean-up by-products, interface bonding and the most thermodynamically abundant surface intermediates.

TDMAH was shown to have slightly different properties to TMA. However we proved that this precursor is also a clean-up reagent, with a number of exothermic reactions participating. The dimethylamide ligand was shown to be resistant to oxidation when intact, however very prone to decomposition and subsequent oxidation. Some of the decomposition intermediates can migrate from Lewis acidic to Lewis basic site as in the TMA case. What is characteristic in the operation of alkylamide precursors is that their self-cleaning behaviour is increased with temperature and results in accumulation of As suboxides at the interface. Our kinetics study has revealed the reason for source of this behaviour.

In general, we predict that the investigated methyl precursors are the best reagents for deposition of dielectrics and performing clean-up. Unfortunately, most of them are very unstable compounds. Having identified Mg precursors as the most effective at clean-up, one possible avenue for future research would be to evaluate the performance of some specific Mg precursor molecules on III-V surfaces. For instance,  $\text{Mg}(\text{C}_5\text{H}_5)_2$  is a commonly-used precursor in ALD [147]. It would be interesting to look in particular at whether this precursor too can carry out 'clean-up' and improve the electrical properties of the interface. Our study showed also that the chloride family cannot act according to the same mechanisms as organometallic and metalorganic precursors, but according to different mechanisms resulting in self-cleaning ALD that could also be investigated further.



Successful ALD relies on growth reactions being faster than side-reactions. For these reasons, calculating the kinetics of self-cleaning ALD reactions could contribute to the research in this subject. However, DFT is not suitable for cases where detailed treatment of electron correlation is necessary. This includes some types of transition state (TS) that we study within this thesis to evaluate the kinetics of the ‘clean-up’ effect. Therefore, it would be profitable in the future to benchmark the DFT barriers reported here against more accurate calculations. The eigenvalue-following Trust Radius Image Minimization algorithm provides more accurate geometries and energetics of transition states. These geometries, at the DFT level, can be used as an input for the computationally-heavy configuration interaction (CI) calculations that account for electron correlation more completely than DFT and yield high-quality energy. It is worth mentioning that the heterodeposition (deposition on the initial substrate) mechanisms investigated here could serve as an input to the multi-scale simulation, *e.g.* kinetic Monte Carlo [148], of the actual film growth corresponding to an experimental timescale.

The major aim of this thesis was to assist and to complement experiment and as a result to obtain better understanding of the mechanisms occurring during initial ALD cycles of dielectric films. This goal was definitely achieved. Some of the suggested here mechanisms were subsequently confirmed, in the case of TMA clean-up by Tallarida and co-workers, while other mechanisms provided explanations for prior experimental findings, in the case of alkylamides by Gougousi and co-workers. What is more, the clean-up by products reported here may be detectable with, *e.g.* FTIR or mass spectrometry experiments of sufficient surface sensitivity. Our calculations assisted analysis of the growth details on silicon nitride substrates. Theoretical calculations accounted for the different starting substrates and provided possible explanations for the experimentally-revealed anomalous growth step.

## Bibliography

1. Semiconductor Industry Association (SIA): <http://www.semiconductors.org/>.
2. Wilk, G.D., R.M. Wallace, and J.M. Anthony, *High-kappa gate dielectrics: Current status and materials properties considerations*. Journal of Applied Physics, 2001. 89(10): p. 5243-5275.
3. Wu, Y. and G. Lucovsky, *Ultrathin nitride/oxide (N/O) gate dielectrics for p/sup +/-polysilicon gated PMOSFETs prepared by a combined remote plasma enhanced CVD/thermal oxidation process*. Electron Device Letters, IEEE, 1998. 19(10): p. 367-369.
4. Lin, L. and J. Robertson, *Defect states at III-V semiconductor oxide interfaces*. Appl. Phys. Lett., 2011. 98(8): p. 082903.
5. Spicer, W.E., et al., *Unified Mechanism for Schottky-Barrier Formation and III-V Oxide Interface States*. Physical Review Letters, 1980. 44(6): p. 420.
6. Hasegawa, H., et al., *Electronic and microstructural properties of disorder-induced gap states at compound semiconductor--insulator interfaces*. Journal of Vacuum Science & Technology B: Microelectronics and Nanometer Structures, 1987. 5(4): p. 1097-1107.
7. Spicer, W.E., et al., *The advanced unified defect model for Schottky barrier formation*. Journal of Vacuum Science & Technology B: Microelectronics and Nanometer Structures, 1988. 6(4): p. 1245-1251.
8. Ye, P.D., *Main determinants for III--V metal-oxide-semiconductor field-effect transistors (invited)*. Journal of Vacuum Science & Technology A: Vacuum, Surfaces, and Films, 2008. 26: p. 697-704.
9. Frank, M.M., et al., *HfO<sub>2</sub> and Al<sub>2</sub>O<sub>3</sub> gate dielectrics on GaAs grown by atomic layer deposition*. Applied Physics Letters, 2005. 86(15): p. 152904-3.
10. Milojevic, M., et al., *Half-cycle atomic layer deposition reaction studies of Al<sub>2</sub>O<sub>3</sub> on In<sub>0.2</sub>Ga<sub>0.8</sub>As (100) surfaces*. Applied Physics Letters, 2008. 93(20): p. 202902-3.
11. Hinkle, C.L., et al., *GaAs interfacial self-cleaning by atomic layer deposition*. Applied Physics Letters, 2008. 92(7): p. 071901-3.
12. Hinkle, C.L., et al., *Frequency dispersion reduction and bond conversion on n-type GaAs by in situ surface oxide removal and passivation*. Applied Physics Letters, 2007. 91(16): p. 163512-3.

13. George, S.M., *Atomic Layer Deposition: An Overview*. Chemical Reviews, 2009. 110(1): p. 111-131.
14. Suntola, T., *Atomic layer epitaxy*. Materials Science Reports, 1989. 4(5): p. 261-312.
15. Aleskovskii, V.B., *Chemistry and technology of solids*. Journal of Applied Chemistry of the USSR, 1974. 47(10): p. 2207-2217.
16. Kim, H., *Atomic layer deposition of metal and nitride thin films: Current research efforts and applications for semiconductor device processing*. Journal of Vacuum Science & Technology B: Microelectronics and Nanometer Structures, 2003. 21(6): p. 2231-2261.
17. Kim, J. and T. Kim, *Initial surface reactions of atomic layer deposition*. JOM Journal of the Minerals, Metals and Materials Society, 2009. 61(6): p. 17-22.
18. Puurunen, R.L., *Surface chemistry of atomic layer deposition: A case study for the trimethylaluminum/water process*. Journal of Applied Physics, 2005. 97(12): p. 121301-52.
19. Higashi, G.S. and C.G. Fleming, *Sequential surface chemical reaction limited growth of high quality Al<sub>2</sub>O<sub>3</sub> dielectrics*. Applied Physics Letters, 1989. 55(19): p. 1963-1965.
20. Dillon, A.C., et al., *Surface chemistry of Al<sub>2</sub>O<sub>3</sub> deposition using Al(CH<sub>3</sub>)<sub>3</sub> and H<sub>2</sub>O in a binary reaction sequence*. Surface Science, 1995. 322(1-3): p. 230-242.
21. Langereis, E., et al., *In situ spectroscopic ellipsometry study on the growth of ultrathin TiN films by plasma-assisted atomic layer deposition*. Journal of Applied Physics, 2006. 100(2): p. 023534-10.
22. Delabie, A., et al., *Atomic layer deposition of hafnium oxide on germanium substrates*. Journal of Applied Physics, 2005. 97(6): p. 064104-10.
23. Dolgushev, N.V., et al., *Synthesis and characterization of nanosized titanium oxide films on the (0001)  $\alpha$ -Al<sub>2</sub>O<sub>3</sub> surface*. Thin Solid Films, 1997. 293(1-2): p. 91-95.
24. Niinistö, L., et al., *Advanced electronic and optoelectronic materials by Atomic Layer Deposition: An overview with special emphasis on recent progress in processing of high-k dielectrics and other oxide materials*. physica status solidi (a), 2004. 201(7): p. 1443-1452.
25. Ando, T., *Ultimate Scaling of High- $\kappa$  Gate Dielectrics: Higher- $\kappa$  or Interfacial Layer Scavenging?* Materials, 2012. 5(3): p. 478-500.

26. Ylilammi, M., *Monolayer thickness in atomic layer deposition*. Thin Solid Films, 1996. 279: p. 124-130.
27. Putkonen, M., M. Nieminen, and L. Niinistö, *Magnesium aluminate thin films by atomic layer deposition from organometallic precursors and water*. Thin Solid Films, 2004. 466(1–2): p. 103-107.
28. Ott, A.W., et al., *Al<sub>3</sub>O<sub>3</sub> thin film growth on Si(100) using binary reaction sequence chemistry*. Thin Solid Films, 1997. 292(1–2): p. 135-144.
29. Groner, M.D., et al., *Electrical characterization of thin Al<sub>2</sub>O<sub>3</sub> films grown by atomic layer deposition on silicon and various metal substrates*. Thin Solid Films, 2002. 413(1–2): p. 186-197.
30. Puurunen, R.L., et al., *Island growth in the atomic layer deposition of zirconium oxide and aluminum oxide on hydrogen-terminated silicon: Growth mode modeling and transmission electron microscopy*. Journal of Applied Physics, 2004. 96(9): p. 4878-4889.
31. Puurunen, R.L., et al., *Successive reactions of gaseous trimethylaluminium and ammonia on porous alumina*. Physical Chemistry Chemical Physics, 2001. 3(6): p. 1093-1102.
32. Yeddanapalli, L.M. and C.C. Schubert, *Thermal and Photochemical Decomposition of Gaseous Aluminum Trimethyl*. The Journal of Chemical Physics, 1946. 14(1): p. 1-7.
33. Lakomaa, E.L., A. Root, and T. Suntola, *Surface reactions in Al<sub>2</sub>O<sub>3</sub> growth from trimethylaluminium and water by atomic layer epitaxy*. Applied Surface Science, 1996. 107(0): p. 107-115.
34. Putkonen, M., et al., *ZrO<sub>2</sub> Thin Films Grown on Silicon Substrates by Atomic Layer Deposition with Cp<sub>2</sub>Zr(CH<sub>3</sub>)<sub>2</sub> and Water as Precursors*. Chemical Vapor Deposition, 2003. 9(4): p. 207-212.
35. Niinisto, J., et al., *Controlled growth of HfO<sub>2</sub> thin films by atomic layer deposition from cyclopentadienyl-type precursor and water*. Journal of Materials Chemistry, 2005. 15(23): p. 2271-2275.
36. Niinistö, J., et al., *Atomic Layer Deposition of HfO<sub>2</sub> Thin Films Exploiting Novel Cyclopentadienyl Precursors at High Temperatures*. Chemistry of Materials, 2007. 19(13): p. 3319-3324.

37. Green, M.L., et al., *Nucleation and growth of atomic layer deposited HfO<sub>2</sub> gate dielectric layers on chemical oxide (Si--O--H) and thermal oxide (SiO<sub>2</sub> or Si--O--N) underlayers*. Journal of Applied Physics, 2002. 92(12): p. 7168-7174.
38. Puurunen, R.L., *Analysis of hydroxyl group controlled atomic layer deposition of hafnium dioxide from hafnium tetrachloride and water*. Journal of Applied Physics, 2004. 95(9): p. 4777-4786.
39. Elers, K.-E., et al., *NbCl<sub>5</sub> as a precursor in atomic layer epitaxy*. Applied Surface Science, 1994. 82–83(0): p. 468-474.
40. Kukli, K., et al., *Atomic Layer Deposition of Tantalum Oxide Thin Films from Iodide Precursor*. Chemistry of Materials, 2000. 13(1): p. 122-128.
41. Kukli, K., et al., *Effect of selected atomic layer deposition parameters on the structure and dielectric properties of hafnium oxide films*. Journal of Applied Physics, 2004. 96(9): p. 5298-5307.
42. Kukli, K., et al., *Comparison of hafnium oxide films grown by atomic layer deposition from iodide and chloride precursors*. Thin Solid Films, 2002. 416(1–2): p. 72-79.
43. Gusev, E.P., et al., *Ultrathin HfO<sub>2</sub> films grown on silicon by atomic layer deposition for advanced gate dielectrics applications*. Microelectronic Engineering, 2003. 69(2–4): p. 145-151.
44. Campbell, S.A., et al., *MOSFET transistors fabricated with high permittivity TiO<sub>2</sub> dielectrics*. Electron Devices, IEEE Transactions on, 1997. 44(1): p. 104-109.
45. Gordon, R.G., et al., *Vapor Deposition of Metal Oxides and Silicates: Possible Gate Insulators for Future Microelectronics*. Chemistry of Materials, 2001. 13(8): p. 2463-2464.
46. Hausmann, D.M., et al., *Atomic Layer Deposition of Hafnium and Zirconium Oxides Using Metal Amide Precursors*. Chemistry of Materials, 2002. 14(10): p. 4350-4358.
47. Min, J.-S., H.-S. Park, and S.-W. Kang, *Metal--organic atomic-layer deposition of titanium--silicon--nitride films*. Applied Physics Letters, 1999. 75(11): p. 1521-1523.
48. Lim, J.-W., J.-S. Park, and S.-W. Kang, *Kinetic modeling of film growth rates of TiN films in atomic layer deposition*. Journal of Applied Physics, 2000. 87(9): p. 4632-4634.

49. Elam, J.W., et al., *Surface chemistry and film growth during TiN atomic layer deposition using TDMAT and NH<sub>3</sub>*. Thin Solid Films, 2003. 436(2): p. 145-156.
50. Kim, D.-J., et al., *Applicability of ALE TiN films as Cu/Si diffusion barriers*. Thin Solid Films, 2000. 372(1-2): p. 276-283.
51. Wada, S., et al., *Recent Development of ALD Precursors for Semiconductor Devices*. ECS Transactions, 2009. 25(4): p. 209-216.
52. Becker, J.S., E. Kim, and R.G. Gordon, *Atomic Layer Deposition of Insulating Hafnium and Zirconium Nitrides*. Chemistry of Materials, 2004. 16(18): p. 3497-3501.
53. Zaera, F., *The surface chemistry of thin film atomic layer deposition (ALD) processes for electronic device manufacturing*. Journal of Materials Chemistry, 2008. 18(30): p. 3521-3526.
54. Kukli, K., et al., *Atomic Layer Deposition of Hafnium Dioxide Films from Hafnium Tetrakis(ethylmethanamide) and Water*. Chemical Vapor Deposition, 2002. 8(5): p. 199-204.
55. Huang, M.L., et al., *Surface passivation of III-V compound semiconductors using atomic-layer-deposition-grown Al<sub>2</sub>O<sub>3</sub>*. Applied Physics Letters, 2005. 87(25): p. 252104-3.
56. Chang, C.H., et al., *Interfacial self-cleaning in atomic layer deposition of HfO<sub>2</sub> gate dielectric on In<sub>0.15</sub>Ga<sub>0.85</sub>As*. Applied Physics Letters, 2006. 89(24): p. 242911-3.
57. Delabie, A., et al., *Atomic Layer Deposition of Hafnium Oxide on Ge and GaAs Substrates: Precursors and Surface Preparation*. Journal of The Electrochemical Society, 2008. 155(12): p. H937-H944.
58. Granados-Alpizar, B. and A.J. Muscat, *Surface reactions of TiCl<sub>4</sub> and Al(CH<sub>3</sub>)<sub>3</sub> on GaAs(100) during the first half-cycle of atomic layer deposition*. Surface Science, 2011. 605(13-14): p. 1243-1248.
59. Gougousi, T. and J.W. Lacin, *Native oxide consumption during the atomic layer deposition of TiO<sub>2</sub> films on GaAs (100) surfaces*. Thin Solid Films, 2010. 518(8): p. 2006-2009.
60. Gougousi, T. and L. Ye, *Interface Between Atomic Layer Deposition Ta<sub>2</sub>O<sub>5</sub> Films and GaAs(100) Surfaces*. The Journal of Physical Chemistry C, 2012. 116(16): p. 8924-8931.

61. Milojevic, M., et al., *Half-cycle atomic layer deposition reaction studies of Al<sub>2</sub>O<sub>3</sub> on (NH<sub>4</sub>)<sub>2</sub>S passivated GaAs(100) surfaces*. Applied Physics Letters, 2008. 93(25): p. 252905-3.
62. Lee, H.D., et al., *Reduction of native oxides on GaAs during atomic layer growth of Al<sub>2</sub>O<sub>3</sub>*. Applied Physics Letters, 2009. 94(22): p. 222108-3.
63. Tallarida, M., et al., *Surface chemistry and Fermi level movement during the self-cleaning of GaAs by trimethyl-aluminum*. Applied Physics Letters, 2011. 99(4): p. 042906.
64. Gougousi, T., et al., *Growth and Interface Evolution of HfO<sub>2</sub> Films on GaAs(100) Surfaces*. Journal of The Electrochemical Society, 2010. 157(5): p. H551-H556.
65. Finnie, C.M., X. Li, and P.W. Bohn, *Production and evolution of composition, morphology, and luminescence of microcrystalline arsenic oxides produced during the anodic processing of (100) GaAs*. Journal of Applied Physics, 1999. 86(9): p. 4997-5003.
66. Suri, R., D.J. Lichtenwalner, and V. Misra, *Interfacial self cleaning during atomic layer deposition and annealing of HfO<sub>2</sub> films on native (100)-GaAs substrates*. Applied Physics Letters, 2010. 96(11): p. 112905-3.
67. O'Mahony, A., et al., *Structural and electrical analysis of the atomic layer deposition of HfO<sub>2</sub>/n-In<sub>0.53</sub>Ga<sub>0.47</sub>As capacitors with and without an Al<sub>2</sub>O<sub>3</sub> interface control layer*. Applied Physics Letters, 2010. 97(5): p. 052904-3.
68. Kohn, W. and L.J. Sham, *Self-Consistent Equations Including Exchange and Correlation Effects*. Physical Review, 1965. 140(4A): p. A1133-A1138.
69. Johnson, B.G., P.M.W. Gill, and J.A. Pople, *The performance of a family of density functional methods*. The Journal of Chemical Physics, 1993. 98(7): p. 5612-5626.
70. Perdew, J.P., et al., *Atoms, molecules, solids, and surfaces: Applications of the generalized gradient approximation for exchange and correlation*. Physical Review B, 1992. 46(11): p. 6671.
71. Møller, C. and M.S. Plesset, *Note on an Approximation Treatment for Many-Electron Systems*. Physical Review, 1934. 46(7): p. 618-622.
72. Andersson, K., P.-A. Malmqvist, and B.O. Roos, *Second-order perturbation theory with a complete active space self-consistent field reference function*. The Journal of Chemical Physics, 1992. 96(2): p. 1218-1226.

73. Cizek, J., *On the Correlation Problem in Atomic and Molecular Systems. Calculation of Wavefunction Components in Ursell-Type Expansion Using Quantum-Field Theoretical Methods*. The Journal of Chemical Physics, 1966. 45(11): p. 4256-4266.
74. Aquilante, F., et al., *MOLCAS 7: The Next Generation*. Journal of Computational Chemistry, 2010. 31(1): p. 224-247.
75. Werner, H.-J., et al., *Molpro: a general-purpose quantum chemistry program package*. Wiley Interdisciplinary Reviews: Computational Molecular Science, 2012. 2(2): p. 242-253.
76. Roos, B.O., et al., *Main Group Atoms and Dimers Studied with a New Relativistic ANO Basis Set*. The Journal of Physical Chemistry A, 2003. 108(15): p. 2851-2858.
77. Woon, D.E. and J.T.H. Dunning, *Gaussian basis sets for use in correlated molecular calculations. III. The atoms aluminum through argon*. The Journal of Chemical Physics, 1993. 98(2): p. 1358-1371.
78. Dunning, J.T.H., *Gaussian basis sets for use in correlated molecular calculations. I. The atoms boron through neon and hydrogen*. The Journal of Chemical Physics, 1989. 90(2): p. 1007-1023.
79. Kresse, G. and J. Furthmüller, *Efficient iterative schemes for ab initio total-energy calculations using a plane-wave basis set*. Physical Review B, 1996. 54(16): p. 11169.
80. Vanderbilt, D., *Soft self-consistent pseudopotentials in a generalized eigenvalue formalism*. Physical Review B, 1990. 41(11): p. 7892.
81. Kresse, G. and J. Hafner, *Norm-conserving and ultrasoft pseudopotentials for first-row and transition elements*. Journal of Physics: Condensed Matter, 1994. 6(40): p. 8245.
82. Wyckoff, R.W.G., *Crystal Structures*. Crystal Structures, Wiley Interscience, New York, 1963.
83. Quagliano, L.G., *Detection of As<sub>2</sub>O<sub>3</sub> arsenic oxide on GaAs surface by Raman scattering*. Applied Surface Science, 2000. 153(4): p. 240-244.
84. Rojas-Lopez, M., et al., *Raman study of luminescent spark processed porous GaAs*. Journal of Vacuum Science & Technology B: Microelectronics and Nanometer Structures, 2001. 19(3): p. 622-627.



85. Ballirano, P. and A.Z. Maras, *Refinement of the crystal structure of arsenolite, As<sub>2</sub>O<sub>3</sub>*. Kristallogr.-New Cryst. Struct., 2002. 217: p. 177-178.
86. Gibbs, G.V., et al., *Role of Directed van der Waals Bonded Interactions in the Determination of the Structures of Molecular Arsenate Solids*. The Journal of Physical Chemistry A, 2009. 113(4): p. 736-749.
87. Tsuzuki, S. and H.P. Luthi, *Interaction energies of van der Waals and hydrogen bonded systems calculated using density functional theory: Assessing the PW91 model*. The Journal of Chemical Physics, 2001. 114(9): p. 3949-3957.
88. Rydberg, H., et al., *Van der Waals Density Functional for Layered Structures*. Physical Review Letters, 2003. 91(12): p. 126402.
89. Jensen, J.O., et al., *A theoretical study of As<sub>4</sub>O<sub>6</sub>: vibrational analysis, infrared and Raman spectra*. Journal of Molecular Structure: THEOCHEM, 2003. 664-665: p. 145-156.
90. Chrissanthopoulos, A. and C. Pouchan, *A density functional investigation of the structural and vibrational properties of the highly symmetric molecules M<sub>4</sub>O<sub>6</sub>, M<sub>4</sub>O<sub>10</sub> (M = P, As, Sb, Bi)*. Vibrational Spectroscopy, 2008. 48(1): p. 135-141.
91. Fiorentini, V. and M. Methfessel, *Extracting convergent surface energies from slab calculations*. Journal of Physics: Condensed Matter, 1996. 8(36): p. 6525.
92. Ganduglia-Pirovano, M.V. and J. Sauer, *Stability of reduced V<sub>2</sub>O<sub>5</sub> ( 001 ) surfaces*. Physical Review B, 2004. 70(4): p. 045422.
93. Reuter, K. and M. Scheffler, *Composition, structure, and stability of RuO<sub>2</sub> (110) as a function of oxygen pressure*. Physical Review B, 2001. 65(3): p. 035406.
94. Stull, D.R. and H. Prophet, *JANAF Thermodynamical Tables, 2nd ed.* U.S. National Bureau of Standards, Washington, D.C., 1971.
95. Ahlrichs, R., et al., *Electronic structure calculations on workstation computers: The program system turbomole*. Chemical Physics Letters, 1989. 162(3): p. 165-169.
96. Weigend, F. and R. Ahlrichs, *Balanced basis sets of split valence, triple zeta valence and quadruple zeta valence quality for H to Rn: Design and assessment of accuracy*. Physical Chemistry Chemical Physics, 2005. 7(18): p. 3297-3305.
97. Perdew, J.P., K. Burke, and M. Ernzerhof, *Generalized Gradient Approximation Made Simple*. Physical Review Letters, 1996. 77(18): p. 3865.

98. Eichkorn, K., et al., *Auxiliary basis sets to approximate Coulomb potentials (Chem. Phys. Letters 240 (1995) 283)*. Chemical Physics Letters, 1995. 242(6): p. 652-660.
99. Eichkorn, K., et al., *Auxiliary basis sets for main row atoms and transition metals and their use to approximate Coulomb potentials*. Theoretical Chemistry Accounts: Theory, Computation, and Modeling (Theoretica Chimica Acta), 1997. 97(1): p. 119-124.
100. Schafer, A., H. Horn, and R. Ahlrichs, *Fully optimized contracted Gaussian basis sets for atoms Li to Kr*. The Journal of Chemical Physics, 1992. 97(4): p. 2571-2577.
101. Bader, R.F.W., *Atoms in Molecules: a Quantum Theory*. New York: Oxford University Press, 1990
102. Tang, W., E. Sanville, and G. Henkelman, *A grid-based Bader analysis algorithm without lattice bias*. Journal of Physics: Condensed Matter, 2009. 21(8): p. 084204.
103. Sanville, E., et al., *Improved grid-based algorithm for Bader charge allocation*. Journal of Computational Chemistry, 2007. 28(5): p. 899-908.
104. Henkelman, G., A. Arnaldsson, and H. Jónsson, *A fast and robust algorithm for Bader decomposition of charge density*. Computational Materials Science, 2006. 36(3): p. 354-360.
105. Henkelman, G., B.P. Uberuaga, and H. Jonsson, *A climbing image nudged elastic band method for finding saddle points and minimum energy paths*. The Journal of Chemical Physics, 2000. 113(22): p. 9901-9904.
106. Reinhardt, F., et al., *GaAs surface control during metalorganic vapor phase epitaxy by reflectance anisotropy spectroscopy*. Journal of Vacuum Science & Technology B: Microelectronics and Nanometer Structures, 1993. 11: p. 1427-1430.
107. Cheng, C.-W., et al., *Self-cleaning and surface recovery with arsine pretreatment in ex situ atomic-layer-deposition of Al<sub>2</sub>O<sub>3</sub> on GaAs*. Applied Physics Letters, 2009. 95(8): p. 082106-3.
108. Cho, A.Y., *Growth of III-V semiconductors by molecular beam epitaxy and their properties*. Thin Solid Films, 1983. 100(4): p. 291-317.
109. SpringThorpe, A.J., et al., *Measurement of GaAs surface oxide desorption temperatures*. Applied Physics Letters, 1987. 50(2): p. 77-79.

110. Mizutani, T., *Correct substrate temperature monitoring with infrared optical pyrometer for molecular-beam epitaxy of III--V semiconductors*. Journal of Vacuum Science & Technology B: Microelectronics and Nanometer Structures, 1988. 6(6): p. 1671-1677.
111. Phung, Q., et al., *Ruthenocene and cyclopentadienyl pyrrolyl ruthenium as precursors for ruthenium atomic layer deposition: a comparative study of dissociation enthalpies*. Theoretical Chemistry Accounts, 2012. 131(7): p. 1-9.
112. Elliott, S.D. and J.C. Greer, *Simulating the atomic layer deposition of alumina from first principles*. Journal of Materials Chemistry, 2004. 14(21): p. 3246-3250.
113. Bartram, M.E., T.A. Michalske, and J.W. Rogers, *A reexamination of the chemisorption of trimethylaluminum on silica*. The Journal of Physical Chemistry, 1991. 95(11): p. 4453-4463.
114. Lamagna, L., et al., *Mechanisms for Substrate-Enhanced Growth during the Early Stages of Atomic Layer Deposition of Alumina onto Silicon Nitride Surfaces*. Chemistry of Materials, 2012. 24(6): p. 1080-1090.
115. Libsch, F.R. and M.H. White, *Charge transport and storage of low programming voltage SONOS/MONOS memory devices*. Solid-State Electronics, 1990. 33(1): p. 105-126.
116. Lu, C.-Y., K.-Y. Hsieh, and R. Liu, *Future challenges of flash memory technologies*. Microelectronic Engineering, 2009. 86(3): p. 283-286.
117. Lee, C.-H., K.-C. Park, and K. Kim, *Charge-trapping memory cell of SiO<sub>2</sub>/SiN/high-k dielectric Al<sub>2</sub>O<sub>3</sub> with TaN metal gate for suppressing backward-tunneling effect*. Applied Physics Letters, 2005. 87(7): p. 073510-3.
118. *Laboratorio MDM - IMM - CNR, Milan, Italy*.  
<http://www.mdm.imm.cnr.it/home.html>.
119. Schamm, S., et al., *Chemical/Structural Nanocharacterization and Electrical Properties of ALD-Grown La<sub>2</sub>O<sub>3</sub>/Si Interfaces for Advanced Gate Stacks*. Journal of The Electrochemical Society, 2009. 156(1): p. H1-H6.
120. Lamagna, L., et al., *O<sub>3</sub>-based atomic layer deposition of hexagonal La<sub>2</sub>O<sub>3</sub> films on Si(100) and Ge(100) substrates*. Journal of Applied Physics, 2010. 108(8): p. 084108-11.
121. Elliott, S.D., et al., *Ozone-Based Atomic Layer Deposition of Alumina from TMA: Growth, Morphology, and Reaction Mechanism*. Chemistry of Materials, 2006. 18(16): p. 3764-3773.

122. Blöchl, P.E., *Projector augmented-wave method*. Physical Review B, 1994. 50(24): p. 17953-17979.
123. Kresse, G. and J. Furthmüller, *Efficiency of ab-initio total energy calculations for metals and semiconductors using a plane-wave basis set*. Computational Materials Science, 1996. 6(1): p. 15-50.
124. Deer, W.A., R.A. Howie, and J. Zussman, *An Introduction to the Rock-forming Minerals* 1992.
125. Grillo, M.-E., S.D. Elliott, and C. Freysoldt, *Native defects in hexagonal  $\beta$ -Si<sub>3</sub>N<sub>4</sub> studied using density functional theory calculations*. Physical Review B, 2011. 83(8): p. 085208.
126. Yates, D.J.C., et al., *Infrared studies of the reactions between silica and trimethylaluminum*. The Journal of Physical Chemistry, 1969. 73(4): p. 911-921.
127. Anwender, R., et al., *Formation of Lewis Acidic Support Materials via Chemisorption of Trimethylaluminum on Mesoporous Silicate MCM-41*. Organometallics, 1998. 17(10): p. 2027-2036.
128. Puurunen, R.L., et al., *IR and NMR Study of the Chemisorption of Ammonia on Trimethylaluminum-Modified Silica*. The Journal of Physical Chemistry B, 2000. 104(28): p. 6599-6609.
129. Low, M.J.D., A.G. Severdia, and J. Chan, *Reactive silica : XV. Some properties of solids prepared by the reaction of trimethylaluminum with silica*. Journal of Catalysis, 1981. 69(2): p. 384-391.
130. Levy, R.A., M.L. Green, and P.K. Gallagher, *Characterization of LPCVD Aluminum for VLSI Processing*. Journal of The Electrochemical Society, 1984. 131(9): p. 2175-2182.
131. Klejna, S. and S.D. Elliott, *First-Principles Modeling of the "Clean-Up" of Native Oxides during Atomic Layer Deposition onto III-V Substrates*. The Journal of Physical Chemistry C, 2012. 116(1): p. 643-654.
132. Murray, C. and S.D. Elliott, *Density Functional Theory Predictions of the Composition of Atomic Layer Deposition-Grown Ternary Oxides*. ACS Applied Materials & Interfaces, 2013. 5(9): p. 3704-3715.
133. Elliott, S.D., *Improving ALD growth rate via ligand basicity: Quantum chemical calculations on lanthanum precursors*. Surface and Coatings Technology, 2007. 201(22-23): p. 9076-9081.

134. Marx, D., et al., *Low temperature etching of GaAs substrates and improved morphology of GaAs grown by metalorganic molecular beam epitaxy using trisdimethylaminoarsenic and triethylgallium*. Journal of Crystal Growth, 1995. 150, Part 1(0): p. 551-556.
135. Salim, S., et al., *Surface reactions of dimethylaminoarsine during MOMBE of GaAs*. Journal of Crystal Growth, 1992. 124(1-4): p. 16-22.
136. Shi, B. and C. Tu, *A kinetic model for tris(dimethylamino) arsine decomposition on GaAs(100) surfaces*. Journal of Electronic Materials, 1999. 28(1): p. 43-49.
137. Puurunen, R.L., *Formation of Metal Oxide Particles in Atomic Layer Deposition During the Chemisorption of Metal Chlorides: A Review*. Chemical Vapor Deposition, 2005. 11(2): p. 79-90.
138. Li, K., et al., *Tetrakis(dimethylamido)hafnium Adsorption and Reaction on Hydrogen Terminated Si(100) Surfaces*. The Journal of Physical Chemistry C, 2010. 114(33): p. 14061-14075.
139. Rodríguez-Reyes, J.C., *Mechanisms of adsorption and decomposition of metal alkylamide precursors for ultrathin film growth*. J. Appl. Phys., 2008. 104(8): p. 084907.
140. Rodríguez-Reyes, J.C.F. and A.V. Teplyakov, *Chemisorption of Tetrakis(dimethylamido)titanium on Si(100)-2 × 1: C-H and C-N Bond Reactivity Leading to Low-Temperature Decomposition Pathways*. The Journal of Physical Chemistry C, 2008. 112(26): p. 9695-9705.
141. Bradley, D.C. and M.H. Chisholm, *Transition-metal dialkylamides and disilylamides*. Accounts of Chemical Research, 1976. 9(7): p. 273-280.
142. Salim, S., C.K. Lim, and K.F. Jensen, *Gas-Phase Decomposition Reactions of Tris(dimethylamino)phosphine, -Arsine, and -Stibine Reagents*. Chemistry of Materials, 1995. 7(3): p. 507-516.
143. Kim, T. and F. Zaera, *Surface Chemistry of Pentakis(dimethylamido)tantalum on Ta Surfaces*. The Journal of Physical Chemistry C, 2011. 115(16): p. 8240-8247.
144. Andersen, R.A., D.B. Beach, and W.L. Jolly,  *$\pi$ -Donor character of the dimethylamido ligand*. Inorganic Chemistry, 1985. 24(26): p. 4741-4743.
145. Olivier, S., et al., *Insights into Crystalline Preorganization of Gas-Phase Precursors: Densification Mechanisms*. Chemistry of Materials, 2008. 20(4): p. 1555-1560.

146. Bouman, M. and F. Zaera, *Reductive Eliminations from Amido Metal Complexes: Implications for Metal Film Deposition*. Journal of The Electrochemical Society, 2011. 158(8): p. D524-D526.
147. Burton, B.B., D.N. Goldstein, and S.M. George, *Atomic Layer Deposition of MgO Using Bis(ethylcyclopentadienyl)magnesium and H<sub>2</sub>O*. The Journal of Physical Chemistry C, 2009. 113(5): p. 1939-1946.
148. Amar, J.G., *The Monte Carlo method in science and engineering*. Computing in Science & Engineering, 2006. 8(2): p. 9-19.

## Table of Abbreviations

ALD	- Atomic Layer Deposition
ano-rcc	- atomic natural orbital relativistic correlation consistent basis sets
aug-cc	- augmented correlation consistent basis sets
B3LYP	- Becke, 3-parameter, Lee-Yang-Parr functional
BSSE	- Basis Set Superposition Error
CAS	- Complete Active Space
CASPT2	- Complete Active Space Perturbation Theory of 2nd order
CASSCF	- Complete Active Space Self-Consistent Field
CC	- Coupled Cluster
CCSD	- Coupled Cluster Single and Double excitation
CCSD(T)	- Coupled Cluster Single, Double and Triple excitations
CMOS	- Complementary Metal Oxide Semiconductor
CVD	- Chemical Vapour Deposition
DFT	- Density Functional Theory
$D_{it}$	- Density of interface traps
dma	- Dimethylamido ligand, $[N(CH_3)_2]^-$
DRAM	- Dynamic Random Access Memory
Et	- Ethyl group, $C_2H_5$
FET	- Field Effect Transistor
FTIR	- Fourier Transform Infrared spectroscopy
GGA	- Generalized Gradient Approximation
GPC	- Growth Per Cycle
HF	- Hartree Fock approximation
IL	- Interfacial Layer
$L$	- Ligand
LDA	- Local Density Approximation
$M$	- Metal
Me	- Methyl group, $CH_3$
MGR	- Molar Growth Rate
MMI	- N-methyl methyleneimine, $CH_3NCH_2$
MOS	- Metal Oxide Semiconductor
MP2	- 2nd order Møller-Plesset perturbation theory

*Table of Abbreviations*

NEB	- Nudged Elastic Band method
PAW	- Projector-Augmented Wave method
PBE	- Perdew-Burke-Ernzerhof functional
PDMAT	- pentakis(dimethylamido)tantalum, Ta[N(CH <sub>3</sub> ) <sub>2</sub> ] <sub>5</sub>
pVTZ	- Polarized Valance Triple-Zeta basis functions
PW91	- Perdew and Wang 1991 functional
QCISD	- Quadratic Configuration Interaction with Single and Double substitutions
QMS	- Quadruple Mass Spectrometry
RI	- Resolution of the Identity approximation
SE	- Spectroscopic Ellipsometry
SONOS	- Silicon-Oxide-Nitride-Oxide-Silicon device
SRPS	- Synchrotron Radiation Photoelectron Spectroscopy
STEM	- Scanning Transmission Electron Microscopy
TDMAAs	- tris(dimethylamino)arsine, As[N(CH <sub>3</sub> ) <sub>2</sub> ] <sub>3</sub>
TDMAH	- tetrakis(dimethylamido)hafnium, Hf[N(CH <sub>3</sub> ) <sub>2</sub> ] <sub>4</sub>
TDMAT	- tetrakis(dimethylamido)titanium, Ti[N(CH <sub>3</sub> ) <sub>2</sub> ] <sub>4</sub>
TEMAH	- tetrakis(ethylmethylamido)hafnium, Hf[N(C <sub>2</sub> H <sub>5</sub> )(CH <sub>3</sub> )] <sub>4</sub>
TEMAZ	- tetrakis(ethylmethylamido)zirconium, Zr[N(C <sub>2</sub> H <sub>5</sub> )(CH <sub>3</sub> )] <sub>4</sub>
TGR	- Thickness Growth Rate
TMA	- trimethylaluminum, Al(CH <sub>3</sub> ) <sub>3</sub>
ToF SIMS	- Time of Flight Secondary Ion Mass Spectroscopy
TPD	- Temperature Programmed Desorption
TS	- Transition State
TST	- Transition State Tool
TZVPP	- Triple-Zeta Valance Plus Polarization basis functions
USPP	- Ultrasoft Pseudopotentials
VTZP	- Valance Triple-Zeta Polarization basis functions
XPS	- X-ray Photoelectron Spectroscopy
XRR	- X-ray Reflectivity
ZPE	- Zero Point Energy